Master of Science Thesis

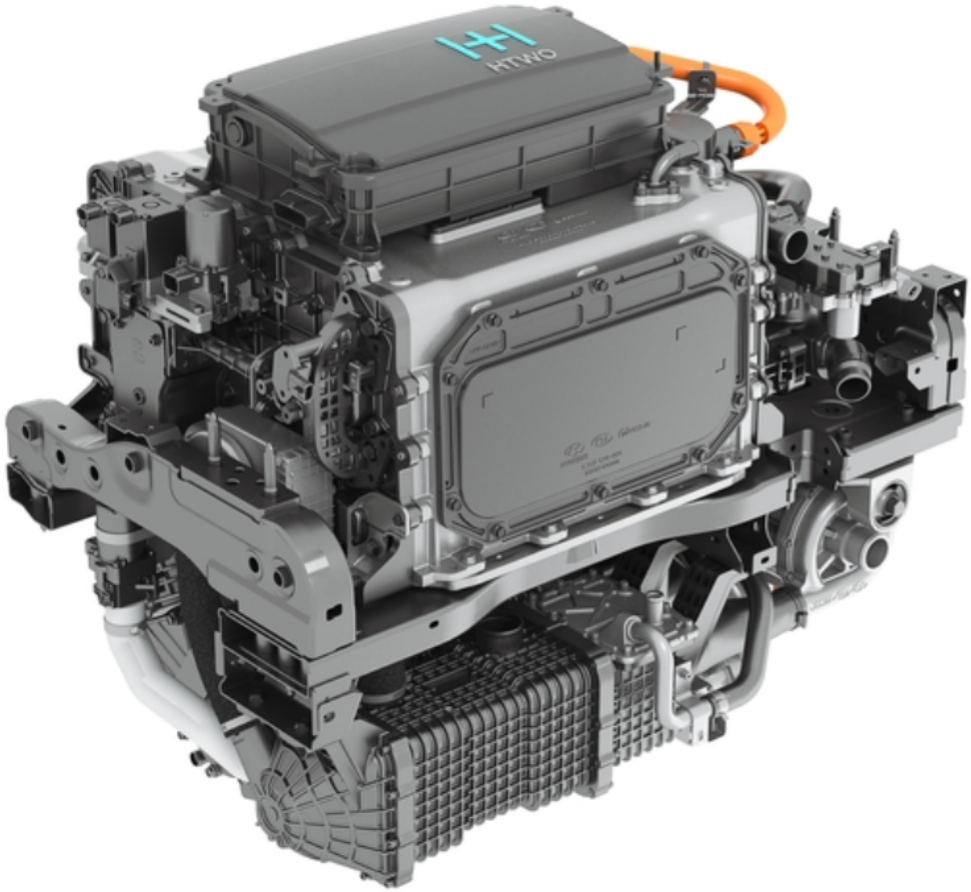

Turbocharging an Automotive Hydrogen PEM Fuel Cell Air Processing System

Simulations on Boost Power and Fuel Saving

Elliott Desmit

April 14, 2024

Aerodynamics

TU Delft

Faculty of Aerospace Engineering

Delft University of Technology

Turbocharging an Automotive Hydrogen PEM Fuel Cell Air Processing System

Simulations on Boost Power and Fuel Saving

Master of Science Thesis

For obtaining the degree of Master of Science in Aerospace Engineering
at Delft University of Technology

Elliott Desmit

April 14, 2024

Cover Image Credits: Hyundai Motor Group

Faculty of Aerospace Engineering · Delft University of Technology

Delft University of Technology

DELFT UNIVERSITY OF TECHNOLOGY
DEPARTMENT OF AERODYNAMICS

The undersigned hereby certify that they have read and recommend to the Faculty of Aerospace Engineering for acceptance the thesis entitled **"Turbocharging an Automotive Hydrogen PEM Fuel Cell Air Processing System"** by **Elliott Desmit** in fulfillment of the requirements for the degree of **Master of Science**.

Dated: April 14, 2024

Supervisors:

Dr.ir. Carlo De Servi - TU Delft

Dr.ir. Lindert van Biert - TU Delft

Dr.-Ing. Sebastian Martin - HMETC

Preface

This report is a result of my thesis project at Hyundai Motor Europe Technical Center (HMETC) in Rüsselsheim, Germany, which marks my graduation as an aerospace engineer at the TU Delft. The thesis took place from June 2023 until April 2024, being the logical step after a successful internship at HMETC. I got the opportunity to perform this thesis and internship because I was already familiar with HMETC beforehand, thanks to my work at Forze Hydrogen Racing. There, I had a very fruitful technical collaboration with HMETC, focused on the fuel cell system of the Forze IX race car. After my time at Forze Hydrogen Racing ended, I reached out to my contacts at HMETC, and the rest is history.

This document is both meant to show the defense committee the work performed during this thesis, and as documentation of the project for HMETC. The aim while writing this thesis was the reproducibility of the work, which I think is important when doing research.

I would like to take the opportunity to show my gratitude to my HMETC supervisors, Dr. Sebastian Martin and Steffen Zinner. I very much appreciate the level of involvement they have shown in my project, both organizational and technical. I would also like to thank Harun Zlojo, for the thorough support he gave me on working with AVL Cruise M. Next, I would like to thank my TU Delft supervisors, Dr. Carlo De Servi and Dr. Lindert van Biert, whose time, support, and flexibility allowed me to pursue this thesis in industry, for which I am grateful.

Last but not least, I would like to thank all my friends and family. To my friends, who have always supported me, whether they are in Belgium, the Netherlands, Germany, the UK, Spain, or anywhere else. To my girlfriend, Blanca, for always being there for me in both the good and hard times, every single day. Finally, to my family and parents, for giving me unconditional love and support with everything I do in life. I could not have wished for a better mom and dad. Without them, I would have never been where I am right now.

Thanks to all the people above, my master's thesis was a success.

Elliott Desmit
Mainz, April 2024

Abstract

Hydrogen Polymer Electrolyte Membrane (PEM) fuel cell technology is becoming increasingly popular in the transportation sector, especially the automotive industry. It can power electric drives by converting hydrogen into electricity in a chemical reaction with oxygen, whose products consist only of water. Therefore, hydrogen PEM fuel cell-based powertrains are free of any harmful emissions, enabling clean propulsion technology. An important part of an automotive fuel cell system is the air processing subsystem, which usually features an electrical air compressor (E-compressor) to supply the necessary oxygen for the chemical reaction. This E-compressor can absorb between 10-30% of the fuel cell gross power. One way to decrease this share is to expand the fuel cell air exhaust flow in a turbine that contributes to power the E-compressor, essentially realizing an electric turbocharger (E-turbocharger). E-turbochargers for fuel cells are still in the development phase, therefore there is a lack of experience and knowledge on their benefit.

In this thesis, a model of an existing automotive PEM fuel cell air processing system has been developed using the AVL Cruise M software. In addition, two prototype PEM fuel cell E-turbochargers (ETC1 and ETC2, respectively) have been modeled and integrated into the main air processing system model. Steady-state simulations have been performed for three different power levels. Moreover, the turbine inlet temperature of the ETC1-based model was varied in the range of 60°C to 150°C to quantify what benefits exhaust heating with waste heat brings in addition to the inherent turbocharging performance gains.

The results show that compared to the baseline system, the model featuring ETC1 achieved an increase in net power between 3.04-6.78% or a decrease in fuel consumption between 3.19-7.67%, depending on the power level. For the ETC2-based model, from low to high load, the net power increased between 1.88-2.04%, or fuel consumption decreased between 2.07-3.17% compared to the baseline system. When increasing the turbine inlet temperature to 150°C, the model showed an additional decrease in fuel consumption of 2.1 percentage points at full power. The models could be improved by implementing a first-principle-based model of the E-compressor and E-turbocharger, which could have been developed in this project if more detailed information on the heat flows within these components was available.

Table of Contents

List of Figures

List of Tables

Nomenclature

Physical Constants

F	Faraday's Constant
R	Universal Gas Constant

Symbols

α	Efficiency Correction Coefficient
β	Efficiency Correction Coefficient
ΔG	Change of Gibbs Free Energy
ΔH	Heat of Formation (of a Chemical Reaction)
ΔS	Entropy Change
δ	Efficiency Correction Coefficient
$\dot{m}$	Air Massflow
$\dot{Q}$	Heat Flow
ϵ	Heat Transfer Effectiveness
η	Efficiency
γ	Ratio of Specific Heat Capacities of Air
κ	Water Flow Factor
λ	Stoichiometry
ω	Humidity Ratio
Π	Pressure Ratio
ψ	Water vs Air Pressure Ratio
Θ	Temperature Ratio
A	Activation Loss Constant/Heat Transfer Area
a	Polarization Curve Constant/chemical activity
b	Polarization Curve Constant
C	Heat Capacity Rate
c	Polarization Curve Constant
C_1	Exchange Current Density Constant
C_2	Exchange Current Density Constant
C_3	Exchange Current Density Constant
C_4	Exchange Current Density Constant
c_p	Specific Heat Capacity at Constant Pressure
d	Polarization Curve Constant
E	Theoretical Maximum Fuel Cell Voltage
f	Polarization Curve Constant
I	Electrical Current
i	Current Density
i_0	Exchange Current Density
i_n	Internal Current Density
M	Molar Mass
n	Rotational Speed
n_{cell}	Number of Fuel Cells in Series
P	Power (Electric/Mechanical)
p	Pressure
r	Stack Electrical Resistance
s	Specific Entropy
T	Temperature
U	Overall Heat Transfer Coefficient
V	Electrical Potential

Subscripts

0	Standard Temperature and Pressure (25°C & 1atm)
1	compressor inlet
2	compressor outlet
$2L$	second law of thermodynamics
3	turbine inlet
4	turbine outlet

a	air
ab	adiabatic process
abs	absorber (heat pump)
act	activation losses
amb	ambient conditions
C	heat pump cold side (evaporator)
c	consumption/coolant/compressor side
$Carnot$	Carnot process
$conc$	concentration losses
$cond$	condenser side (heat pump)
d	dry
$emot$	E-motor (of the E-compressor)
$evap$	evaporator side (heat pump)
fc	fuel cell stack
gen	generator (heat pump)
H	heat pump hot side (condenser)
H_2	hydrogen
H_2O	water
HP	heat pump compressor
i	inlet
int	internal current losses
inv	air compressor inverter
l	loss
lp	liquid pump (heat pump)
max	maximum value
min	minimum value
net	net (not gross)
o	outlet
O_2	oxygen
$ohmic$	ohmic losses
p	production
$poly$	polytropic (heat pump compressor)
s	source fluid evaporator (heat pump)/isentropic process
sat	saturated (vapor)
sys	system
t	turbine side
tot	total(=stagnation) conditions
tr	transfer
w	wet
wv	water vapor

Abbreviations

1D	One-Dimenional
CO	Carbon Monoxide
COP	Coefficient of Performance
ETC	Electric Turbocharger
FTG	Fixed Turbine Geometry
GDL	Gas Diffusion Layer
HHV	Higher Heating Value (Hydrogen)
HVAC	Heat, Ventilation and Air Conditioning
ICE	Internal Combustion Engine
IPCC	Intergovernmental Panel on Climate Change
LHV	Lower Heating Value (Hydrogen)
LMTD	Log-Mean Temperature Difference
MEA	Membrane-Electrode Assembly
NTU	Number of Transfer Units
OCV	Open Circuit Voltage
ORC	Organic Rankine Cycle
PBI	Polybenzimidazole
PEM	Proton (Polymer) Exchange (Electrolyte) Membrane
PID	Proportional Integral Derivative
RH	Relative Humidity
RQ	Research Question
SRC	Steam Rankine Cycle
TEG	Thermo-Electric Generator
TIT	Turbine Inlet Temperature
VAC	Vapor Ad/Absorption Cycle
VCC	Vapor Compression Cycle
VTG	Variable Turbine Geometry
WHR	Waste Heat Recovery

Chapter 1

Introduction

1.1 Motivation and Background Information for this Thesis

The latest IPCC report states that the current global warming status and trend shows that it is becoming increasingly difficult to limit the global temperature increase to below 2°C, which is already higher than the initial target of 1.5°C [1, p. 10]. Stronger efforts on many sides of society are necessary to stay on course. Large greenhouse gas emitters are sectors such as energy, industry, and transportation [1, p. 22]. Hydrogen features clear benefits to help make these sectors climate neutral, due to its high gravimetric energy density as well as being able to be sustainably (i.e. circularly) used and produced [1, p. 29].

Next to combusting hydrogen, which does not directly produce CO_2 emissions and therefore provides a cleaner alternative to fossil fuels for combustion engines [2, p. 17], it is also possible to use it to generate electrical energy, free of any harmful emissions. This process is the reverse process for making clean hydrogen, and is called reverse electrolysis of water: hydrogen and oxygen are made to chemically react, creating water [3, p. 2]. In the process, next to heat, energy is released in the form of electrical current which can power any type of electric machine. The specific type of energy converter performing this process is called a hydrogen fuel cell.

Fuel cell technology, first conceived in 1839 [3, p. 1][4, p. 4], is now becoming more and more relevant in crucial sectors such as energy and transportation in the fight against climate change due to the aforementioned benefits it features. A myriad of technological challenges and research opportunities therefore arise. This thesis aims to tackle one of them, specifically concerning hydrogen polymer electrolyte membrane (PEM) fuel cells. These are considered to be amongst the best options for automotive applications due to their high power density, which reduces weight and size, and low operating temperatures, which facilitate short startup and shutdown times as well as good cold-weather performance [4, p. 13].

A desired technical development is to make PEM fuel cell systems more energy-efficient and power-dense. One relatively low-effort way to do that is by implementing waste heat recovery (WHR). Among others, one way to implement such a solution is to expand the fuel cell air exhaust flow in a turbine, which in turn powers a compressor at the air intake. This is commonly called forced induction or turbocharging, and has been used extensively in mass-produced internal combustion engines (ICE) [5].

Unlike ICEs, no piston movement helps pull air into the fuel cell, so an air compressor is a standard component of a fuel cell system. It needs to be driven by an electrical motor that gets its power from the fuel cell itself through an inverter (converting from DC to AC). The electric motor can absorb between 10-30% [6] of the fuel cell gross power. Adding a turbine to this electrical compressor, essentially creating an electric turbo-compressor or E-turbocharger (ETC), will reduce the electrical power consumption needed for the air compression. This means the system can either provide more net power for the same fuel consumption, or the same net power using less fuel.

Since the fuel cell exhaust air features a significant water concentration, water vapor may condense within the turbine. This can lead to various problems, with the main ones being water droplet erosion of the turbine blades and the damaging of the electronics [7]. To prevent these types of damages, a water separator should be installed before the turbine inlet. This is therefore a necessary component when turbocharging a PEM fuel cell system.

Although turbochargers are mass-produced for millions of ICE vehicle applications, E-turbochargers for fuel cells are still in the development phase. Currently, this technology is mostly being integrated and tested in demonstrator vehicles by a number of OEMs, but there is no mass production ongoing. Therefore, there is a lack of experience and knowledge on the potential performance increase that comes with these E-turbochargers. This leaves a research gap to be filled, and represents the main motivation behind this specific research.

1.2 Research Objective and Questions

The aim of this research is to investigate waste heat recovery solutions for low-temperature PEM fuel cells for automotive applications such as turbocharging as a means of increasing the performance of the powertrain, by developing models of novel fuel cell air processing system concepts and carrying out simulations to quantify their potential performance gains against a benchmark.

The specific research questions (RQs) that were desired to be answered upon completion of this work are posed here:

1. RQ1: What are potential methods of increasing the efficiency of a hydrogen PEM fuel cell system by means of waste heat recovery?
    (a) What are the advantages and disadvantages of each selected method when applied

to a commercial road vehicle?

2. RQ2: By how much does the efficiency of an automotive hydrogen PEM fuel cell system increase when its electrical air compressor is replaced by an electrical turbocharger that harvests power from the fuel cell exhaust stream?
   (a) At the same net output power, how much hydrogen can be saved?
   (b) At the same hydrogen consumption, how much more net power can be produced?
   (c) Does the use of a smaller turbine geometry yield higher system efficiencies at lower power outputs compared to a bigger turbine?
3. RQ3: By how much does the efficiency of the turbocharged fuel cell system increase when a specific amount of waste heat from another source is added to the exhaust stream, thus increasing turbine inlet temperatures?
4. RQ4: In which circumstances could the addition of a pressure regulation valve be beneficial for the working of the aforementioned turbocharged fuel cell system?
   (a) What is the best location for this pressure regulation valve?

1.3 Report Outline

In Chapter 2, the relevant literature is laid out to form the correct basis of the research. More information on hydrogen PEM fuel cell systems is provided, to define the state of the art of this technology. Conventional automotive WHR techniques as well as specific solutions for hydrogen fuel cell systems are discussed, which helped answering RQ1.

Subsequently, Chapter 3 describes in detail the methodology followed for developing the models and performing the simulations of a turbocharged PEM fuel cell air processing system with the goal to answer RQs 2, 3 and 4.

The results coming from all the simulations are presented and elaborated upon in Chapter 4, while conclusions and recommendations for further work are discussed in Chapter 5.

There are also two appendices to this thesis. Appendix A contains additional diagrams and graphs for extra insight into certain topics, while Appendix B covers extra calculations that for the sake of brevity were not reported in the Results sections.

Chapter 2

Literature Review

In this chapter, the relevant literature regarding the research is presented. First, the basics of a hydrogen PEM fuel cell system are laid out, including the polarization curve. Next, technical aspects regarding optimal operation of a fuel cell system are discussed. Lastly, potential waste heat recovery solutions for automotive hydrogen PEM fuel cell systems are elaborated upon.

2.1 Principles of Hydrogen PEM Fuel Cell Systems

A hydrogen PEM fuel cell system comprises of three main parts: the fuel cell stack, the air processing system and the hydrogen supply system. Each of these three parts will be briefly explained in the following subsections.

2.1.1 The Hydrogen PEM Fuel Cell

A hydrogen PEM fuel cell is a type of fuel cell that generates electricity by letting the electrons from the hydrogen flow through an external circuit by means of reverse electrolysis [3, p. 2]. It consists of a combination of layers that collectively make up the membrane-electrode assembly (MEA) [3, p. 73]. The operating principle of such a fuel cell is visualized in Figure 2.1.

The blue layer in the middle is the Proton Exchange Membrane (PEM), also called the polymer electrolyte membrane as it functions as the electrolyte in the cell. The black thin layers on either side of the PEM are the electrodes of the cell. They contain a catalyst (usually platinum) that helps the chemical reactions to take place. The thicker grey layers are the Gas Diffusion Layers (GDL), that help the hydrogen and air spread evenly on the surface of the electrodes [3, p. 73].

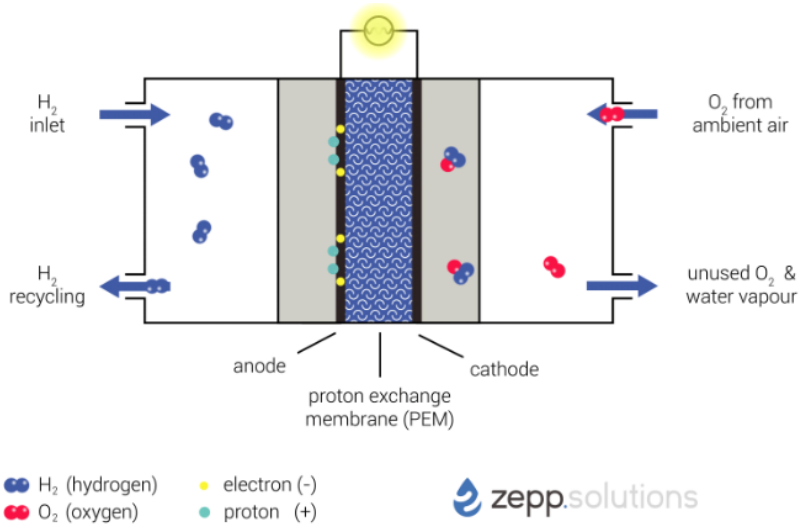

Figure 2.1: Schematic of a Hydrogen PEM Fuel Cell[1]

As can be seen in the schematic, the hydrogen molecules (H_2) come in at the anode (the negative side of the cell) and split into their two electrons and protons (thanks to the catalyst). The protons can go through the exchange membrane, but the electrons cannot pass through it so they flow along an external circuit that can then power an electrical load (in this case a simple light bulb). Once the protons and electrons reach the cathode (the positive side of the cell), they are combined with the incoming oxygen molecules (O_2) to form water (H_2O). The chemical reactions that take place at the anode and cathode side respectively, namely hydrogen oxidation and oxygen reduction, are very simple [4, p. 17]:

$$2H_2 \rightarrow 4H^+ + 4e^- \tag{2.1}$$

$$O_2 + 4H^+ + 4e^- \rightarrow 2H_2O \tag{2.2}$$

The overall chemical reaction for the whole fuel cell is then:

$$2H_2 + O_2 \rightarrow 2H_2O \tag{2.3}$$

In practice, the generated voltage of a single fuel cell is low, usually below 1 V. To generate useful voltages for applications such as power units for vehicles, many (as in, hundreds of) identical fuel cells are connected in series, to form a so-called fuel cell stack. In order to compactly connect many fuel cells in series, the concept of the bipolar plate is often used. The bipolar plate electrically connects the cathode from one cell to the anode of the next, to increase the voltage [4, p. 73]. Since it physically separates two cells, it usually also features coolant channels to facilitate heat rejection. A schematic of the MEA with bipolar plates on both sides is shown below:

[1] https://zepp.solutions/en/technology/

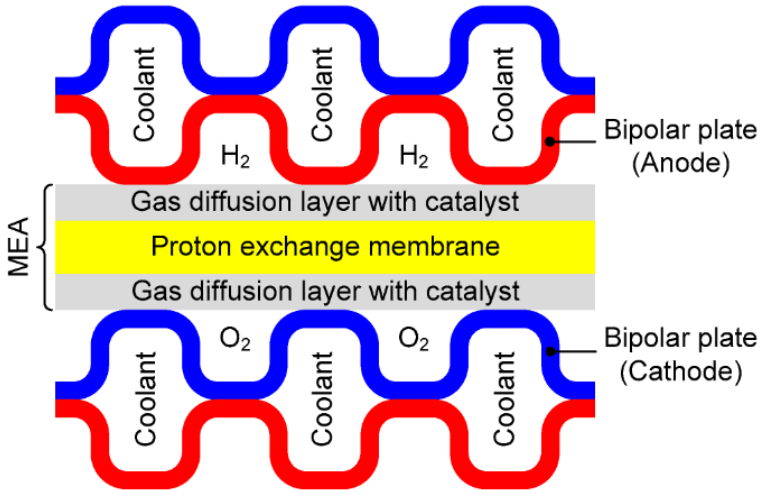

Figure 2.2: Schematic of a Membrane Electrode Assembly and Bipolar Plates [8]

2.1.2 The Air Processing System

The air processing system aim is to supply the right amount of oxygen at the right operating conditions for the stack. As will be discussed later, for optimal performance of the stack, the air should enter the stack at the right temperature, pressure and humidity levels. A simple layout of a typical PEM fuel cell air processing system is shown below:

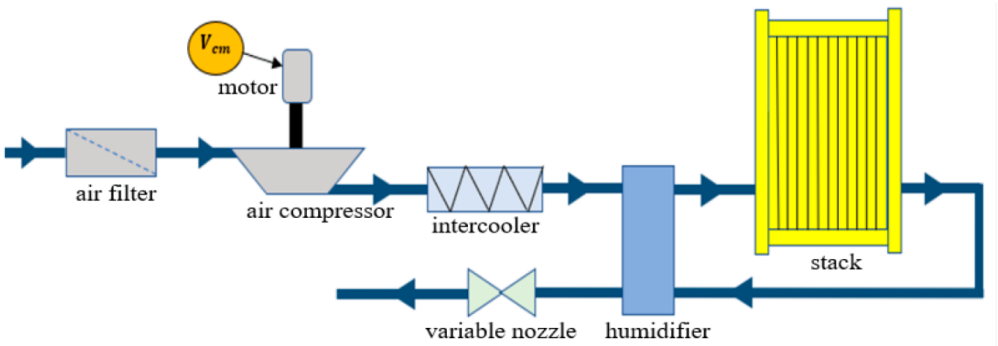

Figure 2.3: Schematic of a Typical Fuel Cell Air Processing System [9]

The first component that the intake air sees is an air filter, just like in ICE air systems. This filters out incoming rainwater, particles and chemicals. Rainwater is bad for the compressor which is the next component in the system. However, small dirt particles could block the oxygen and hydrogen supply channels in the cells, and the platinum catalyst in the MEAs could be damaged by contaminants such as carbon monoxide (CO) [4, p. 275].

Unlike ICEs where the moving pistons pull air into the engine, a fuel cell stack has no moving parts and needs an external component to bring the reactant gasses into the cells. On the

oxygen side, an electrically driven air compressor is needed in order to blow oxygen into the stack. This is one of the main components of the air processing system, and it consumes from 10% to up to 30% of gross stack output power, depending on the size and pressure level of the fuel cell system [3, p. 103][10, p. 4][6].

To control the supply temperature of the air, a heat exchanger or intercooler is integrated into the system. Most of commercially-available PEM fuel cells operate below 100°C, due to the thermal degradation of the polymer electrolyte membrane above this temperature level [4, p. 91], and since the temperature at the outlet of the air compressor can be more than that, the air delivered by the compressor needs to be cooled. However, high temperature PEM fuel cells which could operate between 160°C and 200°C, using acid-doped polybenzimidazoles (PBIs) are currently researched. A higher operating temperature would have several advantages for the fuel cell system: all water is evaporated making water management easier, the catalyst is more resistant to CO poisoning and the thermal management system can be downsized due to the higher temperature difference with the ambient [4, p. 91][11].

Next to material limits, humidity is also very important for the PEM to operate properly, and depending on the operating temperature of the fuel cells, the water produced on the cathode side through the chemical reaction is not sufficient to maintain a good degree of humidity [3, p. 84], especially at the inlet of the bipolar plate. A humidifier can be included in the air supply system to humidify the incoming air recuperating water from the stack exhaust air.

Finally, in order to control the pressure level inside the fuel cell stack independently of the air massflow provided by the compressor, a backpressure valve (the variable nozzle in Figure 2.3) is used. The more this valve is closed, the higher the stack pressure, which also leads to a higher compressor power consumption.

2.1.3 The Hydrogen Supply System

In the automotive industry, which is the application considered in this thesis, hydrogen is stored as a gas at pressure levels of usually 350 or 700bar [4, p. 311]. A possible layout of the hydrogen supply system is shown in Figure 2.4[2].

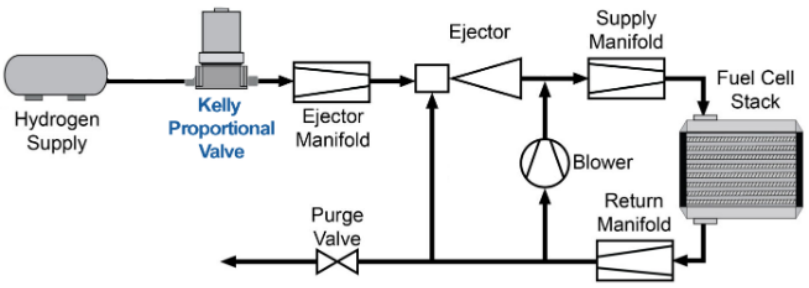

Figure 2.4: Schematic of a Gaseous Storage Fuel Cell Hydrogen Supply System

[2] https://kellypneumatics.com/fuel-cells-and-mass-flow-controllers

Given the high pressure of the hydrogen in the tank, no pumping mechanism is needed to supply the fuel into the stack.

A proportional valve is used to maintain the right hydrogen massflow. This is usually twice the hydrogen needed for the chemical reaction [4, p.128], in order to avoid fuel starvation in the last cells of the stack due to pressure losses along the channels. This leads to an excess of hydrogen at the stack outlet, and recirculation is needed to prevent wasting it.

Hydrogen recirculation can be achieved either by using an electrically powered hydrogen gas blower, or by using an ejector that creates a venturi effect causing the exhausted hydrogen to be sucked back into the stack. The solution with the ejector has the benefits of lower power consumption as well as a reduction of system weight and volume. These two options can also be combined, as seen in Figure 2.4.

Lastly, a purge valve is needed since water and nitrogen cross over from the cathode side to the anode side, affecting the recirculation performance. Every once in a while, the recirculation loop has to be 'purged' to eliminate the accumulated water and nitrogen [4, p.128]. However, this purging inevitably wastes some hydrogen as well.

2.1.4 Efficiency of Hydrogen Fuel Cells

The theoretical maximum voltage that can be achieved in a hydrogen fuel cell can be calculated as follows [3, p. 30]:

$$E = \frac{-\Delta G}{2F} \tag{2.4}$$

where ΔG is the Gibbs free energy associated with the reaction, which can be specifically defined as follows:

$$\Delta G = \Delta H - T\Delta S \tag{2.5}$$

where ΔH is the difference in the enthalpy of formation between the products and the reactants, T is the fuel cell temperature and ΔS is the entropy generation during the reaction. Clearly, at higher temperatures, for the same entropy generation, less Gibbs free energy is available. According to Equation 2.5, the maximum value for ΔG that could be obtained is ΔH, provided $\Delta S = 0$. The value of ΔH depends on the choice of using the higher heating value (HHV) or lower heating value (LHV) of hydrogen.

Strictly speaking, the former represents a situation where hydrogen combusts stoichiometrically and only liquid water is produced (latent heat of vaporization is released when the water condenses), while the latter refers to the case of a large excess of air with the produced water remaining in the vapor state.

At 25°C and atmospheric pressure, the hydrogen HHV equals -285.84kJ/mol and the LHV equals -241.83kJ/mol [3, p. 32]. Their difference is exactly 44.01kJ/mol which is the latent heat of vaporization of water.

Based on the HHV of hydrogen and using Equation 2.5, the theoretical maximum fuel cell potential at 25°C and atmospheric pressure is 285840/192971 = 1.48V. Table 2.1 shows the variation in efficiency as a function of the temperature [3, p. 33]. The efficiency of an ideal fuel cell is then the theoretical maximum voltage E divided by 1.48V.

Table 2.1: Theoretical Maximum Efficiency of a Hydrogen Fuel Cell at Various Temperatures

Water State [-]	**T [°C]**	$\mathbf{\Delta G = \Delta H - T\Delta S}$ **[kJ/mol]**	$\mathbf{E = \frac{-\Delta G}{2F}}$ **[V]**	$\eta_{\mathbf{HHV}}$ **[%]**
liquid	25	-237.2	1.23	83
liquid	80	-228.2	1.18	80
gaseous	100	-225.2	1.17	79
gaseous	200	-220.4	1.14	77
gaseous	400	-210.3	1.09	74
gaseous	600	-199.6	1.04	70
gaseous	800	-188.6	0.98	66
gaseous	1000	-177.4	0.92	62

2.1.5 The Fuel Cell Polarization Curve

The polarization curve visualizes the voltage that the stack generates as a function of the current that is drawn from it, depending also on various operational parameters. An examplary polarization curve is shown in Figure 2.5.

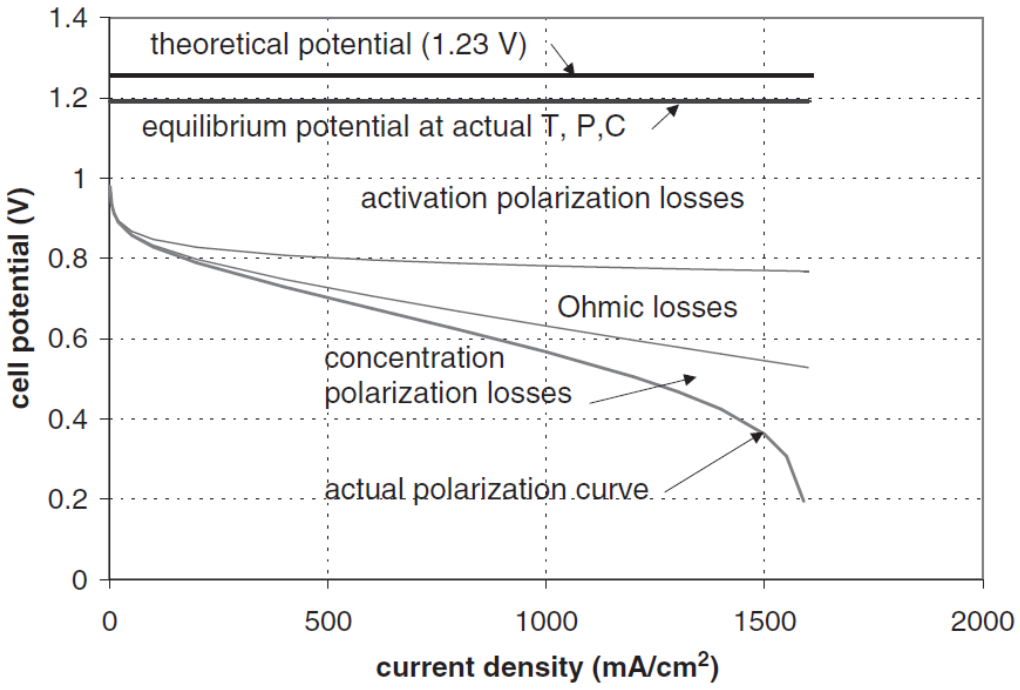

Figure 2.5: Polarization Curve of an Exemplary Low Temperature Fuel Cell [4, p. 50]

As can be seen in Figure 2.5, the cell voltage decreases when an increasing amount of current is drawn from it. The current level in the stack here is expressed in units of mA/cm^2, or current divided by the active cell area (the 2-dimensional area on which the reactions take place), also known as the current density i. When no current is being drawn from the cells, the voltage is maximum and corresponds to the open circuit voltage (OCV) of the fuel cell. The OCV, denoted as E, can be theoretically calculated through the Nernst equation given below [3, p. 36]:

$$E = \frac{\Delta H_0}{2F} - \frac{T\Delta S_0}{2F} + \frac{RT}{2F} \cdot \ln\left(\frac{a_{H_2} \cdot a_{O_2}^{0.5}}{a_{H_2O}}\right) = E_0 + \frac{RT}{2F} \cdot \ln\left(\frac{a_{H_2} \cdot a_{O_2}^{0.5}}{a_{H_2O}}\right) \tag{2.6}$$

where E_0 is the theoretical OCV at standard pressure and temperature, R is the universal gas constant, T is the fuel cell temperature, and F the Faraday constant. Finally, a represents the activity of the reactants or products (either hydrogen, oxygen or water), which for an ideal gas could be shown to be equal to the ratio of the respective partial pressure and the atmospheric pressure [3, p. 35].

With reference to Figure 2.5, there are four main loss mechanism that cause the voltage to decrease for increasing current densities. These losses are called: activation losses, ohmic losses, internal currents/fuel crossover, and finally, concentration losses.

The various losses (except for fuel crossover) are individually visualized in Figure 2.6.

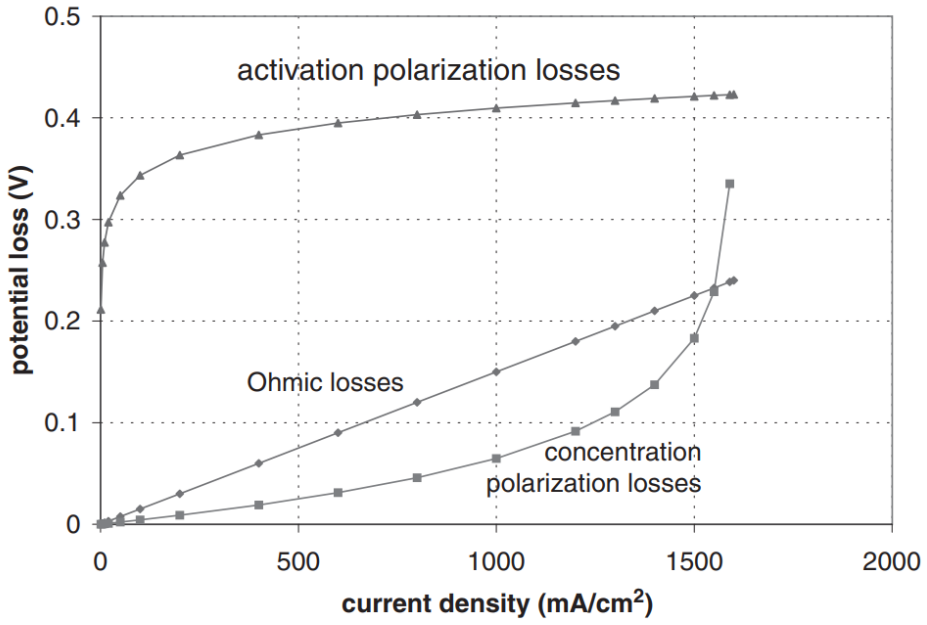

Figure 2.6: The Various Voltage Loss Mechanisms in a PEM Fuel Cell [4, p. 48]

Activation losses result from the need for an activation energy to start off the chemical reactions. This consumes a part of the initial OCV. In hydrogen PEM fuel cells, the cathode (air) activation losses are dominant while those of the anode are negligible [3, p. 52]. These

activation losses scale logarithmically with the current, having their main effect at small current densities and approach a constant value at large current densities, as shown in Figure 2.6. Therefore, they can be expressed as:

$$\Delta V_{act} = A \ln\left(\frac{i}{i_0}\right) \tag{2.7}$$

Where A is a design-dependent variable, and i_0 is the exchange current density, which is a measure of the 'readiness to provide power' of the fuel cell as it represents the amount of electrons flowing back and forth in equilibrium [3, p. 50]. The latter is also the dominant term in the activation losses, and can be increased (which is beneficial) by increasing cell temperature and reactant pressure.

Ohmic losses are voltage drops that arise due to the electrical resistance inside the cells. These occur in both the electrodes and electrolyte, due to resistance put up against the flow of electrons and protons, respectively. These are Ohmic materials, meaning the current going through them is directly and linearly proportional to the voltage difference through their Ohmic resistance. Therefore this voltage drop increases linearly with increasing current [3, p. 57]:

$$\Delta V_{ohmic} = r \cdot i \tag{2.8}$$

where r is the electrical resitance.

Internal currents, meaning electrons that manage to pass through the PEM, and fuel crossover, meaning $H2$ molecules that pass through without reaction with the anode catalyst, can be assumed to have the same effect [3, p. 54]. From the perspective of the electrodes, these moving electrons contribute to the current density, even though they do not pass along the electric circuit. The total current density i is therefore the sum of the internal current density i_n and the useful current density i, and in the activation losses this means [3, p. 55]:

$$\Delta V_{int} = A \ln\left(\frac{i + i_n}{i_0}\right) \tag{2.9}$$

Hence at zero effective current ($i = 0$), especially in low temperature fuel cells where the exchange current density is small, there are already noticable activation losses. This can be seen in Figure 2.5, where the actual OCV (the solid grey line) is just below 1.2 V but the theoretical OCV (the solid black line) is 1.23 V (corresponding to the maximum efficiency of 83% at standard temperature and pressure shown in Table 2.1). At higher temperatures, this initial drop in OCV is much less pronounced due to the steep increase of the dominant parameter i_0.

Finally, concentration losses result from the fact that at very high currents, high amounts of hydrogen and oxygen are consumed each second, leading to reduced concentration of these reactants. This in turn lowers the voltage further. Experiments have shown an empirical relation between this voltage drop and the current that takes the shape of an exponential function, becoming more severe at higher currents [3, p. 59]:

$$\Delta V_{conc} = d \cdot \exp(f \cdot i) \tag{2.10}$$

Combining all these losses, one can express the voltage analytically in terms of the applied current density and other stack parameters as follows:

$$V_{cell}(T, p, i) = E_0 + a \cdot T \cdot \ln(p) - r \cdot i - b \cdot \ln(i) - c \cdot \exp(d \cdot i) \tag{2.11}$$

Where the coefficients a, b, c, d and r are system dependent parameters positive in value. All these losses can be influenced by means of various parameters, such as concentration, electrolyte porosity, reactant pressure, temperature and relative humidity (RH). Since the air side is the focus of this research, the main considered parameters influencing the polarization curve are air pressure, temperature and RH.

2.2 Influence of Operating Conditions on PEM Fuel Cells

It is important to operate the fuel cell stack within certain limits to achieve the best performance, but also to protect it from damaging. The following section gives more background on i) the influence that certain operating parameters have on the performance of the stack, ii) the desired operating conditions as well as iii) the main operating limits of current PEMs.

2.2.1 Effects of Operating Pressure and Temperature

Pressure and temperature affect mainly two aspects of the polarization curve: the OCV and the excange current density. Considering equation 2.11, the open circuit voltage is given by:

$$E = E_0 + a \cdot T \cdot \ln(p) \tag{2.12}$$

Remember that E_0 itself reduces approximately linearly with increasing temperature (Table 2.1). Hence, the temperature seems to have both a good and bad effect. The second term on the right hand side of equation 2.12 shows that at higher temperatures, increasing the pressure gives more benefit than at lower temperatures.

The exchange current density has the following dependency on pressure and temperature [4, p. 38]:

$$i_0 = i_0^{ref} \cdot C_1 \cdot \left(\frac{p}{p^{ref}}\right)^{C_2} \cdot \exp\left(C_3 - C_4/T\right) \tag{2.13}$$

where C_1, C_2, C_3 and C_4 are all positive constants. Looking at the equation, increasing the pressure will increase i_0 by a certain factor dependent on the exponent C_2. Increasing the temperature yields an exponentially higher i_0.

For the above reasons, higher air pressure and stack temperature will generally increase the OCV and reduce the activation losses as well as the initial voltage drop due to internal currents. This is visualized in the figures below:

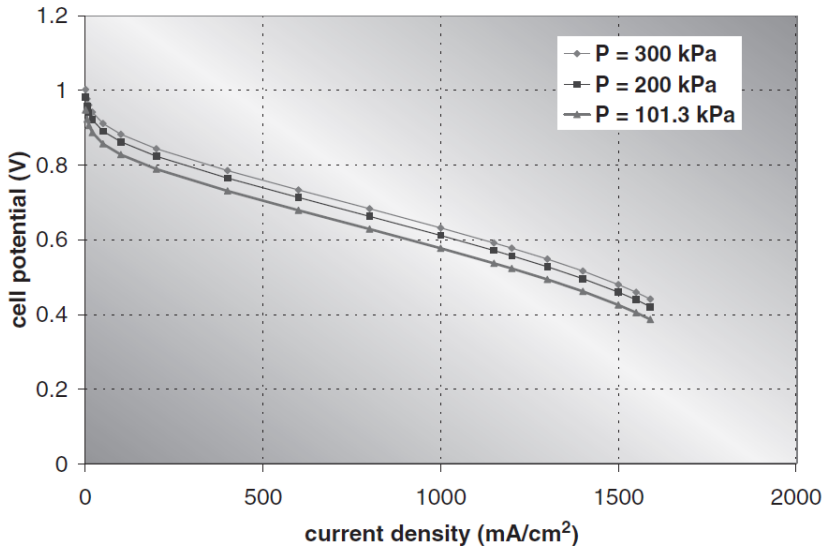

Figure 2.7: Effect of Increasing Operating Pressure on the Polarization Curve [4, p. 57]

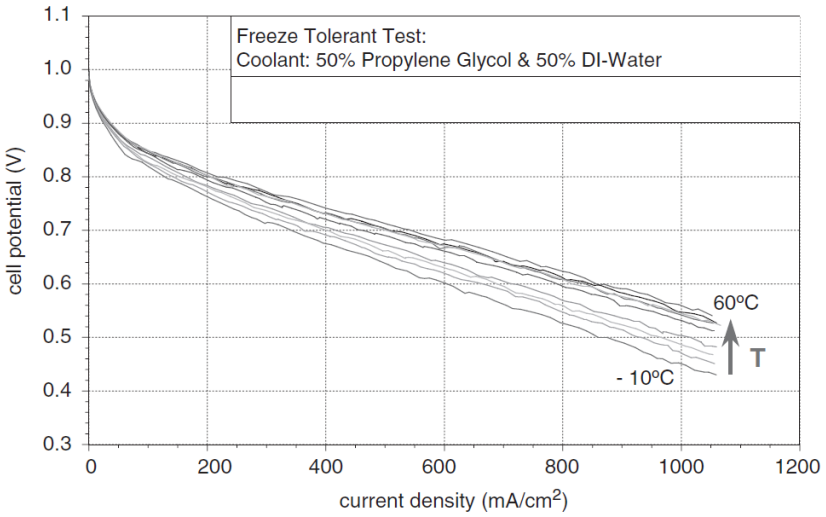

Figure 2.8: Effect of Increasing Operating Temperature on the Polarization Curve [4, p. 59]

The importance of relative humidity for the performance of a fuel cell is discussed in the next subsection.

2.2.2 PEM Fuel Cell Water Management

The proton conductance of the polymer electrolyte membrane increases (and therefore the ohmic losses decrease) with increasing water content within it [4, p.81]. However, when it comes to water presence and movement inside the fuel cell, there are various ways this occurs

as explained in Section 4.4 of [3], and they are visualized below:

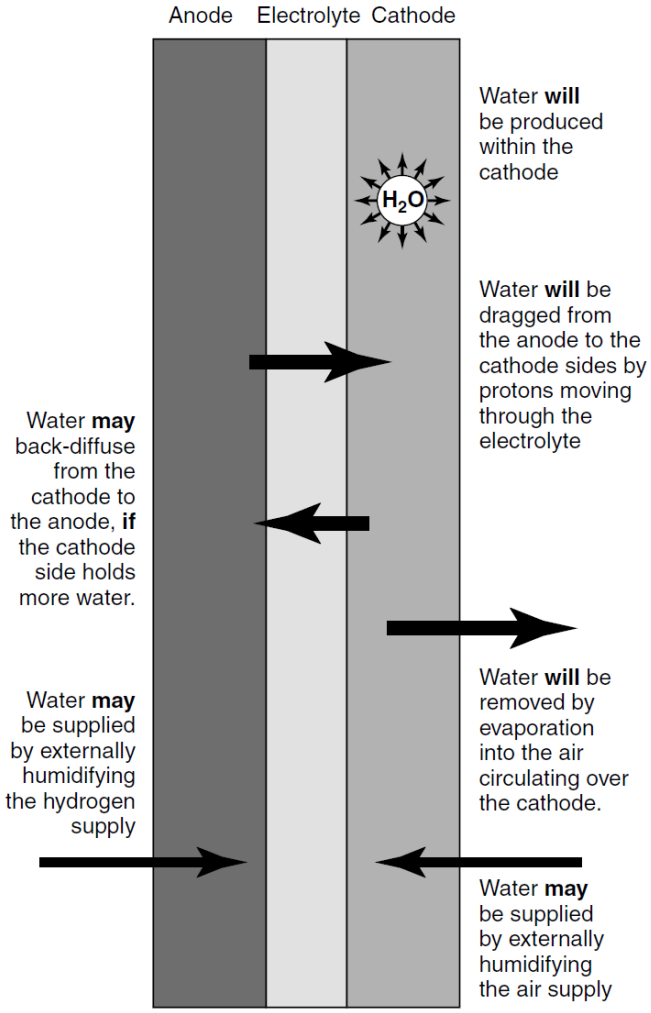

Figure 2.9: The Different Ways of Water to Move Within the Fuel Cell [3, p. 77]

Water production takes place at the cathode side due to the electrochemical reaction, which provides a supply of water molecules that can be used for keeping the membrane wet.

One way for water to move is that H^+ ions (i.e. protons) going through the PEM pull water molecules with them. That is referred to as electro-osmotic drag, and can extend from one up to five water molecules per proton. This means that at high current densities, the anode side of the membrane can get too dry while the cathode side is sufficiently hydrated. That is why external humidification of the hydrogen side can be beneficial.

There is always a certain amount of water cross-over from the cathode side to the anode side, which depends on the water concentrations on both sides and the membrane thickness. This water thus enters the excess hydrogen stream and needs to be separated out in order for the

hydrogen recirculation to function properly.

A lot of water can be evaporated into the excess air, which can be a good thing to prevent flooding of the air channels, but also a bad thing if too much water is removed from the membranes. The amount of water evaporation depends on the temperature and relative humidity of the air, which is explained in more detail now.

At higher temperatures, air is able to hold increasingly more water. If the air is too dry, it will take up too much water from the membranes which causes proton conductance to reduce and membrane durability to decrease.

To prevent this, as mentioned before, external humidification of the incoming air can be performed. It can be said that when a fuel cell stack operates at temperatures above 60°C, in general it is always necessary to have an air humidifier in the system as there will be no sufficient water production to prevent the membrane from drying out [3, p. 84].

The maximum amount of water vapor that air can hold at a certain temperature is proportional to the water saturation vapor pressure. This is plotted in the following graph[3]:

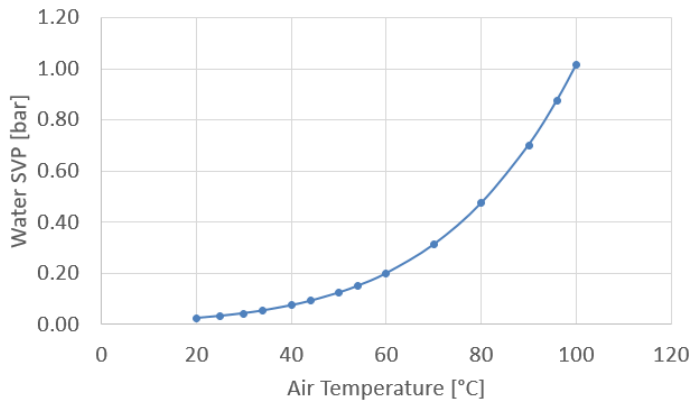

Figure 2.10: The Saturated Water Vapor Pressure (SVP) as a Function of Air Temperature

Clearly the trend is superlinear. Hence for a fixed amount of water content, when the air heats up, it gets very dry. The degree of dryness can be expressed by the relative humidity, which is simply the ratio between the actual partial pressure of the water vapour held by the air and the saturation vapour pressure at its specific temperature [3, p. 78]:

$$RH = \frac{p_{H_2O}}{p_{H_2O,sat}} \tag{2.14}$$

The lower the relative humidity, the dryer the air, and thus more water would evaporate from the membranes. In order to prevent this, the rule of thumb says that the stack exit air relative humidity should be between at least 80% but not above 100%, otherwise liquid water floods the cell channels [3, p. 80]. The air humidifier has to be designed properly such that the

[3] https://www.engineeringtoolbox.com/water-vapor-saturation-pressure-d_599.html

water loop stays in balance: it has to be able to sufficiently humidify the stack inlet air with the available water content in the stack outlet air. This is crucial to keep the stack working at high efficiencies.

If the fuel cell stack operates at higher pressure, less water is needed to achieve the same humidity which reduces performance and sizing requirements on the external humidifier [3, p. 80]. This is another benefit of operating the fuel cell at higher pressures, next to the voltage increase mentioned before.

2.3 Waste Heat Recovery in PEM Fuel Cell Systems

Waste heat is a by-product of any process involving transforming energy, as no system is 100% efficient (2^{nd} law of thermodynamics). The temperature level of the waste heat indicates its quality: high grade waste heat comes from processes operating at temperatures greater than 400°C, medium grade waste heat is between 100°C and 400°C and low grade waste heat is below 100°C [4]. Recovering low grade waste heat is difficult due to the low temperature level and therefore the low energy potential w.r.t. the ambient environment. Since a PEM fuel cell system operates at temperatures below 100°C, its waste heat is of low grade.

2.3.1 Energy Flows in a PEM Fuel Cells System

In order to understand how the waste heat in a PEM fuel cell system could be recovered, it is important to first visualize all the energy flows and its different forms. A so-called Sankey diagram is a great way of doing that, and such a diagram is shown in figure 2.11 for a hypothetical PEM fuel cell system and a hypothetical internal combustion engine (naturally aspirated diesel) at full load, in order to compare them.

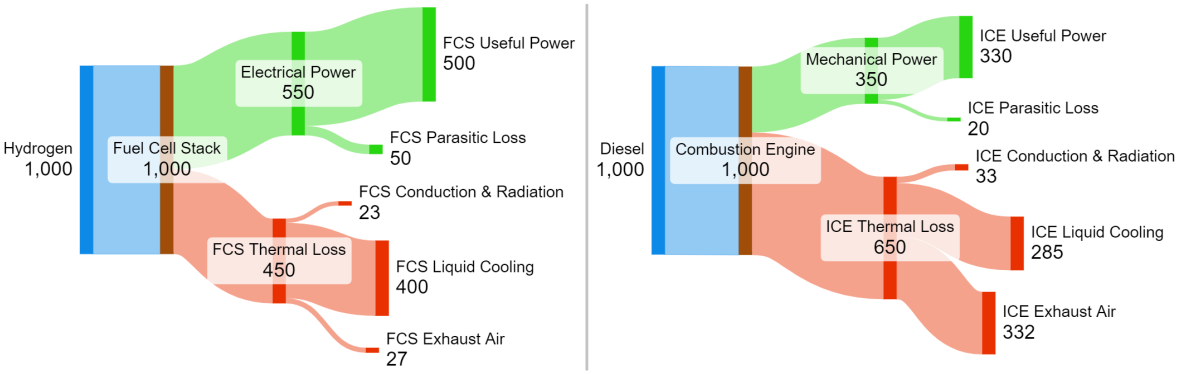

Figure 2.11: Sankey Diagram of a Hydrogen PEM Fuel Cell System (Left) and a Diesel Engine (Right), Both at Full Load

[4] https://www.thermopedia.com/content/1250/

For both energy conversion systems, the energy flows are similar. The hydrogen or fuel carrying all the energy goes into the conversion system (either the fuel cell or the engine), and from there splits up in useful power (electrical or mechanical, respectively) and waste heat (thermal loss).

In terms of useful power, both systems have to supply power to auxiliary systems to keep their respective power cycles in operation. The fuel cell system has to electrically power its air compressor and other devices, which costs about 9-10% of the gross output power. The combustion engine has to power its oil and coolant pumps, valvetrain and other devices, which costs about 5-6% of total output power. The fuel cell system therefore sees a higher parasitic load, but is more efficient in terms of converting fuel into useful power.

When it comes to waste heat, the situation is quite different. Due to the high operating temperature (∼400-500°C exhaust) of the combustion engine, the exhausts can take up about half of the produced waste heat (332/650), and most of the rest goes into the cooling water. For the fuel cell system operating at temperatures below 100°C, only around 6% of the waste heat goes into the exhaust, while most of it goes into the coolant. This has to be kept in mind when analyzing viable ways to recover heat in this kind of system.

There exist many WHR solutions used in the energy, industry and automotive sectors. Specifically regarding automotive (as per the aim of this research), multiple WHR options have been identified. These are listed below:

- Turbocharging using air exhaust energy
- The Organic Rankine Cycle (ORC) power system
- Vapor compression cycle (VCC) and vapor absorption cycle (VAC) systems
- Thermo-electric generators (TEGs)

Each of the above options will now be elaborated upon, and their specific application in PEM fuel cell systems will be explored.

2.3.2 Turbocharging with Exhaust Gas

In automotive ICE applications, turbines have been used extensively for recuperation of exhaust energy with the purpose of increasing air pressure (effectively increasing air density and thus oxygen concentration) into the engine in order to create more power [5].

This is referred to as turbocharging: the turbine converts the enthalpy of the exhaust flow into rotational energy, thereby rotating a compressor wheel via a shaft that moves more air into the engine (boost pressure), which allows more fuel to be burned and increases engine power. This can be seen in Figure 2.12.

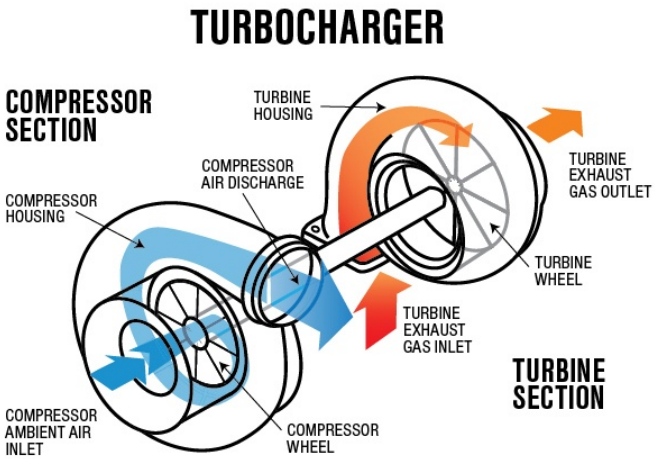

Figure 2.12: Schematic of a Conventional Turbocharger

To characterize the performance of a certain turbocharger, the so-called compressor and turbine maps are generally used. Examplary compressor and turbine maps are shown in Figures 2.13 and 2.14 respectively.

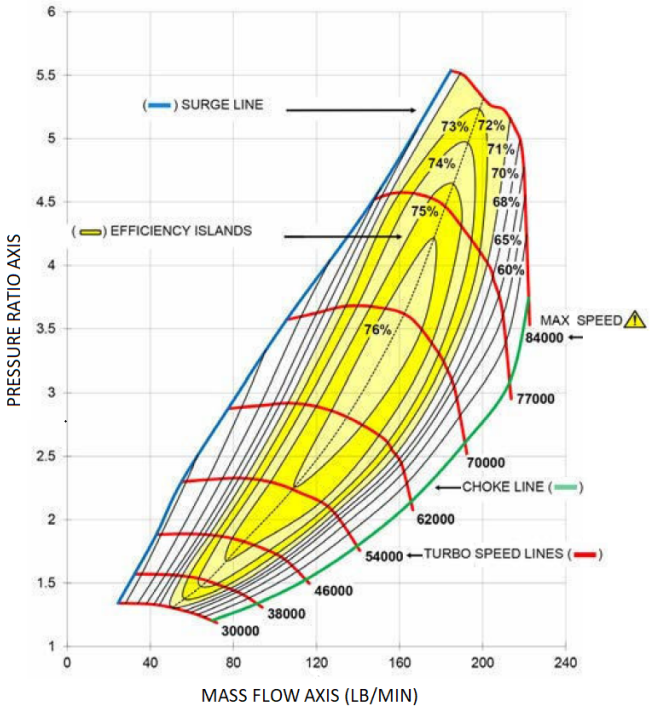

Figure 2.13: Examplary Turbocharger Compressor Map [12]

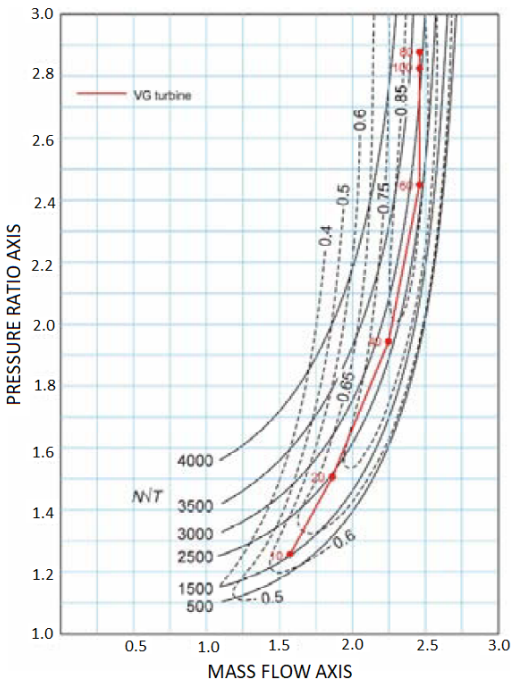

Figure 2.14: Examplary Turbocharger Turbine Map [13]

As can be seen in Figure 2.13, the x-axis shows the air massflow through the compressor, and the y-axis shows the pressure ratio over the compressor. The red lines show the 'turbo speed', which is the rotational velocity of the turbine and compressor wheels (they are the same as they are mounted on the same shaft). An operating point of a compressor wheel is completely defined by three variables. At a certain air massflow (due to the engine operation) and speed (due to turbine rotation) the compressor will deliver a given pressure ratio.

The red line (84000RPM) on top of the map shows the maximum speed which cannot be exceeded. This is one limit of the map. Another limit is the blue 'surge line' connecting the points of highest pressure ratios: if the pressure ratio at a certain massflow would exceed this line of the map, flow reversal occurs, which should be avoided at all times. The final limit of the map is the green 'choke line' connecting the points of maximum massflow. Higher massflows at a certain pressure ratio are not possible due to the sizing of the compressor, it would have to be larger to achieve this.

The final interesting part of the compressor map in Figure 2.13 concerns the efficiency islands in yellow. The highest compressor efficiency here is about 76% and is achieved when operating in the central region of the map. If operation occurs closer to the surge region, or towards the choke region, it is clear that the efficiency drops very quickly to 60% and lower. It is therefore not desired to operate in those two regions, and the engine and its turbocharger should be matched accordingly.

Analogous to the compressor map, the turbine map in Figure 2.14 shows the same parameters for the turbine wheel. Here the solid black lines are the turbine speeds, the dotted black lines are the turbine iso-efficiency curves and the red line shows the position of the variable inlet guide vane (see below). There seems to be a vertical asymptote at a massflow of around 2.75 (unknown units). This shows that no matter how large the expansion is (e.g. by lowering the turbine outlet pressure keeping the total inlet conditions constant), there will not be more flow through the turbine. This is the choke condition of the turbine wheel and is defined by its size, just as with the compressor

Turbochargers in PEM Fuel Cell Systems

There are two main ways to integrate an exhaust turbine into a fuel cell system: connecting a turbine wheel directly to the E-compressor (making an E-turbocharger) or integrating a turbine wheel separately in the flow (free turbocharger). For the latter option, the turbine could be connected to its own compressor wheel, or to an electric generator. Figure 2.15 shows an E-turbocharger setup and one (of many) possible free turbocharger setup.

The E-turbocharger setup (left schematic) has the benefit of being compact. The downside of this layout is the more complex design, as now all three components - the compressor, turbine and E-motor - have to be designed to operate efficienctly together. This is more challenging than only matching a compressor with an E-motor [10, p. 6].

The free turbocharger setup (right schematic) has the benefit of using a separate conventional turbocharger, removing the constraint of needed a turbine designed to work with both the

compressor and E-motor. This setup is essentially a two-stage compression system with a single turbine stage, and is also referred to as the serial booster topology [10, p. 7].

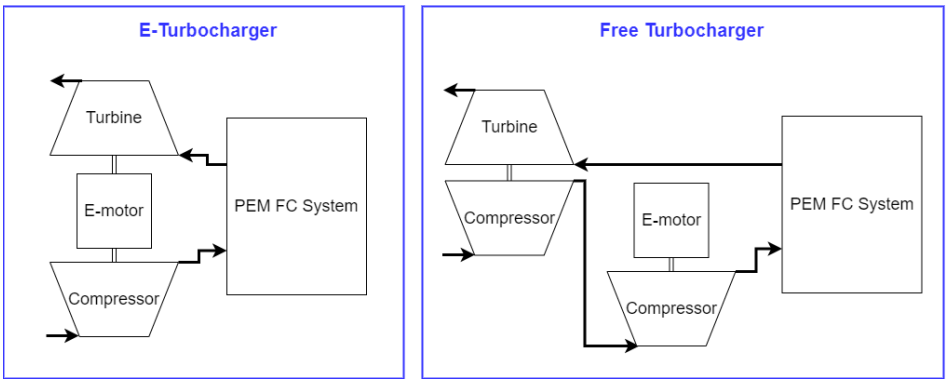

Figure 2.15: Various Ways for Integrating a Turbine in a PEM FC System

The focus of this research was to investigate the E-turbocharger setup, since multiple OEMs have prototypes of E-turbochargers available (e.g. BorgWarner[5], Cummins[6] Fischer[7], IHI[8] and Pankl[9], among others). A picture of a fuel cell E-turbocharger from Fischer Fuel Cell Compressor AG is shown below:

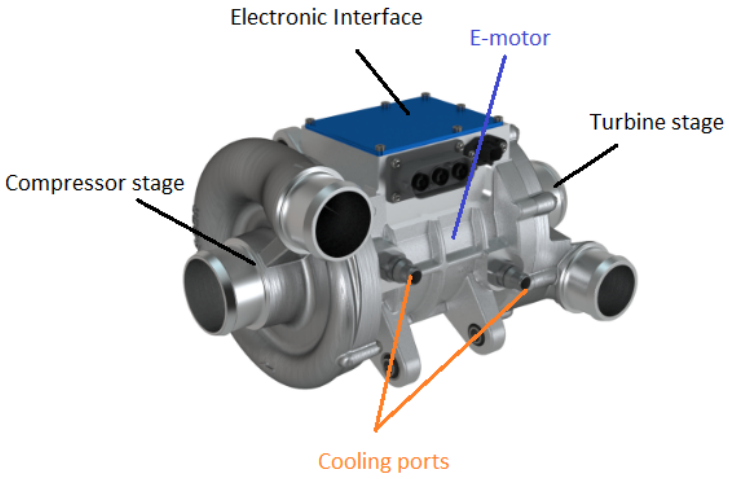

Figure 2.16: The EMTCT-90K AIR GEN5 from Fischer Fuel Cell Compressor AG

Contrary to ICE applications, a PEM fuel cell system exhaust turbine cannot fully power the compression since the temperature of the exhaust air is very low and therefore also its energy content, as can be seen in the Sankey diagrams in Figure 2.11.

[5] https://www.borgwarner.com/technologies/electric-boosting-technologies
[6] https://www.emobility-engineering.com/cummins-develops-fuel-cell-e-turbocharger/
[7] https://www.fischer-fuelcell-compressor.com/en/products
[8] https://www.ihi.co.jp/turbocharger/en/products/electric_turbocharger/index.html
[9] https://pankl.com/racing/en/products/charging-systems/

Prior research has shown that using an E-turbocharger setup in hydrogen PEM fuel cell systems, around 30-40% of necessary compression power could be provided by the turbine [14][15], with the most optimistic estimates in literature indicating 50-60% of electrical compression power reduction [16, 17, 6].

Regarding the impact on a system level, it has been numerically estimated for automotive systems with various stack sizes to lead to 3.5-7% increase in fuel efficiency at same net power [18, p. 11][10, p. 6]. The highest results of 7% are due to high assumed expander efficiencies (∼90%)[13, p. 4]. A 14-16% increase in net power at same fuel consumption was reported in some literature [17][10, p. 6].

Fixed Turbine Geometry vs Variable Turbine Geometry for E-turbochargers

Two studies have covered the use of variable turbine geometry (VTG) versus fixed turbine geometry (FTG) specifically for fuel cell E-turbochargers, one numerical [19], and one experimental [14, p. 9] in nature.

The numerical study compared an FTG E-turbocharger turbine with two types of VTG turbines: a pivoting vane VTG and sliding nozzle VTG. It was found that the pivoting vane VTG performed best, and was able to obtain higher efficiences compared to the FTG turbine in off-design points, effectively broadening the efficient operating range of the E-turbocharger. It was concluded that a VTG E-turbocharger would also be beneficial as the backpressure valve becomes unnecessary, since the VTG allows for backpressure regulation.

The experimental study showed similar results, measuring increased turbine efficiencies for VTG at higher pressure ratios and variable air massflows compared to the FTG turbine. However, at the design point, the FTG performs the best due to the lower gap losses that inevitably increase when using VTG. This research concluded that FTG was the best way forward, since lowest design complexity was desired as well as steady-state operation, though the target of the study was a non-automotive application.

Summarizing, the integration of an E-turbocharger in a PEM fuel cell air processing system seems to have system performance benefits with limited addition of system weight and size. Therefore, this concept was chosen as a possible option to increase the efficiency of automotive PEM fuel cell systems. The adopted methodology to assess the efficiency gains that the E-turbocharger may enable is explained in Chapter 3.

2.3.3 The Organic Rankine Cycle Power System

The organic Rankine cycle (ORC) is a closed thermodynamic cycle that implements the same working principle as the steam Rankine cycle (SRC) . The basic process flow diagram of the ORC is shown in Figure 2.17. The operating principle is as follows:

Waste heat is fed to an evaporator that vaporizes the working fluid, which then goes through an expander to convert the thermal energy into mechanical power. After that, the working

fluid is condensed using a heat sink, such that it can be pumped around again in liquid form to the evaporator to repeat the cycle. The energy input of the cycle is the waste heat at the evaporator and the mechanical work of the pump, while the output is the power delivered by the expander which is usually connected to an electric generator.

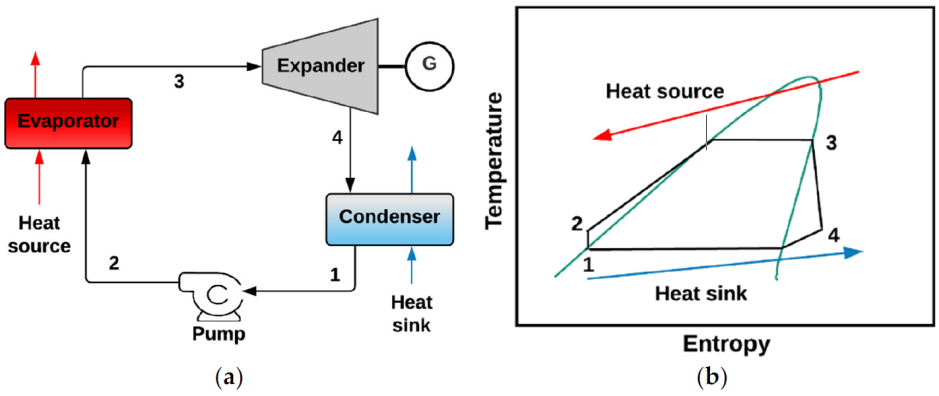

Figure 2.17: Layout of the Basic Organic Rankine Cycle [20, p. 3]

The main difference between the ORC and the original SRC, is the working fluid. The SRC works with steam, and is suitable for processes featuring temperatures of around 400°C and more [21, p. 1]. The ORC, however, employs organic working fluids, which feature a lower boiling point. The ORC therefore makes it possible to recover heat at temperatures as low as 60°C and up to 400°C depending on the working fluid and condenser pressure [21, p. 2][22], with most of the plants featuring a thermal source with maximum temperature between 150°C and 300°C [20, p. 4][23, p. 2].

There are three main types of ORC working fluids: wet, isentropic and dry fluids. Their main distinction lies in the shape of the vapor saturation curves on a T-s diagram, as shown in Figure 2.18 below.

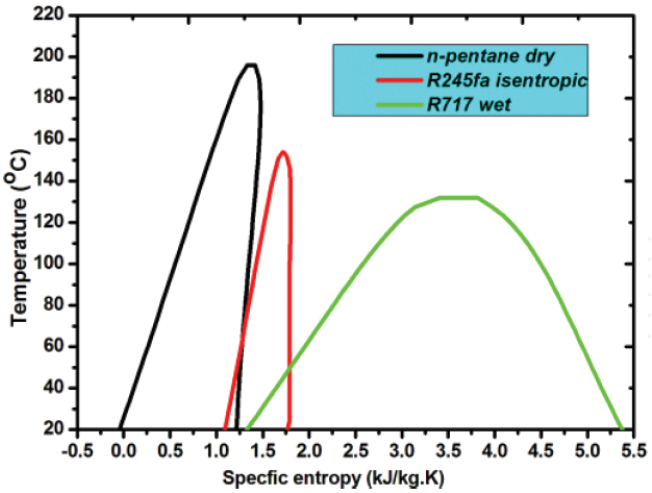

Figure 2.18: The Three Main Types of Organic Working Fluids [24]

Wet fluids have the advantage of higher latent heat of vaporization at a certain temperature. This means that more heat can be taken up for the same fluid massflow rates (which affects pump work). This leads also to more compact equipment [25]. The main downside of wet fluids however is that during expansion, condensation can occur, due to the negative slope of the saturation curve in the T-s diagram (right part of green curve in Figure 2.18). The liquid droplets are expected to damage the turbine. To prevent this, significant superheating of the wet fluid is usually performed which necessitates higher waste heat temperatures and larger evaporators (increasing size and cost) [26, p. 6].

Isentropic and dry fluids do not have this problem. Without much or even any superheat, there is no risk of fluid condensation along the expansion process in the turbine [27, p. 3]. This could also lead to better cycle performance in certain conditions, and is one of the reasons why isentropic and dry fluids are more suitable for recuperation of low-temperature waste heat [25].

Zeotropic fluids, which are mixtures of wet/isentropic/dry fluids can lead to better ORC performance compared to pure fluids, but not always [20, p. 5]. However, the selection of the correct working fluid has to be investigated on a case-by-case basis. There is no silver bullet [24][27, p. 3-4].

Cycle efficiencies of industrial ORC plants can go up to 29% [20, p. 10], but that is achievable for high temperature levels of the waste heat source as well as large capacity of the ORC installation. For automotive applications, where constraints on weight, size and cost are much stricter, the story is different.

In prior investigations, ORC cycle efficiencies in automotive setups ranged between 3-10% with most around 6% [28][29][30][31]. Usually, ORCs for ICE applications used the engine exhaust air as thermal source, as the exhaust gas stream features both the the largest thermal energy and temperatures [26]. Sometimes also the coolant thermal energy was exploited [5].

For PEM fuel cell systems, the best thermal source for the ORC system would be the fuel cell coolant, as it has the highest temperature and waste heat energy content (as seen in Figure 2.11). However, compared to the ICE ORC cycle efficiencies which have higher evaporator temperatures, for automotive PEM fuel cell systems an ORC would have even lower cycle efficiencies.

Considering the high additional costs, weight, size and slower dynamics then, integrating an ORC in a PEM fuel cell system is deemed much less attractive than adopting an exhaust turbine. However, the advent of high-temperature PEM fuel cell stacks operating between 160-200°C, along with improvements on ORC technology might change that in the future.

2.3.4 Vapor Compression and Absorbtion Cycle Systems

Vapor compression and absorption cycles (VCC and VAC, respectively) are closed thermodynamic cycles also known as 'heat pumps'. They move heat from one place, namely the

evaporator, to another one, namely the condenser. What differentiates the two cycles is what happens in between the evaporator and condenser. Both cycles are now discussed.

Vapor Compression Cycles

The VCC heat pump features a gas compressor that needs to be powered electrically. The basic working principle is shown in the following schematic:

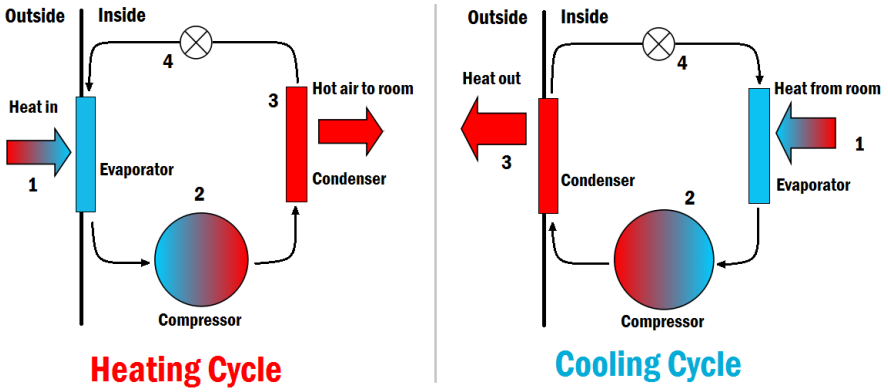

Figure 2.19: The VCC Heat Pump in Heating (left) and Cooling Mode (right)[10]

Heat is taken up by the working fluid at the evaporator. From there, the fluid goes through a gas compressor that compresses and superheats the working fluid (instead of expanding in a turbine). At this point, the working fluid has a higher temperature compared to the hot source at the evaporator. At the condenser, the heat is released at this higher temperature. A heat pump can be built as a reversible setup: the flow of the working fluid can be reversed, such that the evaporator becomes the condenser and vice versa. This way, a heat pump can both heat or cool an inside space, as shown in Figure 2.19.

VCC heat pumps are used in many heat, ventilation and air conditioning (HVAC) applications on both industrial scale as well as building heating/cooling [32] and automotive HVAC systems [33]. They are very efficient in heating and cooling by using only a small amount of electricity compared to the heat being added or removed. The performance of a heat pump is usually represented by the coefficient of performance (COP), which is defined as follows:

$$COP = \frac{\dot{Q}_H}{P_{HP}} \tag{2.15}$$

where $\dot{Q}_H$ is the heat released at the condenser and P_{HP} is the electrical power needed to drive the compressor. The theoretical maximum limit for the COP is taken from the ideal Carnot process where the evaporator and condenser temperatures are constant, denoted as T_C and T_H respectively. The COP in that case is [34]:

$$COP_{Carnot} = \frac{T_H}{T_H - T_C} \tag{2.16}$$

[10] https://energyeducation.ca/encyclopedia/Heat_pump

which means that the smaller the temperature difference with which the heat pump works, the better its performance. The COP values of real VCC heat pumps for automotive HVAC usually range between 3 and 5 [35].

In this research however, the focus is not on HVAC, but WHR. One possible advantage that VCC may enable is that it can be used to increase the temperatures of the waste heat source, which, as aforementioned, is problematically low for PEM fuel cell systems. This may be useful to increase the power generated by the exhaust turbine: the idea is to feed a heat pump with thermal energy from the fuel cell stack coolant (or another source of thermal energy) to heat up the exhaust air before entering the turbine.

Normal automotive HVAC heat pumps would not be appropriate, as they work at temperatures lower than 70°C (PEM fuel cell stack operating temperature). For this specific concept, high-temperature heat pumps have to be used that could operate at 70°C and higher. Such heat pumps can be found in industry, and have COPs ranging from 2.4 to 6.5 depending on temperature lifts ($T_H - T_C$) which usually range between 95°K and 30°K [36].

This solution was not found in previous research. So a simplified assessment of its potential gain was carried out. The methodology and results of this investigation can be found in Section B.1 of Appendix B.

Vapor Absorption Cycles

The VAC heat pump features a so-called 'thermal compressor' consisting of a subsystem of heat exchangers and a liquid pump. A simple schematic of the cycle is shown below[11]:

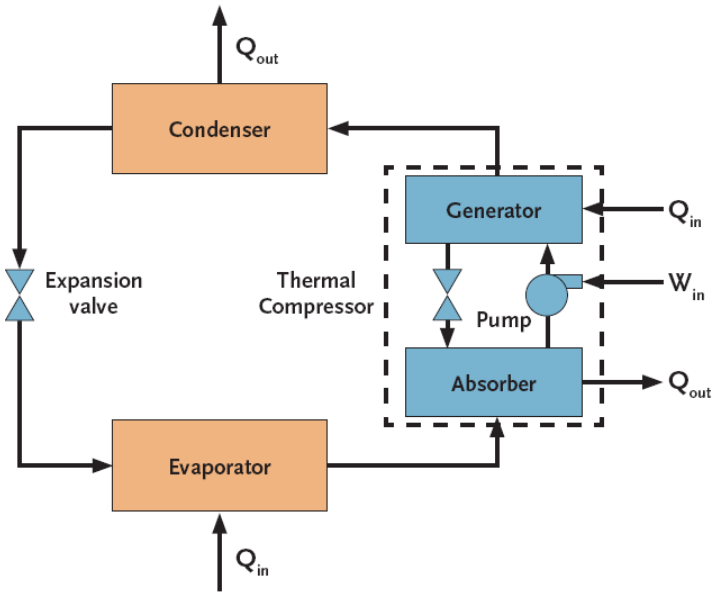

Figure 2.20: The VAC Heat Pump with Thermal Compressor

[11] https://www.cibsejournal.com/cpd/modules/2009-11/#:~:text=In%20practice%20a%20typical%20COP,for%20a%20vapour%20compression%20system.

After the heat uptake in the evaporator, the gaseous working fluid enters the absorber, a heat exchanger where the working fluid in vapor state is absorbed by a chemical solvent, usually lithium-bromide [37]. This process is exothermal, meaning that the absorber acts as a heat sink. At this point, the liquid lithium-bromide-working fluid mixture can be pumped around the circuit.

After the pump, a generator, given a heat input, separates the solvent from the working fluid, releasing the gaseous working fluid now at higher pressure and temperature compared to those in the evaporator. The solvent is regenerated through an expansion valve and rerouted to the absorber. The superheated working fluid goes through the condenser where it releases thermal power while condensing.

This setup is more complex than a VCC: two heat sources, two heat sinks and one electrical power source are needed (in VCC there is only one heat source and heat sink). The benefit of this cycle is that the liquid pump requires much less electrical power to circulate the working fluid. The main energy source is the waste heat, making the cycle more advantageous if electrical costs are high and sufficient waste heat is available.

Real applications are mostly found in industry, with a COP between 0.1 and 0.8 with most values around 0.4-0.5 [37]. The COP here is defined differently compared to VCC:

$$COP = \frac{\dot{Q}_H + \dot{Q}_{abs}}{\dot{Q}_C + \dot{Q}_{gen} + P_{lp}} \tag{2.17}$$

where Q_{abs} is the heat released by the absorber, Q_{gen} the heat input to the generator and P_{lp} the electrical consumption of the liquid pump. In certain applications with steam as the working fluid (at 130°C), the COP can approach 1 [38]. Those values are much lower compared to VCC due to the inefficiency of the thermal compressor. Additionally, these setups are very bulky due to the need of at least 4 heat exchangers.

Due to these reasons and the fact that VAC cannot raise the temperature of the pumped heat above the hottest heat source (which is at the generator), it does not seem very useful for the application investigated in this study.

Nonetheless, there have been prior investigations done on VAC in automotive applications for HVAC purposes. One experimental investigation of a VAC HVAC on a Nissan 1400 showed that cooling powers of around 2kW could be generated, but only when driving at sufficiently high speed to have enough exhaust heat. Additionally, the COP was around 0.09, 10-15 minutes were needed before the cylce started working, and no cooling was provided when the car was idling [39].

Another numerical investigation focused on the potential benefit of a combined VCC-VAC HVAC cycle for an ICE passenger vehicle, and found that the combined COP was higher than a VCC-only HVAC system [40]. However, the setup was very complex and bulky.

2.3.5 Thermo-electric Generators

Thermo-electric generators (TEGs) utilize the Seebeck effect to produce electricity from a temperature difference, or, on the opposite, they exploit the Peltier effect to provide heating or cooling given an electric power input [41]. TEGs are made up of conductive materials, and when a temperature difference exists over them, the electron concentration will be higher in the cold side compared to the hot side since at lower temperatures the particles move slower (and remain longer in one place).

This results in an electric potential difference between the cold and hot side at open circuit. When the thermoelectric material is connected to a closed circuit, the current flows from the cold side to the hot side [41].

The building block of TEGs are n- and p-type Peltier elements, which are connected in series to create a TEG that has a distinct cold and hot side and can generate useful electric potentials. This is shown in the schematic below:

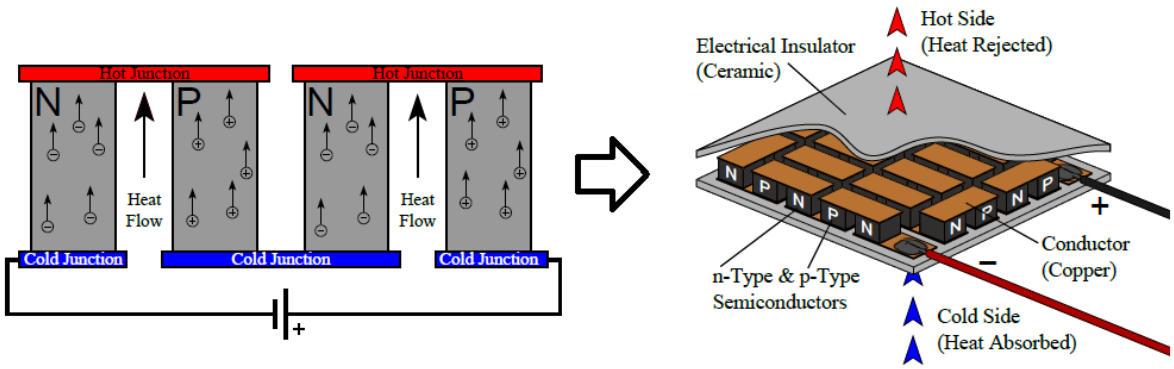

Figure 2.21: Peltier Device [41]

The efficiency of TEGs is very low, usually around 5-7% [42][43, p. 23] with peak values of 10-11% documented in literature [44][45]. In automotive ICE applications, where temeprature differences of over 100°C are easily achievable, TEGs only generated electric power of several hunderds of Watts, only exceeding the 1kW mark at full engine power [42, p. 4][46]. This performance is way to low, especially considering that temperature differences in PEM fuel cell systems are only around 50°C. Therefore this technology is not considered any further.

Chapter 3

Modeling Methodology

To answer research questions 2, 3 and 4 formulated in Section 1.2, a full fuel cell air processing system model has been built using the AVL Cruise M software. First, a brief overview of the available system data and the purpose of the simulation study is given. Afterwards a complete explanation of the various models in AVL Cruise M is provided.

3.1 Notes on Available Measurement Data

There were three main categories of available measurement data used to build, calibrate, verify and validate the different models. The first category was a collection of complete vehicle measurements, the second consisted of polarization curve measurements from the fuel cell stack on a testbench, and the third category included measurements resulting from the testing at a testbench of different E-(turbo)compressors.

3.1.1 Complete Vehicle Measurement Data

The reference fuel cell (air processing) system is used in multiple vehicle types: a passenger car, a city bus and a commercial truck. As the passenger vehicle was accessible, it was used to generate system data. A measurement campaign was executed on a test ground, and system data at steady state points ranging from 10kW to 97kW stack power was collected. These measurements contained data such as:

- air temperatures and pressures throughout the air processing system
- air compressor data such as speed, electrical input power and intake massflow
- coolant inlet and outlet temperatures for the intercooler and the fuel cell stack

- fuel cell stack data such as air stoichiometry, electrical current and voltages

This data was used both for component model calibration and full system model validation.

3.1.2 Stack Polarization Curve Measurement Data

The fuel cell stack itself was tested on a testbench setup, yielding measurements such as:

- air massflow and stoichiometry
- air temperature and pressure at stack inlet and outlet
- stack coolant massflow and inlet and outlet temperatures
- electrical current and voltage

This data was used to develop the fuel cell stack model.

3.1.3 E-(turbo)compressor Measurement Data

Since the air compression system was the main focus of the research, specific data regarding this subsystem was also obtained. The original E-compressor as well as two different prototype E-turbochargers were tested on the same testbench by a third party, and access to the corresponding data was obtained. The E-(turbo)compressor dataset contained the following parameters:

- air massflow through compressor and turbine stages
- air temperature and pressure at compressor and turbine inlets and outlets
- E-motor speed and electrical input power
- E-motor coolant massflow and inlet and outlet temperatures
- calculated parameters such as pressure ratios and isentropic efficiencies

This data was used to develop the E-(turbo)compressor models used in the simulations.

3.2 Overview of the Simulation Approach

In order to provide an answer to research question 2 (Section 1.2), it was necessary to first develop a model for the current air supply system that uses an E-compressor only, such that

a consistent comparison could be made with the model of the turbochagerd system concept. This initial system model was called the 'baseline model', and its aim was to mimic the behavior of the fuel cell air supply system currently in use on the vehicle.

The comparisons would be done at three different power levels of the stack, namely about 50kW, 70kW and 97kW.

The results of the simulations with the baseline model could be validated using measurement data from the real reference system at the three power levels. Once successfully validated, the baseline model served as basis for the development of the system model of the turbocharged configurations, and as reference to which it would be compared.

3.2.1 Two Different Turbocharger Prototypes

For the turbocharged models, two different E-turbocharger prototypes were analyzed. The first one is of a bigger size and is indicated as 'ETC1', while the other one with smaller compressor and turbine diameters is indicated as 'ETC2'. Their respective compressor and turbine maps are compared in Figure 3.1.

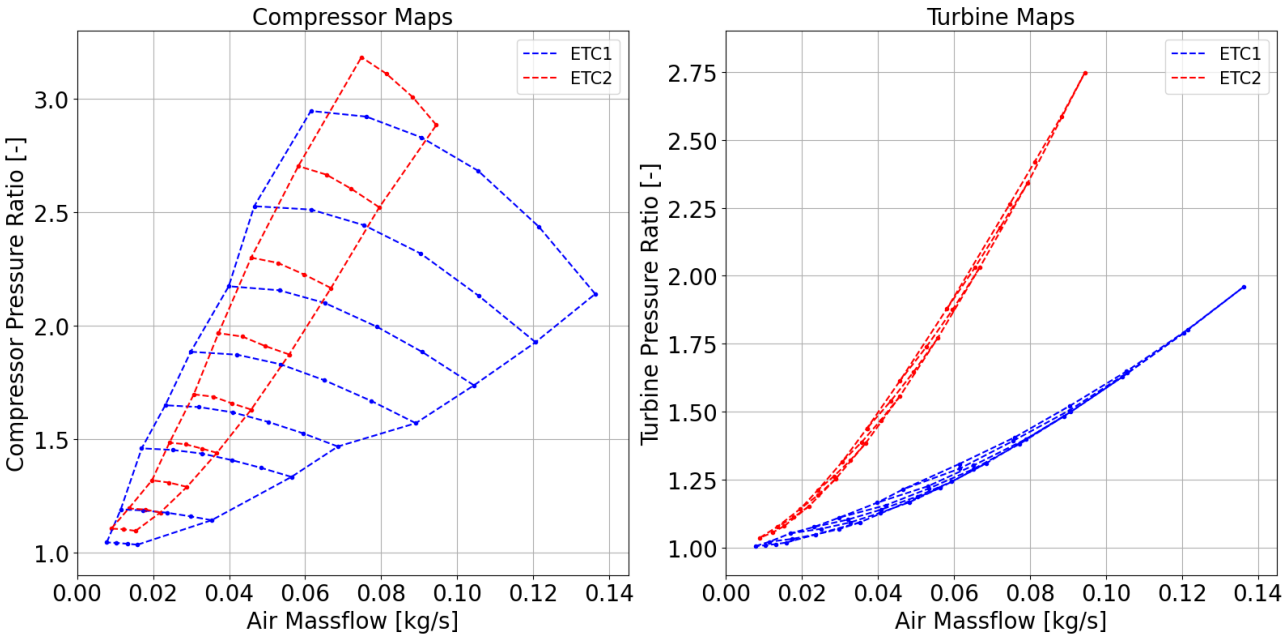

Figure 3.1: Compressor and Turbine Maps of ETC1 and ETC2 Prototypes

It can be seen in the left plot that due to its bigger size, the compressor of ETC1 (blue) has a much wider operating range than the one of ETC2. Its surge line lies slightly higher and its choke line much lower compared to ETC2. Additionally, ETC1 has a higher maximum

air flow rate. The choke line of the ETC2 compressor lies just above the middle of the ETC1 compressor map, meaning that, at same massflows, ETC2 will most likely operate at higher pressures compared to ETC1.

The same considerations apply to the case of the turbine maps (right plot). Since the turbine of ETC2 is smaller, at same air flows, it will require a much higher inlet pressure (granted the outlet pressure is constant), as the red turbine map lies significantly above the blue one. The differences in the geometry of the two E-turbochargers are highlighted in Table 3.1, including amount of compressor and turbine blades as well as the diameters of the inlet and outlet connections.

Table 3.1: Comparison of Geometries of ETC1 and ETC2 Prototypes

	Compressor			Turbine		
Prototype	**# blades**	**Øin [mm]**	**Øout [mm]**	**# blades**	**Øin [mm]**	**Øout [mm]**
ETC1	7	50.3	36.9	9	42.2	60.3
ETC2	10	43.9	40.5	11	35.0	50.0

Starting from this information, the expectation was that ETC2 would outperform ETC1 at the lower air massflows (thus power levels) and the other way around at the higher air massflows.

The turbocharged system models were verified by analyzing if the estimated output of the E-turbochargers matched with the behavior observed in the experiments at the testbench.

3.2.2 Increasing the Turbine Inlet Temperature

In order to provide an answer to research question 3, test bench data performed with increased turbine inlet temperatures was needed. Fortunately, the dataset of ETC1 contained exactly that information. At three different air masslfows corresponding to approximately 50kW up to more than 100kW, the turbine inlet temperature was varied between 50°C and 200°C.

However, data for temperatures above 150°C were not analyzed, as for current vehicles in which this fuel cell system is used, the available waste heat does not exceed this temperature level. The different turbine inlet temperatures that were simulated in the end were: the default temperature (this value ranged between 50 and 60°C), then 80°C, 100°C, 120°C and finally 150°C. The way the turbine inlet temperature was raised in the model will be discussed in Section 3.8. This allowed to quantify the effect of increased turbine inlet temperatures on total system performance.

In Section 4.1, Table 4.1 shows all the performed simulations with their corresponding inputs.

3.3 Setup of the Baseline and Turbocharged System Models

AVL Cruise M is a software for dynamic simulations. However, this tool has been used to implement a lumped parameter model of the fuel cell powertrain and assess the system performance in off-design conditions.

This was possible because the model could be implemented without accounting for any system dynamics. All the parameters of the component models that would have implied mass or energy accumulation were neglected.

The advantage of using this software was that setting up and connecting the various component models was very easy to do with the provided graphical user interface, in addition to having simulation case parameterization and predefined component libraries that could function as examples and inspiration. This allowed for quickly simulating various cases each with their specific set of model inputs, such as running the turbocharged powertrain at varying ambient conidtions or with either the specs from ETC1 or ETC2.

3.3.1 High-level System Model Overview

First, the main setup and working principles of the overall system model will be discussed, and subsequently each individual component model will be described in detail. A simplified schematic of the system model of the baseline configuration with its main inputs can be seen in Figure 3.2. The figure shows the different air processing components with their connectors. Additionally, the model boundary conditions and operational inputs are highlighted in blue, together with the model inputs needed to define the characteristics of the various system components in purple.

What is not shown in the figure are most of the model outputs (green) as well as the initial conditions for air pressure and temperature at each point in the system. The former will be shown in detail in the following sections. The latter were simply set equal to ambient conditions, just how it would be in the real system before it turns on.

Additionally, one-way arrows show model inputs, and two-way arrows show model connections where the models exchange operational parameters during the simulation time.

The thermodynamic state of the air was calculated before and after each component. Moreover, the inlet and outlet of two consecutive components was considered to be the same point in the system, i.e. the compressor outlet was the same as the intercooler inlet, the stack outlet was the same as the humidifier wet inlet, etc.

The system model of the turbocharged powertrain was quite similar to that of the baseline solution. The only difference was that the pressure valve was replaced by a water separator (which was necessary to protect the turbine), and the E-compressor was swapped out for an E-turbocharger. A schematic of this system model can be seen in figure A.1 in Appendix A.

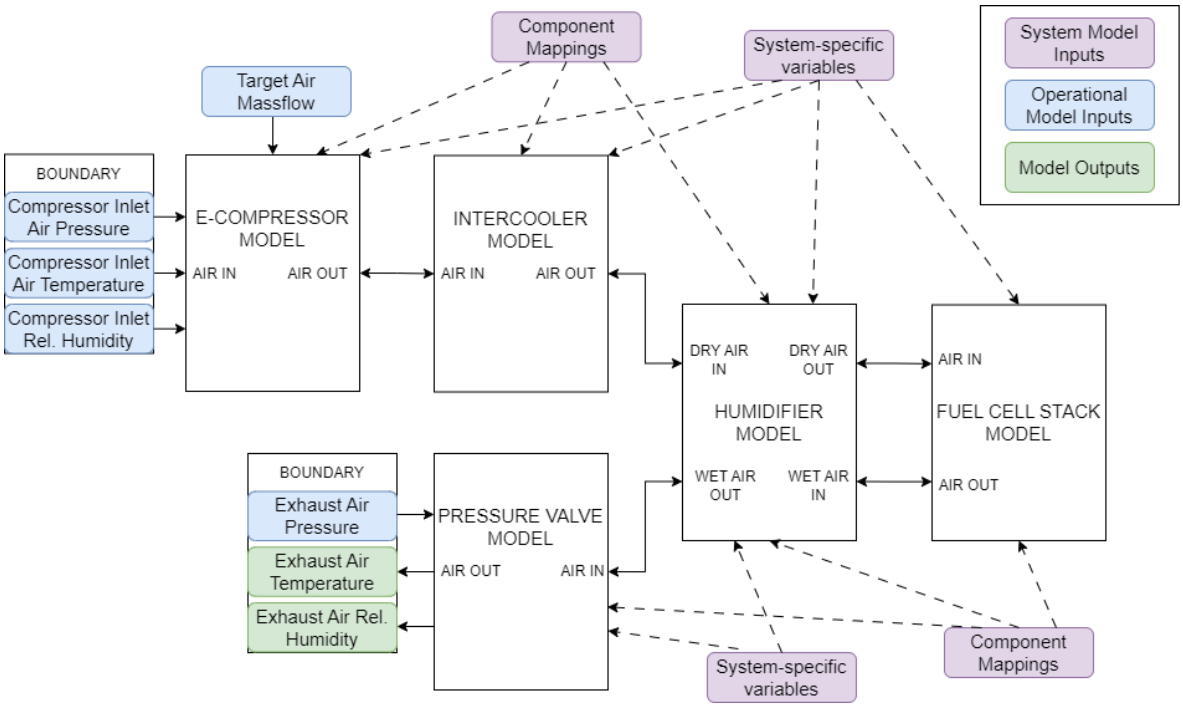

Figure 3.2: Schematic of the Complete Baseline System Model

3.3.2 Solution Method of the Model

The main control variable of the whole system is the target air massflow (indicated in blue). This is the input variable central to the calculations. As will be discussed in detail in Subsection 3.7.1, a PID-controller iteratively adjusts the rotational speed of the compressor motor in order to obtain this target air massflow. Each iteration, the resulting air massflow is then propagated further down through all components of the air processing system, in the order they appear in the system model w.r.t. the air flow path. In function of the given air massflow, each component model computed the predicted behavior and the simulation was underway. At a certain point, the PID-controller would converge to the correct speed that yields the target massflow at the resulting pressure ratio, and the simulation reaches steady state.

Boundary conditions had to be applied only at the compressor air inlet and the air exhaust. At the compressor inlet, the air pressure, temperature and relative humidity were set according to predefined conditions. They are indicated in blue as they are 'operational' model inputs, referring to the fact that those inputs vary depending on the operational conditions that are targeted in the simulation. For example, one could choose the compressor inlet air temperature to be 10°C, 20°C or another temperature, depending on what weather conditions are considered. At the exhaust, the air pressure was set to the desired value (hence blue), and the air temperature and relative humidity were set to be equal to the output of the pressure valve model (hence green, representing model outputs).

The reason why the air pressure could be predefined at both sides of the air path but not the temperature or relative humidity (they can only be prescribed at the compressor inlet) will be explained in the next section.

3.3.3 The Pressure Calculation Chain

What should be specified is the way the pressures were calculated at each point in the system model during the simulation. Since the airspeed was strictly subsonic, the speed of sound (i.e. the pressure waves) could travel both upstream through the system from exhaust to inlet and vice versa. This is visualized in the sketch below:

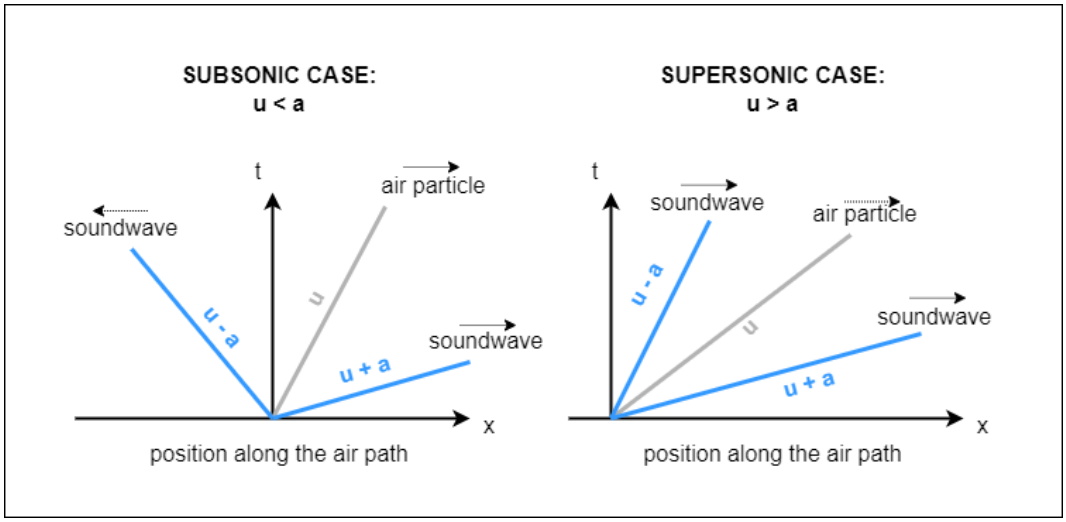

Figure 3.3: Visualization of Pressure Wave Behavior in Subsonic vs. Supersonic Flow. The Flow Speed is Denoted as 'u' and the Speed of Sound is Denoted as 'a'.

Pressure (i.e. sound) waves propagate in all directions [47, p. 130], so in this specific 1D example, the waves travel both to the left and right relative to the flow direction of the air particles. When the flow is subsonic, each component can 'feel' pressure changes that happen both upstream and downstream of the system. Hence the pressure boundary conditions were imposed at both ends of the system. When the flow would be supersonic, the pressure waves travelling to the left w.r.t. the air particles still travel to the right w.r.t. the system of reference, as can be seen in the sketch. In that case, only an upstream pressure could be set and the downstream pressure would be computed through the model [48, p. 4].

For the considered application, the flow is subsonic throughout the system. By knowning the massflow through a component, its pressure drop could be computed. Then, since the outlet pressure of the last component is a boundary condition of the model, the calculation of the pressure through the air loop starts from the last component, which is the backpressure valve for the baseline configuration. Subsequently, the inlet pressure of the last component corresponds to the outlet pressure of the component before it. Hence, the inlet pressure of the

second-to-last component can be estimated determining the pressure drop in that component, which is a function of the air massflow that is known. The process is then repeated until the compressor outlet is reached, as the compressor inlet pressure is again a set boundary condition. This calculation process is vizualized in Figure 3.4 below.

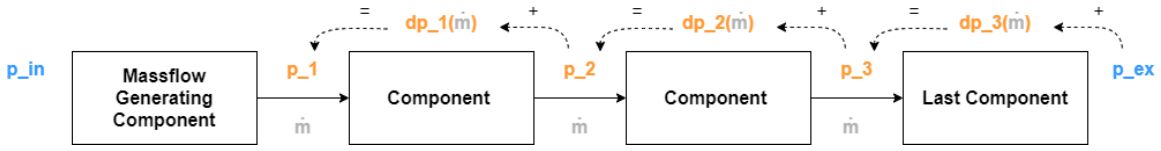

Figure 3.4: The Pressure Calculation Chain in the System Model. The Constant Boundary Pressures in Blue, Calculated Pressure (Drops) in Orange, and Massflows in Grey

For the temperatures, the values are calculated in the opposite direction (from intake to exhaust) since heat transfer works differently compared to pressure waves. A simple example: the exhaust temperature of the air can be hotter than the ambient, but the exhaust pressure will adapt to whatever the ambient pressure is.

3.4 Fuel Cell Stack Modeling

The desired functionalities of the fuel cell stack model are as follows:

- predict the change in composition and massflow rate of the air stream
- predict the change in water content in the air (water production and relative humidity)
- predict the change in air temperature (heat transfer)
- predict the pressure loss in the fuel cell stack
- predict the conversion of chemical energy into electrical energy (voltage generation at a given current)

There was no interest in the stream on the anode side of the fuel cell, as the system model is limited to the air supply loop which involves only the cathode side of the fuel cell. Information on the properties of the stream on the anode side was also not needed, since the electrical current can be one-to-one related to the air mass flow if one knows the air stoichiometry (which was the case here).

The stack voltage is the result of many effects including the physical phenomena occurring in the anode side, but since the voltage losses due to the cathode side are much larger, as explained in Subsection 2.1.5, it is usual practice to neglect anode-related voltage losses. Therefore, even without modeling the anode, one could set up an accurate stack model for the purposes of this research. In the following subsections, how each of these functionalities were implemented is laid out.

3.4.1 Fuel Cell Oxygen Consumption

The oxygen consumption of a fuel cell depends on how much current is pulled from it. From [3, p. 396], it is seen that the following relation applies:

$$\dot{m}_{O_2,c} = \frac{M_{O_2} \cdot I_{fc} \cdot n_{cell}}{4 \cdot F} \tag{3.1}$$

where $\dot{m}_{O_2,c}$ is the rate of oxygen consumption in kg/s, M_{O_2} the molar mass of oxygen in kg/mol, I_{fc} the stack current in A, n_{cell} the number of fuel cells in the stack and F the Faraday constant. The dry air mass flow that exits the fuel cell stack is then simply the difference between the dry air mass going into the stack and the amount of oxygen consumed in the stack:

$$\dot{m}_{a,fc,o} = \dot{m}_{a,fc,i} - \dot{m}_{O_2,c} \tag{3.2}$$

The total exit air massflow, however is larger, as there is also water vapour coming out of the stack. In order to quantify this, the following subsubsection explains the topic of water management inside a fuel cells stack.

3.4.2 Fuel Cell Water Management

Modeling the water management in the fuel cell stack is crucial for a system that also features a humidifier. Depending on the water content of the stack exhaust flow, the humidifier has a certain amount of water vapor to work with for humidifying the dry intake air. This in turn dictates how much water vapor enters the fuel cell stack.

As shown in Figure 2.9, there are many pathways for the water inside the fuel cell. In this fuel cell system, there is no external humidification of hydrogen, so that is not a source of water supply. From the perspective of the air path then, the stack water balance was determined to be as follows:

$$\dot{m}_{H_2O,fc,o} = \dot{m}_{H_2O,fc,i} + \dot{m}_{H_2O,fc,p} - \dot{m}_{H_2O,fc,l} \tag{3.3}$$

where $\dot{m}_{H_2O,fc,o}$ is the stack exit water massflow, $\dot{m}_{H_2O,fc,i}$ the stack inlet water massflow, $\dot{m}_{H_2O,fc,p}$ the stack water production rate (can be computed using the stack current) and $\dot{m}_{H_2O,fc,l}$ the rate of water not exiting via the stack exhaust. The amount of water going into the stack is assumed to be known since the air conditions (pressure, temperature and relative humidity) are all known inputs of the fuel cell stack model. However, there was a problem: none of the available test data included relative humidity measurements. Without this data, it was not possible to exactly quantify $\dot{m}_{H_2O,fc,l}$ of this particular stack. This in turn made it challenging to calculate $\dot{m}_{H_2O,fc,o}$. Nevertheless, an attempt was made to estimate the water loss with the available data.

The assumption was made that at any point in the 10kW to 100kW stack power range, the system would be able to provide a stack air inlet relative humidity of 85%, and that this would be sufficient to keep the water content in the fuel cells at the right level. This would only be possible if two conditions apply:

1. the stack exhaust flow going into the humidifier wet side should hold enough water vapor to theoretically bring the intake air flowing through the humidifier dry side up to 85% of RH
2. if there is enough water vapor in the exhaust to humidify the intake air to 85% RH, the humidifier had to be able make full use of that water to actually achieve this RH on the dry air side

Given the last condition, it was decided to model the humidifier as an 'ideal humidifier', see Subsection 3.6.2 for more detail.

Subsequently, if the water content in the fuel cells is at a good level, this means the stack exhaust relative humidity must be between 90% and 100% (as stated in Subsection 2.2.2). Based on this assumption, an estimation can be made on how much water is lost with the stack air stream. Equation 3.3 was then rewritten to:

$$\dot{m}_{H_2O,fc,o} = \dot{m}_{H_2O,fc,i} + \dot{m}_{H_2O,fc,p} + (1-\kappa)\cdot\dot{m}_{H_2O,fc,p} = \dot{m}_{H_2O,fc,i} + \kappa\cdot\dot{m}_{H_2O,fc,p} \quad (3.4)$$

In other words, the water lost from the airflow was estimated to be a fraction $(1-\kappa)$ of the stack water production, where κ was denoted to be the 'water flow factor', which has a value between 0 and 1. This water flow factor had to be calibrated to get the stack outlet RH between 90 and 100%.

The computation of the relative humidity given the value of κ was done as follows. As discussed in Section 2.2.2, air relative humidity is the ratio of the partial pressure of water vapour in the air and the saturation vapour pressure of water at the specified air temperature:

$$RH = \frac{p_{H_2O}}{p_{H_2O,sat}} \quad (3.5)$$

The saturation vapour pressure of the air at the stack outlet is a function of the stack air oulet temperature as shown in Figure 2.10. The actual water partial pressure in the air at the stack outlet, however, was not known and needed to be calculated.

Assuming that all the generated water inside the stack is evaporated into the air and exhausted from the stack, and taking into account the water content of the fresh air, the water partial pressure in the stack exhausts is given by the following relation [3, p. 82]:

$$p_{H_2O,fc,o} = \frac{(0.42 + \psi\cdot\lambda_a)\cdot p_{a,fc,o}}{0.21 + (1+\psi)\cdot\lambda_a} \quad (3.6)$$

where $p_{H_2O,fc,o}$ is the partial pressure of the water vapor at stack outlet, λ_a the air stoichiometry, $p_{a,fc,o}$ the dry air pressure at stack outlet, while ψ is defined as follows [3, p. 82]:

$$\psi = \frac{p_{H_2O,fc,i}}{p_{a,fc,i} - p_{H_2O,fc,i}} \quad (3.7)$$

with $p_{H_2O,fc,i}$ and $p_{a,fc,i}$ being the water vapor pressure and air pressure at stack inlet, respectively. However, not all produced water leaves the stack, as previously stated. According

to the water flow factor κ, only part of the produced water will leave with the exhaust air. This means that a more accurate representation of the water partial pressure reads:

$$p_{H_2O,fc,o} = \frac{(0.42 \cdot \kappa + \psi \cdot \lambda_a) \cdot p_{a,fc,o}}{0.42 \cdot \kappa - 0.21 + (1 + \psi) \cdot \lambda_a} \tag{3.8}$$

A more detailed derivation of Equation 3.8 is given in section B.2 of Appendix B.

To finally arrive at the relative humidity of the stack outlet air, one simply has to use the value found for $p_{H_2O,fc,o}$ as a function of κ and the value for $p_{H_2O,sat}$ corresponding to the stack air outlet temperature in equation 3.5. Given this relation, the value of κ could be calibrated to match the expected RH in the exhausts. This is shown in Table 3.2.

Table 3.2: Calibration of the Water Flow Factor κ

κ [-]	**50 kW**		**70 kW**		**97 kW**	
	$\dot{\mathbf{m}}_{\mathbf{H_2O,fc,o}}$ [g/s]	$\mathbf{RH_{fc,o}}$ [-]	$\dot{\mathbf{m}}_{\mathbf{H_2O,fc,o}}$ [g/s]	$\mathbf{RH_{fc,o}}$ [-]	$\dot{\mathbf{m}}_{\mathbf{H_2O,fc,o}}$ [g/s]	$\mathbf{RH_{fc,o}}$ [-]
0.6	6.31	0.8637	9.00	0.9132	12.57	1.010
0.7	6.94	0.9288	9.92	0.9845	13.90	1.0916
0.75	7.25	0.9603	10.38	1.0189	14.56	1.1277
0.8	7.56	0.9912	10.84	1.0527	15.21	1.1661

After some trial and error, the most suitable κ was deemed to be 0.66, which gave an RH of just above 90% for 50kW and just slightly over 100% for 97kW. Any other value for κ would result either to a too low RH at 50kW or a too high at 97kW. In order to perform these calculations, the stack outlet air temperature had to be known, which is where the stack thermal model comes in, as discussed in the next subsection.

3.4.3 Fuel Cell Heat Generation and Transfer

In steady state, when no conduction through materials such as casings is happening due to the system being warmed up to operating temperature, the thermal energy produced by the stack can go into three different heat sinks: the air, the water generated in the reaction, and of course the coolant.

Since this fuel cell stack operates well below 100°C, the air and the coolant remain in their normal state, i.e. gaseous and liquid respectively, throughout the whole process. Thus, the air and liquid take up only sensible heat from the stack. The water, however, can both take up sensible heat (in a gaseous or liquid state) as well as latent heat due to evaporation (evaporation happens continuously, at the surface between the water and air).

It is quite rare for product water to be fully in liquid form when leaving the stack via the air path, since most of the water present in the cathode side is usually evaporated into the exit air [3, p. 400]. Therefore, it is common practice to assume all the product water is evaporated, meaning that the LHV of the fuel is to be used for the calculation of sensible heat release as

a function of output power. For hydrogen, as discussed before, the LHV corresponds to 1.25 V. The cooling effect of the evaporation of water is thus already taken into account, and the sensible heat that is produced in the fuel cell stack can then be expressed as [3, p. 400]:

$$\dot{Q}_{fc} = P_{fc}\left(\frac{1.25}{V_{cell}} - 1\right) \tag{3.9}$$

This is thus the amount of thermal energy that needs to be taken away from the fuel cell by the air and coolant in order to stay on the right temperature level. With the aforementioned steady state assumptions (no conduction to casings etc.), the following heat balance could be made:

$$\dot{Q}_{fc} = \dot{Q}_c + \dot{Q}_a = \dot{m}_c \cdot c_{p,c} \cdot \Delta T_c + \dot{m}_a \cdot c_{p,a} \cdot \Delta T_a \tag{3.10}$$

where $\Delta T_c = T_{c,o} - T_{c,i}$ and $\Delta T_a = T_{a,o} - T_{a,i}$ are the temperature differences from inlet to outlet of the coolant and air respectively. A thermal model could be made in order to calculate the air and coolant outlet temperatures (assuming the inlet temperatures are known) by means of heat transfer theory. In order to quantify the heat transfers from the stack cells to the air and to the coolant, one could set up the following heat balances:

$$\dot{Q}_c = (UA)_c \cdot \Delta T_{fc,c} = \dot{m}_c \cdot c_{p,c} \cdot \Delta T_c \tag{3.11}$$

$$\dot{Q}_a = (UA)_a \cdot \Delta T_{fc,a} = \dot{m}_a \cdot c_{p,a} \cdot \Delta T_a \tag{3.12}$$

where $(UA)_c$ and $(UA)_a$ are the overall heat transfer coefficients (multiplied with the heat transfer area) for the coolant and air respectively. $\Delta T_{fc,c}$ is the average temperature difference between the stack cells and the coolant, and $\Delta T_{fc,a}$ the average temperature difference between the stack cells and the air. The issue with this approach was that the heat transfer coefficients and the temperature of the fuel cells are unknown and very difficult to measure. There was no existing data on these parameters for the considered system, and therefore this calculation method was deemed unfeasible.

What was important from the perspective of the full model, was that the stack model provided an accurate estimate on the stack air exit temperature. This could be done by making a common yet valid assumption: the stack air outlet temperature was said to be equal to the stack coolant outlet temperature [4, p. 123].

Since measurement data exisited on the inlet and outlet coolant temperatures in function of the operating conditions, it was possible to quantify the air outlet temperature. This assumption has been made in literature before. There are two arguments that solidify its use, one of them general and the other specific to this research.

Firstly, the heat capacity rate ($\dot{m} \cdot c_p$) of the coolant is many times greater than that of the air. Their ratio can be in the order of 50-100: assume a stack coolant massflow of 2.6kg/s (corresponding to about 150l/min) and an air massflow of 0.09kg/s (for around 100kW stack power). The heat capacity of the coolant is about 3500J/kg/K and for air it is 1005J/kg/K. This leads to a ratio of heat capacity rates of $2.6 \cdot 3500/(0.09 \cdot 1005) = 100$, meaning for the

same temperature difference, the coolant will absorb about 100 times more heat than the air. In a location where the air in the stack would be hotter than the coolant, heat will flow quickly from the air to the coolant by conduction through the bipolar plates, reaching an equilibrium temperature that is practically the same as the coolant's temperature.

Secondly, in the baseline fuel cell stack configuration, the air and coolant are in co-flow. This means the air and coolant flow close to eachother in the same direction through the stack. Combining this fact with the first fact mentioned above, one can argue that the air outlet temperature would be very close to the coolant outlet temperature in this specific case. Therefore the assumption is deemed to be valid.

How the stack air outlet temperature was then eventually modeled was as follows: In the real system, the thermal management makes sure that the stack coolant inlet temperature is 60°C. Using measurement data, a mapping of the coolant temperature rise was made in function of the generated stack power, which was taken as the independent variable for the map. This is since the stack power is the direct indicator of stack heat release and thus coolant temperature increase. So depending on the stack power, the model calculates the coolant outlet temperature, and thus the air outlet temperature of the stack is known. The simple equation is shown below:

$$T_{a,o} = T_{c,o} = 60 + \Delta T_c(P_{fc}) \tag{3.13}$$

where $T_{a,o}$ and $T_{c,o}$ are the stack outlet air and coolant temperatures respectively, and $\Delta T_c(P_{fc})$ is the mapped stack coolant temperature difference in function of stack power. This concludes the thermal modeling of the fuel cell stack. The next subsection focuses on how to compute P_{fc}.

3.4.4 Fuel Cell Power Generation

The electrical power generated by a fuel cell stack is, like any electrical power generator, the product of the voltage generated by the stack and the current pulled from it:

$$P_{fc} = I_{fc} \cdot V_{fc} \tag{3.14}$$

where the stack current can be obtained when one knows the air massflow and used air stoichiometry [3, p. 397]:

$$I_{fc} = \frac{0.21 \cdot 4 \cdot F \cdot \dot{m}_{a,fc,i}}{M_{O_2} \cdot n_{cell} \cdot \lambda_a} \tag{3.15}$$

Additionally, when the stack current is known as well as assuming no fuel crossover, the hydrogen consumption can be computed through [3, p. 398]:

$$\dot{m}_{H_2} = \frac{M_{H_2} \cdot I_{fc} \cdot n_{cell}}{2 \cdot F} \tag{3.16}$$

The stack voltage is equal to the voltage of a single cell multiplied by the amount of fuel cells in series:

$$V_{fc} = V_{cell} \cdot n_{cell} \tag{3.17}$$

As explained in Section 2.1.5, the polarization curve of a fuel cell can be formulated as follows:

$$V_{cell}(T, p, i) = E_0 + a \cdot T \cdot \ln(p) - r \cdot i - b \cdot \ln(i) - c \cdot \exp(d \cdot i) \tag{3.18}$$

where $E = E_0 + b \cdot T \cdot \ln(p)$ represents the reversible OCV that depends on the operating pressure and temperature of the fuel cell, with E_0 being the OCV at standard temperature and pressure. The remaining three terms represent the ohmic losses, activation losses and concentration losses, respectively.

What needed to be done to use the polarization curve in a model, was to quantify the various coefficients in Equation 3.18. This was done using testing data. For the baseline simulation, the data from the nominal measurement was taking to fit the following polarization curve:

$$V_{cell}(i) = E_{oc} - r \cdot i - a \cdot \ln(i) \tag{3.19}$$

This is different from the previous formulations of the polarization curve that have been shown, starting with E_{oc}, which is not the same as $E_0 = 1.23$V. Recalling the internal currents, the voltage at zero effective current (which in Equation 3.19 equals E_{oc}) is already lower than the theoretical OCV, hence $E_{oc} < E_0$. Secondly, there is no prescribed dependency on pressure, since the operating pressure varies between the 10kW and 100kW operation point due to the logic of the vehicles control unit, and the data inherently carries this pressure dependent information. Finally, no concentration losses were considered since from the data it was clear that up to the 100 kW point, the polarization curve was still in the ohmic region where it decreases linearly, and the exponential decrease was not yet present. Therefore, using the data, the best fit was made by finding the optimal positive values for E_{oc}, r and a.

For the turbocharged simulations, it was expected that the operating pressure at same air massflow would be higher, meaning the dependency of the voltage on pressure now had to be incorporated. For that, a polarization curve of the following form was fitted to the data:

$$V_{cell}(i) = E_{oc} - r \cdot i - (a - b) \cdot \ln(i) + c \cdot \ln(p) \tag{3.20}$$

This was possible since the data contained polcurves measured at different stack air pressures. As can be seen, two additions have been made compared to Equation 3.19. This is since increasing the operating pressure has two benefits for the voltage as explained in Section 2.2.1. One benefit is decreasing the activation losses, hence the introduction of positive parameter b. The other is increasing the OCV, hence the addition of the term $c \cdot \ln(p)$. Again using the data, positive values for E_{oc}, r, $(a-b)$ and c were fitted to obtain the voltage model.

The last part of the stack model that needed to be built in was the pressure drop, which is discussed now.

3.4.5 Stack Air Pressure Drop

Physically, the pressure drop of a gas over a component depends on the square of the flow speed of the gas, as per the momentum equation [49, p. 144]:

$$dp = -\rho \cdot V \cdot dV \tag{3.21}$$

Since flow speed can be related to air massflow through conservation of mass ($\dot{m} = \rho AV$), it can also be said that pressure drop is proportional to massflow. By substitution and simplification, one can come to the following equation:

$$\Delta p = \xi \cdot \frac{\dot{m}^2}{\rho_i} \tag{3.22}$$

where ξ is a constant depending on the component geometry, and ρ_i is the inlet air density for the component. The inlet air density of any component varies with its inlet pressure and temperature.

In a fuel cell system, depending on its power output, the air has a certain temperature and pressure at each component in the air path: the air temperatures and pressures are usually higher at higher stack powers (and therefore also the air density). So, at higher air massflows (i.e. higher stack powers), the air density also increases. In the vehicle measurement data then, the change in massflow automatically carried the information on the change in air density, and it was decided to compute the pressure drop only in function of the air massflow:

$$\Delta p = \xi \cdot \dot{m}^2 \tag{3.23}$$

where ξ was estimated from the measurement data. This solved the issue of not having measurement data of same air massflow at varying pressures (the vehicle control could not be manipulated to run user-specified conditions).

This approach of modeling the pressure drop is the same for all other components in the complete system model, except for the intercooler and the E-(turbo)compressor (which will be discussed in Sections 3.5 and 3.7 respectively).

3.4.6 Overview of the Complete Fuel Cell Stack Model

The fuel cell stack model can be summarized by the following schematic showing its inputs and outputs:

Figure 3.5: Schematic of the Inputs and Outputs of the Fuel Cell Stack Model

3.5 Intercooler Modeling

The goal of the intercooler model was to both predict the behaviour of the intercooler in baseline system operational conditions, and also at the higher air pressures and temperatures that occur when using an e-turbo instead of e-compressor (due to the higher compression ratio). Purely using mappings based on measurement data from the real baseline system would not have been sufficient, as they could not accurately predict intercooler behavior in the turbocharged system. The desired functionalities of the intercooler model are as follows:

- predict the change in air and coolant temperature (heat transfer)
- predict the change in air pressure (pressure losses)

In AVL Cruise M, one can choose certain options that allow for calculating an outlet temperature and inlet pressure of a component by means of a user-specified model. The known inputs

then have to be an inlet temperature and outlet pressure, which is the case in this model (recall the pressure calculation chain from Section 3.3.3). The relative humiditiy change over the component will then be computed automatically by AVL Cruise M, so there was no need to explicitly model this. Only for the fuel cell stack (as discussed before) and the humidifier (as discussed later), custom humidity models were specified.

Each functionality is again broken down in the following subsubsections, starting with the heat transfer.

3.5.1 Intercooler Heat Transfer

To set up the heat transfer model, the ϵ-NTU method (Number of Transfer Units) was used. It allows for finding the outlet temperatures of the hot and cold sides of a heat exchanger. The theory presented below was taken from chapter 3 of [50].

The dimensionless parameter ϵ is called the heat exchanger effectiveness, and is defined as the ratio between the actual heat transfer taking place and the maximal theoretical heat transfer possible. The latter is defined as the heat transfer obtained in a counterflow heat exchanger with infinite surface area. In that case, the heat transfer is equal to:

$$\dot{Q}_{max} = (\dot{m} \cdot c_p)_{min} \cdot (\Delta T)_{max} = (\dot{m} \cdot c_p)_a \cdot (T_{a,i} - T_{c,i}) \tag{3.24}$$

where $T_{a,i}$ and $T_{c,i}$ are the intercooler air and coolant inlet temperatures, respectively. Here $(\dot{m} \cdot c_p)_{min} = (\dot{m} \cdot c_p)_a$ since the air is the thermally weaker fluid, and the maximum temperature difference is the one between the hot inlet air and the cold inlet coolant. The effectiveness is then simply:

$$\epsilon = \frac{\dot{Q}}{\dot{Q}_{max}} = \frac{\dot{m}_a \cdot c_{p,a} \cdot \Delta T_a}{\dot{m}_a \cdot c_{p,a} \cdot (T_{c,i} - T_{a,i})} = \frac{\Delta T_a}{(T_{c,i} - T_{a,i})} \tag{3.25}$$

In other words, since the inlet temperatures and massflows of both the air and coolant are model inputs, if one knows ϵ, one can compute the air temperature change and subsequently the coolant temperature change (by means of conservation of energy).

To compute ϵ, the NTU first has to be found. NTU is also a dimensionless parameter that represents the 'thermal size' of the heat exchanger and is defined as:

$$NTU = \frac{UA}{C_{min}} \tag{3.26}$$

Where C_{min} is the minimum of $(\dot{m}_a \cdot c_{p,a}, \dot{m}_c \cdot c_{p,c})$, i.e. the weakest flow heat capacity rate (here air), and UA is the product of the overall heat transfer coefficient and equivalent surface area. C_{min} is known from the input of the simulation, yet UA has to be determined both by geometrical features of the heat exchanger as well as vehicle measurements. A detailed description of how that has been done is explained in Section B.3. The result is that during the simulation, depending on the corresponding inputs, UA could be computed.

The next step then was to obtain the NTU using Equation 3.26. The core part of the ϵ-NTU method is the mathematical equation that links both dimensionless variables. When the NTU is known, ϵ can be computed if the correct expression is used, which is dependent on the intercooler geometry. The relationship for a cross-flow heat exchanger with both hot and cold streams unmixed is as follows:

$$\epsilon = 1 - \exp(-NTU) - \exp\left[-(1 + C^*)NTU\right] \cdot \sum_{n=1}^{\infty} {C^*}^n P_n(NTU) \tag{3.27}$$

$$P_n(NTU) = \frac{1}{(n+1)!} \cdot \sum_{i=1}^{n} \frac{n+1-i}{i!} NTU^{n+i} \tag{3.28}$$

$$C^* = \frac{C_{min}}{C_{max}} = \frac{\dot{m}_a \cdot c_{p,a}}{\dot{m}_c \cdot c_{p,c}} \tag{3.29}$$

The value for ϵ is then obtained using the above equations with $n = 10$. Knowing ϵ, finally the air temperature change over the intercooler could be computed using Equation 3.25, which is the main desired output of the intercooler thermal model. The air outlet temperature is then simply the air inlet temperature summed with the obtained air temperature difference. The coolant temperature difference could be then estimated by means of enforcing a heat balance between the air and the coolant:

$$\Delta T_c = \frac{\dot{Q}_c}{\dot{m}_c \cdot C_{p,c}} = \frac{\dot{Q}_a}{\dot{m}_c c_{p,c}} = C^* \cdot \Delta T_{air} \tag{3.30}$$

This concludes how the thermal model for the intercooler is setup.

3.5.2 Intercooler Pressure Drop

Unlike most other components in the system, the pressure drop model for the intercooler is made to be theory-based instead of a data mapping in function of air massflow. The main reason for this is stated above: the model has to predict intercooler behavior outside of nominal operational conditions represented by the available measurement data. However, there is a second more practical reason: the pressure drop over the real intercooler is too small to be captured within the accuracy of the installed pressure sensors on the test vehicle, as the measured pressures seemed to actually increase over the intercooler instead of drop which is physically not possible and made this data useless. The theoretical pressure drop calculation method was taken from [50] (chapter 8) and explained in detail in Section B.4 of Appendix B.

3.5.3 Overview of the Complete Intercooler Model

In figure 3.6, the complete intercooler model with corresponding inputs and outputs is visualized.

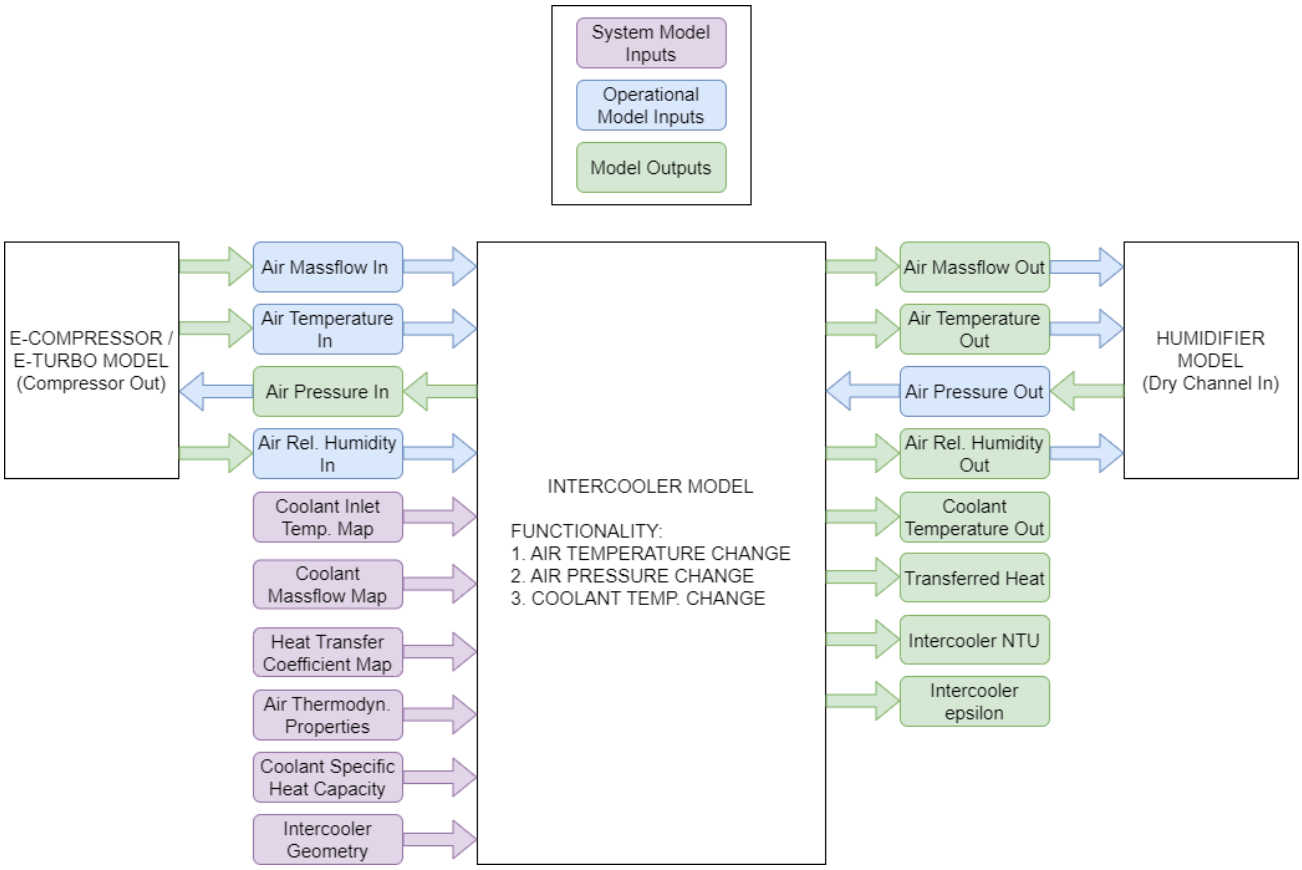

Figure 3.6: Schematic of the Inputs and Outputs of the Intercooler Model

3.6 Humidifier Modeling

The humidifier has a big influence on the performance of the whole system, as it handles both the incoming and the exhaust air, and lets the two flows interact. The desired functionalities of the humidifier model are as follows:

- predict the change in water content in the air (water massflow and relative humidity)
- predict the change in air temperature (heat transfer)
- predict the change in air pressure (pressure losses)

AVL Cruise M has a built-in humidifier function block. It requires certain user-defined input parameters such as the type of humidifier (plate / shell-tube) and some geometrical features. The considered humidifier is of the shell-tube type. A sketch of such a humidifier is shown below:

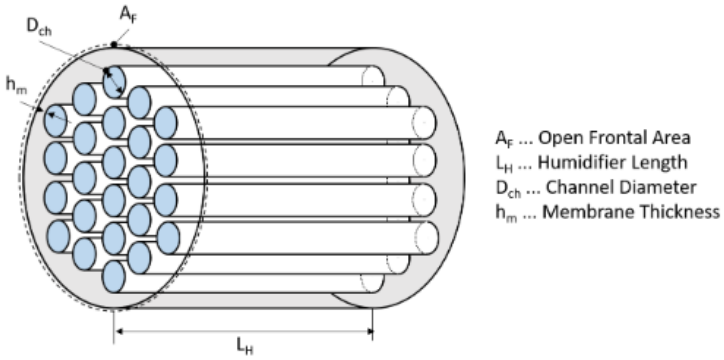

Figure 3.7: Schematic of a Shell-Tube Type Humidifier (from AVL Cruise M documentation)

The dry air flows inside the circular tubes which are made from a polymer membrane similar to the PEM in the fuel cell stack [3, p. 89]. This membrane can exchange water vapor from a wet gas stream to a dry gas stream. The wet air flows around the circular tubes, in this case in counterflow with the dry air flow. The pathways for the dry and wet air flow are referred to as the dry and wet channel, respectively. Each of the two channels logically also features an inlet and outlet. The dry inlet equals the intercooler outlet, the dry outlet equals the stack inlet, the wet inlet equals the stack outlet and the wet outlet equals the pressure valve inlet.

The AVL humidifier block requires as input the massflows going through both the dry and wet channels (usually not the same due to stack oxygen consumption), as well as the pressures, temperatures and relative humidities of the air coming in at both channels. Additionally, some system-dependent parameters such as certain dimensions (some of them are indicated in Figure 3.7) have to be specified. At that point, the AVL Cruise M humidifier block is ready to be used.

The theoretical model behind it originates from [51]. In order to tailor the behaviour of this model to match the specific hardware for this simulation, there are three multipliers that can be used: a volume scaling that influences mainly the model stability but also the change in relative humidity in both channels, a heat transfer factor that influences the heat transferred from the hotter to the colder stream (usually wet to dry), and lastly a diffusion multiplier that influences the amount of water vapor being transferred from the wet to the dry channel. If one has access to sufficient system data regarding pressure drops, temperature changes and relative humidity changes in function of operating conditions, these three multipliers can be tuned to calibrate the model.

Unfortunately, using this model seemed to be no option in the case of this research. First of all, there were no relative humidity measurements available for any point in the system, making it hard to tune the diffusion multiplier, which also had an influence on the heat transfer in the humidifier. This in turn led to numerical instabilities that made the simulations crash, which could not be fixed by changing the other multipliers. For this reason, it was decided to develop an own humidifier model, although simplified. The setup and working of this model is discussed in the following subsubsections.

3.6.1 Humidifier Heat Transfers

The way the heat exchange is modeled for the humidifier is similar to the intercooler: the ϵ-NTU method is applied again. In this case, heat transfer occurs between the intake (dry) and exhaust (wet) streams going through the humidifier. Therefore, this component could be modeled as an air-to-air heat exchanger, and this specific humidifier featured a counterflow configuration.

When checking the available measurement data, it seemed like the measured heat gain at the dry side mostly did not equal the measured heat loss at the wet side. Namely, the ratio of dry channel heat gain and wet channel heat loss fluctuated between 0.6 and 1.6, meaning sometimes the dry side got more heat input than the wet side gave, and vice versa. This is since the measurements were not taken in a perfectly steady state, and thus a heat balance between the dry and wet channel could not be implied on this data. This had the consequence that there was no overall UA that could be extracted from the measurements: eventhough a log-mean temperature difference (LMTD, see equation B.36) between the dry and wet side could be calculated, the heat change in both channels was not equal.

To then obtain a model that could accurately predict both the dry and wet outlet temperatures, it was considered to define a UA for the two streams separately, meaning each side had a specific NTU and ϵ value. They were denoted as NTU_d and NTU_w, the NTUs of the dry and wet side respecitively, and ϵ_d and ϵ_w, the effectiveness values of the dry and wet side respectively. Just as with the intercooler model, first the NTUs have to be calculated in order to compute ϵ. Once the latter is known, the temperature difference (and thus the outlet temperature) could be obtained.

The NTU_d and NTU_w were calculated in the same way mentioned before in the intercooler model section:

$$NTU_d = \frac{(UA)_d}{C_d} \tag{3.31}$$

$$NTU_w = \frac{(UA)_w}{C_w} \tag{3.32}$$

where C_d and C_w are the heat capacity rates ($\dot{m} \cdot c_p$) of the dry and wet flows respectively. In order to obtain these NTU values, $(UA)_d$ and $(UA)_w$ had to be computed from the measurement data, which was done as follows:

$$(UA)_d = \frac{Q_d}{LMTD} = \frac{\dot{m}_d c_{p,d} \Delta T_d}{LMTD} \tag{3.33}$$

$$(UA)_w = \frac{Q_w}{LMTD} = \frac{\dot{m}_w c_{p,w} \Delta T_w}{LMTD} \tag{3.34}$$

where $\dot{m}_d$ is the measured dry massflow, $c_{p,d} = 1005$J/kg/K is the dry air specific heat capacity, $\dot{m}_w$ the wet air massflow computed by the stack model, and $c_{p,w} = 1280$J/kg/K,

which was the average moist air specific heat capacity at stack outlet conditions. The latter is computed by the following relation taken from [52]:

$$c_{p,w} = c_{p,d} + \omega \cdot c_{p,wv} = 1005 + \omega \cdot 1884 \tag{3.35}$$

where ω is the humidity ratio (around 0.146 at stack outlet) and $c_{p,wv} = 1884$J/kg/K the specific heat capacity of water vapor. In the model, measurement data was used to estimate the $(UA)_d$ and $(UA)_w$ values in function of air massflow. The working of this model was then similar to the intercooler heat exchange model: once the UA's were known, the NTU's could be computed using Equations 3.31 and 3.32, such that the effectiveness could be calculated. For a counterflow heat exchanger, the relationship between NTU and effectiveness is defined as [50, p. 124]:

$$\epsilon = \frac{1 - \exp(-NTU(1 - C^*))}{1 - C^* \exp(-NTU(1 - C^*))} \tag{3.36}$$

with C^* still defined as C_{min}/C_{max}. Finally, knowing the values for both ϵ's, the outlet temperatures of the dry and wet channels could be calculated:

$$T_{o,d} = T_{i,d} + \epsilon_d \frac{C_{min}}{C_d}(T_{i,w} - T_{i,d}) \tag{3.37}$$

$$T_{o,w} = T_{i,w} - \epsilon_w \frac{C_{min}}{C_w}(T_{i,w} - T_{i,d}) \tag{3.38}$$

This completed the heat transfer functionality.

3.6.2 Air Humidification

As already mentioned in Subsection 3.4.2, the humidifier was assumed to be an ideal one. What is meant by that term in this research is that it is assumed that all the water vapor present in the stack outlet air (the wet stream), could if needed be transferred to the dry side by this humidifier. So even in a hypothetical limiting case where for certain operational conditions all the water from the wet stream is needed to sufficiently humidify the dry stream, this model would allow that to happen and the humidifier wet outlet stream would have zero relative humidity (no water content), which is obviously not the case in reality. However, this assumption allowed to set up a simple model for calulating the outlet relative humidities of the dry and wet humidifier channels.

The target relative humidity of the stack inlet air was set to 85% for all simulations. Using measurement data and the already developed stack model that could compute the stack air oulet relative humidity and water massflow, it was checked whether there was enough water available to always humidify the dry air stream to this target 85%. A reminder should be given about the water flow factor κ, which was calibrated to achieve good outlet relative humidities and had an impact on the quantification of how much water came out of the stack with the air. Considering this, the results showed that for the full measurement range from

10kW to 100kW stack power, there seemed to be enough water in the stack outlet air to humidify the stack inlet air to 85%, assuming an ideal humidifier.

The water balancing loop in the perspective of the air path between the humidifier and the fuel cell stack is visualized in the schematic below:

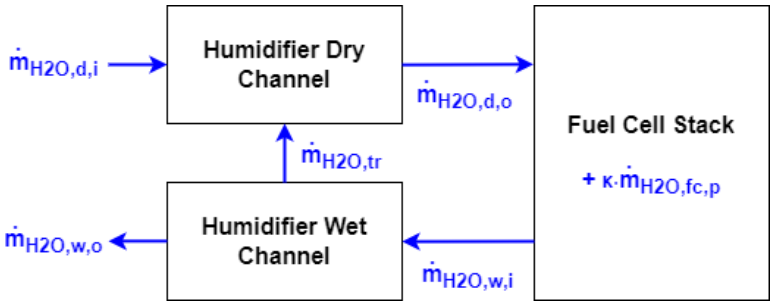

Figure 3.8: The Water Balancing Loop of the Humidifier and Stack Interaction

where $\dot{m}_{H_2O,d,i}$ is the water massflow going into the humidifier dry channel, $\dot{m}_{H_2O,d,o} = \dot{m}_{H_2O,fc,i}$ is the water massflow coming out of the dry channel/going into the stack, $\dot{m}_{H_2O,fc,p}$ is the stack water production rate, $\dot{m}_{H_2O,w,i} = \dot{m}_{H_2O,fc,o}$ the water massflow going in the wet channel/coming out of the stack, $\dot{m}_{H_2O,w,o}$ the water massflow going out of the wet channel, and finally $\dot{m}_{H_2O,tr}$ the water transfer rate from wet to dry.

The following water balances must hold in this humidification model:

$$\dot{m}_{H_2O,d,o} = \dot{m}_{H_2O,d,i} + \dot{m}_{H_2O,tr} \tag{3.39}$$

$$\dot{m}_{H_2O,w,i} = \dot{m}_{H_2O,d,o} + \kappa \cdot \dot{m}_{H_2O,fc,p} \tag{3.40}$$

$$\dot{m}_{H_2O,w,o} = \dot{m}_{H_2O,w,i} - \dot{m}_{H_2O,tr} \tag{3.41}$$

The way these different water massflows are calculated is as follows. Given that the intercooler outlet conditions (i.e. humidifier dry inlet conditions) are already known, the dry inlet relative humidity and temperature are used to obtain the corresponding water partial pressure:

$$p_{H_2O,d,i} = RH_{d,i} \cdot p_{H_2O,sat}(T_{a,d,i}) \tag{3.42}$$

Using this partial pressure, the following equation is used to compute the water massflow going into the dry channel [3, p. 80]:

$$\dot{m}_{H_2O,d,i} = 0.622 \cdot \frac{p_{H_2O,d,i}}{p_{a,d,i} - p_{H_2O,d,i}} \cdot \dot{m}_{a,d,i} \tag{3.43}$$

where $p_{a,d,i}$ and $\dot{m}_{a,d,i}$ are the air pressure and dry air massflow at dry channel inlet. Meanwhile, from the fuel cell stack model, the outlet conditions (i.e. humidifier wet inlet conditions) were known, meaning also the water massflow entering the wet channel could be computed:

$$p_{H_2O,w,i} = RH_{w,i} \cdot p_{H_2O,sat}(T_{a,w,i}) \tag{3.44}$$

$$\dot{m}_{H_2O,w,i} = 0.622 \cdot \frac{p_{H_2O,w,i}}{p_{a,w,i} - p_{H_2O,w,i}} \cdot \dot{m}_{a,w,i} \tag{3.45}$$

where $p_{H_2O,w,i}$ and $p_{a,w,i}$ are the wet inlet water partial pressure and air pressure respectively, and $\dot{m}_{a,w,i}$ the dry air massflow at wet channel inlet. As aforementioned, the target relative humidity of the stack inlet air was set to 85% and was therefore also a model input. In order to know the required stack inlet water massflow, the stack inlet air temperature has to be known. This was provided by the humidifier thermal model explained above. Then the calculation is simply:

$$p_{H_2O,d,o} = 0.85 \cdot p_{H_2O,sat}(T_{a,d,o}) \tag{3.46}$$

$$\dot{m}_{H_2O,d,o} = 0.622 \cdot \frac{p_{H_2O,d,o}}{p_{a,d,o} - p_{H_2O,d,o}} \cdot \dot{m}_{a,d,o} \tag{3.47}$$

where $p_{H_2O,d,o}$ and $p_{d,o}$ are the dry outlet water partial pressure and air pressure respectively, and $\dot{m}_{a,d,o}$ the dry air massflow at dry channel outlet. At this point, the necessary water transfer from the wet to the dry channel $\dot{w}_{tr} = \dot{m}_{H_2O,d,o} - \dot{m}_{H_2O,d,i}$ could be computed. What had to be checked here was that $\dot{m}_{H_2O,tr}$ should always be less than $\dot{m}_{H_2O,w,i}$, otherwise there was not enough water in the system to humidify to 85% with an ideal humidifier.

The water massflow going out of the wet channel is then simply calculated using Equation 3.41. Since the wet channel air outlet temperature and pressure were provided by the humidifier thermal and pressure drop models respectively, the wet channel outlet air relative humidity could be calculated simply through the definition of RH using the water vapor partial pressure of the wet outlet $p_{w,w,o}$, computed in Equation 3.48.

$$p_{H_2O,w,o} = \frac{p_{H_2O,w,o}}{1 + 0.622 \cdot \dot{m}_{a,w,o}/\dot{m}_{H_2O,w,o}} \tag{3.48}$$

3.6.3 Humidifier Pressure Drops

The pressure drops are implemented analogously to the fuel cell stack pressure drop, as explained in Subsection 3.4.5.

3.6.4 Overview of the Complete Humidifier Model

The way the humidifier model is connected in the full system model with its inputs and outputs is visualized in figure 3.9.

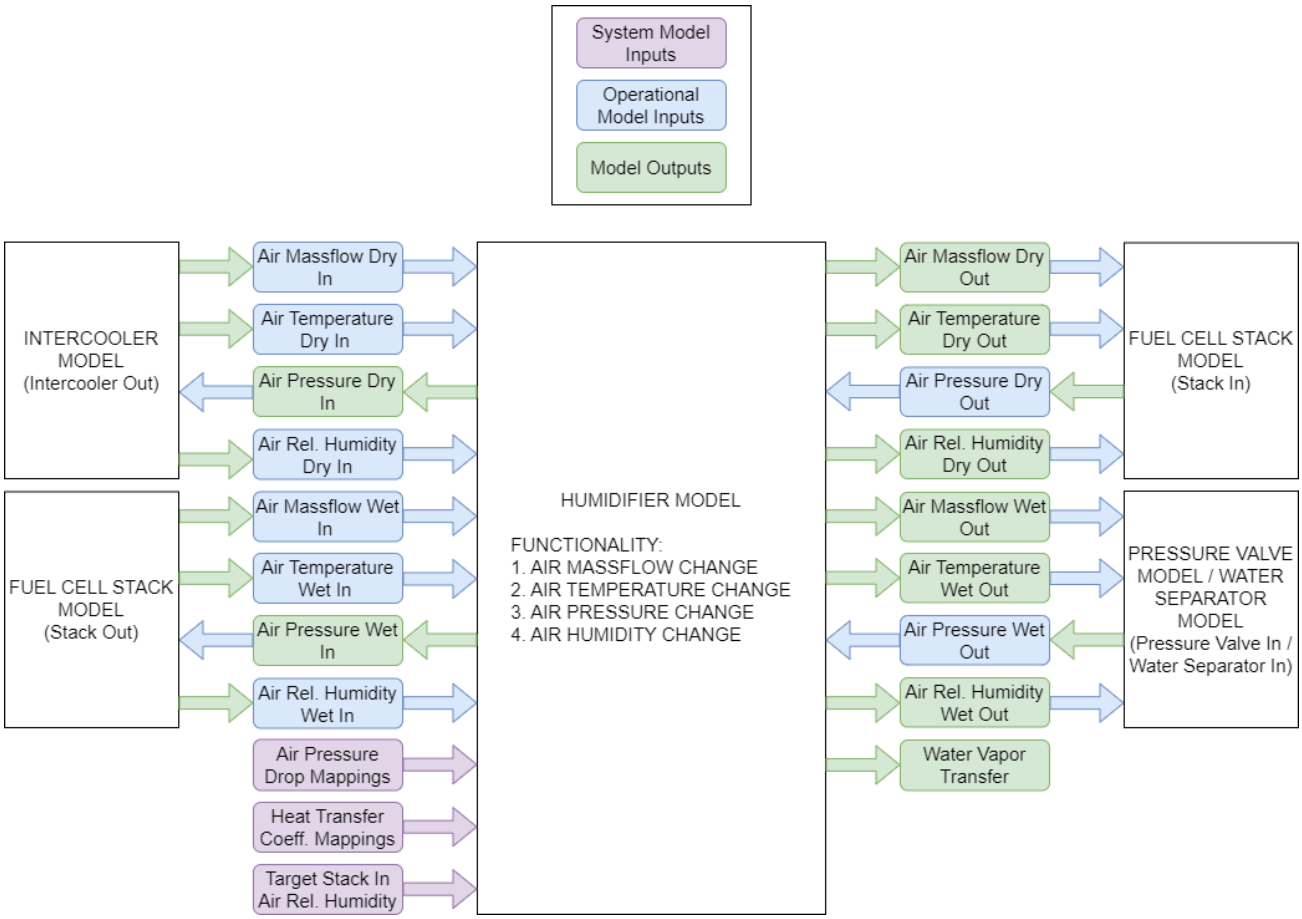

Figure 3.9: Schematic of the Inputs and Outputs of the Humidifier Model

3.7 E-Compressor & E-Turbo Modeling

The E-compressor is the component in the system that generates the massflow to power the stack, and therefore it is a power consumer. For the overall goal of the system model, which was to clearly answer the stated research questions, it was important that the necessary inverter input power (power going from the stack to the air compression) was estimated accurately. The desired functionalities of the E-compressor model are as follows:

- predict the change in air massflow (massflow generation)
- predict the change in air temperature (compression and heat transfer)
- predict the conversion of electrical energy into kinetic energy (inverter power to compression power)

3.7.1 Air Massflow Control

The amount of air massflow that a radial compressor generates depends on a few different factors. Assuming the input power is taken care of and the size of the compressor wheel is already fixed, the air massflow generated is influenced by the rotational speed n of the compressor wheel and the degree of flow restriction in the system behind the compressor, which is straightforwardly indicated by the pressure ratio Π_c with which the compressor operates. These dependencies are clearly visible in the compressor map, which was already shown in Figure 3.1.

So, depending on the necessary pressure ratio (due to occurring backpressure) and the desired air massflow, the compressor map can be used to find the corresponding compressor speed (indicated by the dashed lines in figure 3.1). In the real fuel cell system then, the control unit will set the speed of the E-motor that powers the compressor wheel to the target value according to the compressor map.

However, a compressor map can be used in multiple ways. As long as two of the three variables (massflow, pressure ratio or speed) are known, the third can be predicted by means of simple 2D interpolation in the map. This method is used in the compressor model, and the detailed implementation is described. The main procedure is visualized in Figure 3.10.

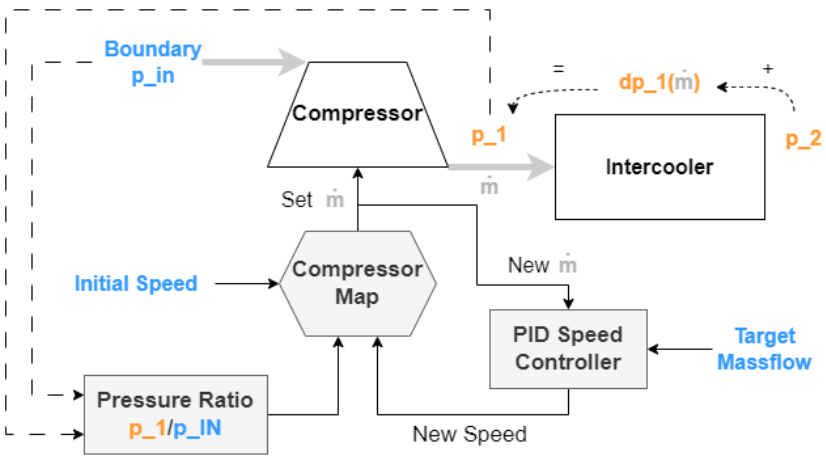

Figure 3.10: Schematic Showing the Massflow Calculation Algorithm. Simulation and Boundary Inputs in Blue, Massflow in Grey and Varying Pressures in Orange

In the simulation, the target air massflow is the main system model input, as this dictates how much power the stack would provide as well as how much power the compressor inverter would need. At the start of the simulation (t=0), the compressor inlet and outlet pressure are given by a boundary and initial condition respectively, meaning that there is also an initial pressure ratio (a little larger than 1).

Additionally, an initial condition on the compressor speed is set. This way, the initial massflow could be found by utilizing the compressor map. The resulting massflow is then passed to a

PID-controller that updates the compressor speed to eventually obtain the target massflow given as the main model input. After a certain amount of simulation time (iterations), the target massflow is obtained and all other parameters also reach steady-state.

3.7.2 Compressor Air Temperature Increase

The conventional way to model the temperature increase in a compressor is to assume it is only the result of compression (due to work input), and neglecting any heat tranfser. For compressors in ICE turbochargers, this assumption is fine for this kind of model [53, p. 7]. However, in the case of an E-(turbo)compressor, due to the liquid cooling of the E-motor that sits right next to the compressor, or in between compressor and turbine, there is significant heat transfer taking place that cannot be neglected. This posed a new challenge, which is presented below.

If the heat transfer could be neglected, the ideal reference flow is isentropic flow, as it is reversible and adiabatic. In that case, a compressor efficiency could be represented by an isentropic efficiency that is defined as follows [53, p. 21]:

$$\eta_c = \frac{T_{tot,2s} - T_{tot,1}}{T_{tot,2} - T_{tot,1}} = \frac{T_{tot,1}\left(\Pi_{tot,c}^{(\gamma-1)/\gamma} - 1\right)}{T_{tot,1} - T_{tot,1}} \tag{3.49}$$

where T_{tot1} and T_{tot1} are the actual inlet and outlet stagnation (or total) temperatures, and $T_{tot,2s}$ is the ideal outlet stagnation temperature if the compressor would have no losses. $\Pi_{tot,c}$ is the compressor stagnation pressure ratio, and γ is the ratio of specific heats of air.

The difference and relationship between stagnation and static conditions is elaborated upon in Section B.5 of Appendix B. There it is shown that for this research, stagnation and static conditions could be assumed to be the same, as the flow speed is sufficiently low. In practice, during the modeling, it was therefore assumed that $T_{tot} = T$ and $p_{tot} = p$.

By measuring the temperature and pressure at compressor inlet and outlet on a testbench, a compressor efficiency map can be made in function of parameters such as massflow, pressure ratio and speed. In a compressor model, if the compressor inlet temperature was given and the pressure ratio was known, the corresponding efficiency could be obtained from the map, and Equation 3.49 can be rewritten to:

$$T_2 = T_1 \left[1 + \frac{\Pi_c^{(\gamma-1)/\gamma} - 1}{\eta_c}\right] \tag{3.50}$$

such that the outlet temperature could be computed. However, recall that this was the conventional way of computing the outlet temperature assuming there was no heat transfer occurring in the compressor. Unfortunately, this is not the case in this research. The following T-s diagram (Figure 3.11) clearly visualizes the associated problem.

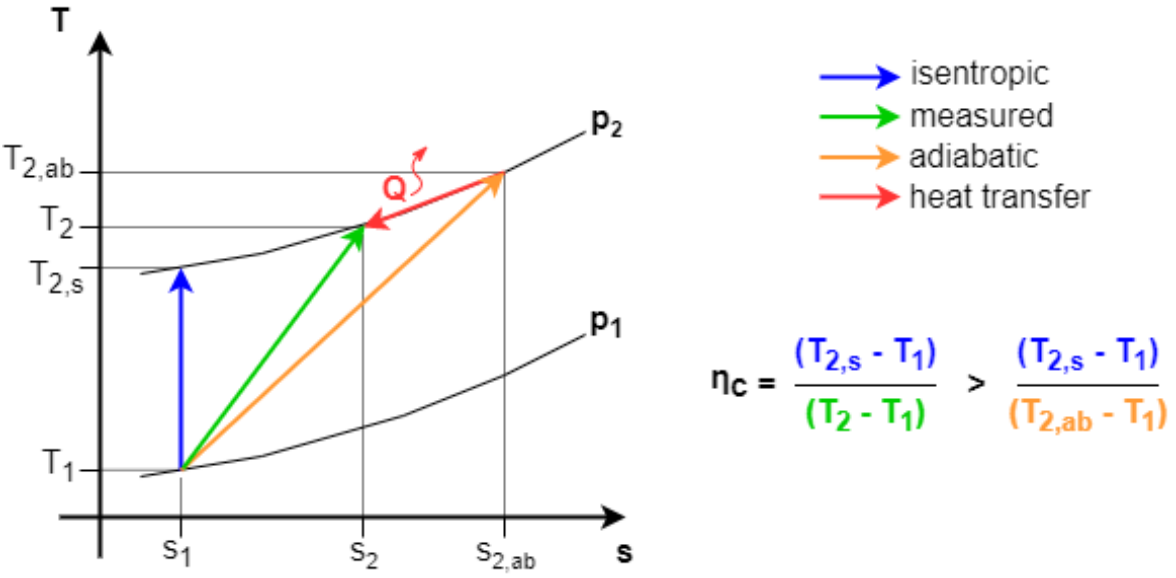

Figure 3.11: Temperature-entropy Diagram of an E-compressor. Blue: Isentropic Compression, Orange: Adiabatic Compression (with Subscript 'ab'), Red: Heat Transfer from Air to Coolant, Green: Measured Compression on a Testbench

In Figure 3.11, a comparison is made between adiabatic and non-adiabatic compression taking place in the same compressor. Assume in both cases, the compressor operates with the same inlet temperature and at the same pressure ratio, massflow and speed. Since the non-adiabatic compression experiences heat transfer (from the air to the coolant, red arrow), the outlet temperature will be lower (T_2, green arrow) compared to the adiabatic compression process ($T_{2,ab}$, orange arrow). The assumption that pressure p_2 does not change during the heat transfer is argumented in Section B.6.

The ideal temperature difference ($T_{2s} - T_1$) represented by the blue arrow is the same for both cases since the pressure ratio is equal, but because the actual temperature difference is now lower for the non-adiabatic compression, the simple consequence is that the computed isentropic efficiency (green arrow) is higher than for the adiabatic case (orange arrow). In cases of low air flows, it was even seen in the measurements that the efficiency was above 100%: this happens when the heat transfer is so significant that the red arrow becomes very long and 'pushes' the green arrow to the left of the blue arrow.

However, it is the same compressor, therefore its efficiency should be remain constant for the same operating point irrespective of absence or presence of heat transfer. This shows the problem with using an isentropic efficiency in this case: the values resulting from this definition of efficiency overestimate the performance of the compressor since they are too high.

To accurately model the compressor outlet temperature then, another approach had to be found. This is discussed in the coming part.

The First Attempt

The first attempt consists of setting up an energy balance in order to correct the overestimated isentropic compressor efficiency to a lower value with the available measurement data. This attempt was not successful, but for reference, the approach is documented in Section B.7.

The conclusion of this first attempt is that an accurate energy balance could not be formulated in terms of a closed mathematical problem featuring the same amount of equations and unknowns. The reason for this is that the available measurement data did not contain a sufficient amount of information on the heat transfer involved.

The Second Attempt (Successful)

The only feasible choice at this point was to simply use a dataset interpolation to estimate the temperature change over the compressor in function of some operational conditions. More specifically, two input variables were chosen to predict the compressor temperature ratio (in Kelvin/Kelvin). It was decided to take the air massflow and the compressor pressure ratio as the two predictors.

The reasoning behind this selection is that in this case, as mentioned already, the temperature change is a consequence of both compression (work input) and heat transfer. Naturally, the degree of compression is best represented by the pressure ratio.

The air massflow was chosen since it influenced the degree of heat transfer: at high massflows, the heat capacity rate of the compressing air is larger, meaning the air temperature drop is less compared to low massflows for the same heat transfer. This was also seen in the measurement data: at low flows, the isentropic efficiencies were extremely high, sometimes exceeding 100% indicating the strong influence of the heat transfer. But at high flows, the isentropic efficiencies were closer to realistic results for radial compressors of around 70-75% [12], meaning the heat transfer effect was much smaller.

One could also argue that the compressor inlet temperature has an effect on the degree of heat transfer. This is completely correct. However, in every simulation done in this research (except for baseline validation simulations), the compressor inlet temperature was set to 20°C, which was also the inlet temperature used on the E-(turbo)compressor testbenches that generated the measurement data. Hence, for these simulations, there is no added value in implementing the compressor inlet temperature as a third predictor for the compressor temperature change.

Concluding, the Kelvin temperature ratio $\Theta_c = T_2/T_1$ over the compressor is estimated as a linear 2D interpolation of the data using massflow and pressure ratio:

$$\Theta_c = \text{map}(\dot{m}_a, \Pi_c) \tag{3.51}$$

The outlet temperature could then be computed (using Kelvin) simply through:

$$T_2 = T_1 \cdot \Theta_c \tag{3.52}$$

There are two main disadvantages with having to use this approach. Firstly, there is no real energy balance enforced, meaning the electrical consumption of the compressor E-motor (discussed below) could not be analytically computed from the change in air enthalpy.

The second disadvantage was the sensitivity on the conditions in which the datasets were generated, which have an influence on the heat transfer taking place. The maps used in this model come from an indoor E-compressor testbench where the ambient temperature was around 20°C. If the maps would be generated by driving the vehicle in colder weather and having fresh airflow over the E-compressor casing, it is obvious the temperature measurements would be different. Hence, the flexibility or ability of the model to predict accurately different operational conditions is somewhat limited.

The simulated ambient conditions should therefore preferably stay close to the ambient conditions present during the generation of the datasets. Otherwise, the results could be unreliable, especially considering the complete temperature range of the simulation. Since fuel cell systems operate at a low temperature compared to combustion engines (<100°C compared to e.g. ∼600°C), a 5°C misprediction in temperature could have a larger effect on other computed parameters compared to calculations in ICE-related research.

3.7.3 E-Compressor Electric Power Consumption

The compressor wheel gets mechanical (rotational) input power from a shaft that is driven by an E-motor that gets its electrical power from the fuel cell stack. Since the stack outputs DC current and the E-motor needs AC current, there is an inverter in between the stack and the E-motor. It is the electrical power sent from the stack to this inverter that is of interest: it is a direct measure of parasitic power loss.

As mentioned in the previous subsection, it is not possible to set up an energy balance to compute the necessary inverter power. Therefore, the only practical solution is to resort to interpolating datasets once again.

The exact implementation here is as follows. The data is used to compute a so-called 'compression system efficiency', defined as:

$$\eta_{c,sys} = \frac{\Delta H_a}{P_{inv}} = \frac{\dot{m}_a \cdot c_{p,a} \cdot (T_2 - T_1)}{I_{inv} \cdot V_{inv}} \tag{3.53}$$

where the inverter current and voltage I_{inv} and V_{inv} were direct measurements. This effectively lumps together the inverter, the E-motor with cooling, and the compressor wheel together as one component. Now, a map of $\eta_{c,sys}$ in terms of certain predictors could be generated.

In this case, the predictors to map the compression system efficiency are also chosen to be air massflow and pressure ratio, for the same reasons as stated above. Due to the definition of $\eta_{c,sys}$ in Equation 3.53, its value is dependent on the air enthalpy change over the compressor, which in turn depends on the degree of compression as well as heat transfer.

The inverter power could then be computed as follows:

$$\eta_{c,sys} = \text{map}(\dot{m}_a, \Pi_c) \tag{3.54}$$

$$P_{inv} = \frac{\dot{m}_a \cdot c_{p,a} \cdot (T_2 - T_1)}{\eta_{c,sys}} \tag{3.55}$$

At this point, the E-compressor model is ready, and can be integrated in the full system model. A diagram showing the inputs and outputs of the E-compressor model is shown in Figure 3.14.

The next step is to model a turbine side, that could be coupled to the already existing E-compressor model to construct an E-turbocharger model. This is explained in the next subsection.

3.7.4 E-Turbocharger Turbine Recovery and Electric Power Consumption

When developing the E-turbocharger component model, the new challenge was to accurately model the turbine side and couple it to the compressor side. The latter is modeled in the same fashion as explained before: a target air masflow is provided to the model and a PID-controller adjusts the speed to get there, and the temperature increase over the compressor is estimated using data maps.

However, since now a turbine is attached to the E-motor on the other side, a model has to be made that eventually is able to compute the required inverter power based on the combined effect of the compressor demand and the turbine recovery. This interaction has to be quantified as good as possible. To visualize the situation, an energy flow diagram applied to an E-turbocharger, is shown below:

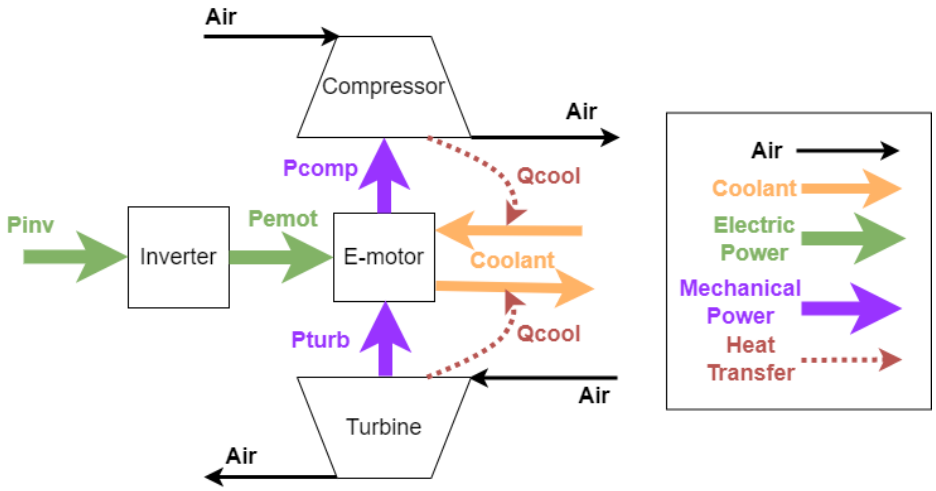

Figure 3.12: Schematic Showing the Energy Flows in an E-turbocharger

In order to compute the enthalpy change of the air at the turbine side (which is essentially the energy input into the turbine wheel), the air massflow going through the turbine as well as the temperature difference over the turbine has to be known. Getting the air massflow going in is straightforward: it is simply an input to the turbine model. This makes sense as in reality, a turbine wheel reacts on a massflow going through it.

When it comes to the temperature difference, the problem of non-negligible heat transfer once again arises. This is once again shown with a temperature-entropy diagram, this time for the turbine, in Figure 3.13.

This meant no energy balance could be made as again not enough information was available to accurately quantify the heat transfer, and yet again the need to resort to interpolation of data occurred. The implementation for the turbine side somewhat differed compared to the compressor side.

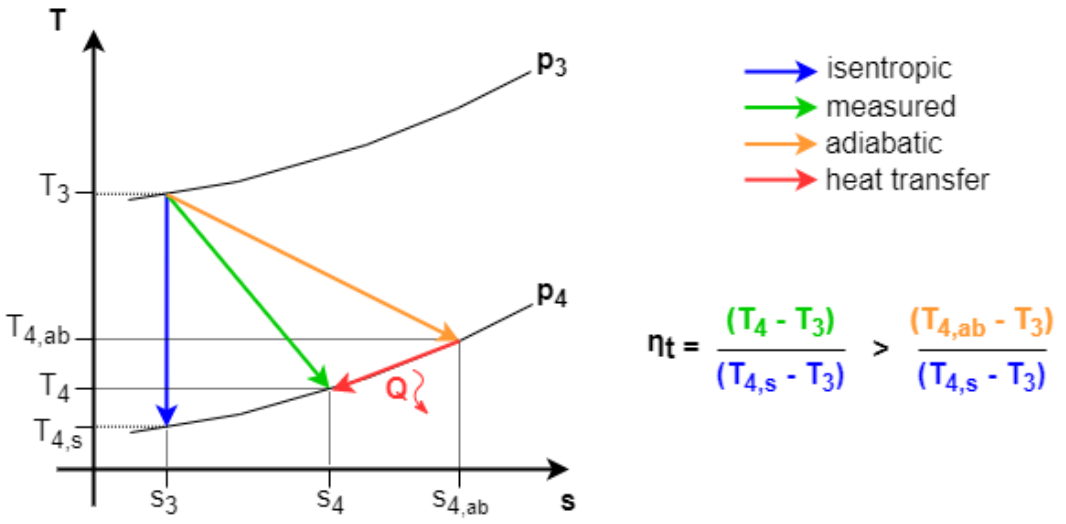

Figure 3.13: Temperature-entropy Diagram of an E-Turbine. Blue: Isentropic Expansion, Orange: Adiabatic Expansion (with Subscript 'ab'), Red: Heat Transfer from Air to Coolant, Green: Measured Expansion on a Testbench

In theory, for both the compressor and turbine, their inlet temperatures play a role on the amount of heat transfer that would take place. But for these simulations, the compressor inlet temperature is always set to 20°C and never varied. Therefore, the compressor inlet temperature was not considered a variable for predicting the temperature change from the data.

However, the inlet temperature for the turbine would differ between 50°C and 150°C for the various simulations, so now it had to be considered as a predictor variable, as it had a considerable influence on the temperature difference. In addition to the turbine inlet temperature, for the reasons already mentioned, also the air massflow and the pressure ratio are predictors for the temperature ratio.

The air massflow is a model input making it already known, but the pressure ratio is not. Unlike the compressor, which had as input both its inlet (boundary condition) and outlet pressure, the pressure ratio is not a direct input for the turbine: it has to be calculated somehow.

Computing the Turbine Pressure Ratio

Recalling the working of the pressure calculation chain: the system pressures are calculated by using the exhaust pressure boundary and then consecutively adding the pressure drop of each component, moving upstream the system. For the turbocharged model, this meant the pressure drop over the turbine has to be quantified somehow using known inputs.

The perfect tool for this job is the turbine throughput map, shown in the left plot in Figure 3.1. In the simulation, the speed of the compressor, which is identical to the speed of the turbine, is being controlled to obtain the given target massflow. This is therefore also available as a model input for the turbine. Thus, knowing the turbine speed and the air massflow it received, the throughput map could give exactly the resulting expansion ratio (pressure ratio). Therefore, the expansion ratio $\Pi_t = p_3/p_4$ is computed by linearly interpolating the data using speed and massflow:

$$\Pi_t = \text{map}(n, \dot{m}_{air}) \tag{3.56}$$

This in turn could be used to also compute the turbine inlet pressure, to continue the pressure calculation chain upstream.

$$p_3 = p_4 \cdot \Pi_t \tag{3.57}$$

Now, all three predictor variables to obtain the turbine temperature ratio $\Theta_t = T_3/T_4$ are known: $\dot{m}_a$, T_3 and Π_t. The way the prediction is made is explained now.

Computing the Turbine Temperature Ratio

Unfortunately, AVL Cruise M does not feature linear 3D interpolation of a dataset, meaning the operation $\Theta_t = \text{map}(\dot{m}_a, T_3, \Pi_t)$ could not be performed directly. Therefore, a workaround has been implemented: chaining two 2D maps together to predict the temperature ratio. The simplest way to describe this operation symbolically is as follows:

$$\Theta_t = \text{map}[\Pi_t, \text{map}(\dot{m}_a, T_3)] \tag{3.58}$$

However, to perform this the right way, a more formal description has to be outlined. In general, chaining two 2D maps together in order to estimate a target parameter using three predictors should be done as follows:

1. select the three predictors X, Y and Z for predicting the target variable A
2. using two predictors, e.g. X and Y, predict an intermediate variable W
3. using the remaining predictor Z and the intermediate variable W, predict A

Two conditions have to hold for this to work: variables X and Y have to be valid predictors for W, and variables W and Z have to be valid predictors for A. They cannot be chosen at random. A simple example is that the turbine rotational speed n is not a valid predictor for the temperature change, it depends on other things as discussed previously.

For the turbine model in this research, the following parameters were selected for X, Y, W, Z and A respectively:

- $X = \dot{m}_a$, the air massflow, a known input for the turbine model
- $Y = T_3$, the turbine inlet temperature, also a known input for the turbine model
- $W = \eta_t$, the turbine isentropic efficiency, predicted using $\dot{m}_a$ and T_3
- $Z = \Pi_t$, the turbine expansion ratio
- $A = \Theta_t$: the turbine temperature ratio, predicted using η_t and Π_t

This way, the turbine temperature ratio is computed by considering the effect of all three original predictors.

The reason why η_t is decided to be the intermediate variable is as follows. In the final map, Π_t would be used as the predictor representing the contribution of expansion to the temperature change. The other predictor had to be one that represented the contribution of heat transfer to the temperature change, and it had to have $\dot{m}_a$ and T_3 as valid predictors for itself, as set out by the above conditions for chained 2D maps.

As discussed multiple times before, the isentropic turbine efficiency represents the significance of the effect of heat transfer, since the more its value is greater than normal ($\sim$75% [12]), the bigger the heat transfer impact on the temperature change, as visualized by figure 3.13. This is exactly why the air massflow and turbine inlet temperatures are ideal predictors for η_t, which clarifies why it was chosen as the intermediate predictor W.

Finally, the way the turbine outlet temperature is compute is then:

$$\Theta_t = \text{map}(\Pi_t, \eta_t) = \text{map}[\Pi_t, \text{map}(\dot{m}_a, T_3)] \tag{3.59}$$

Again, calculating with Kelvin and not Celcius:

$$T_4 = \frac{T_3}{\Theta_t} \tag{3.60}$$

The final thing that has to be quantified is the inverter power, which is elaborated upon now.

Computing the E-turbocharger Inverter Power Consumption

In the case of an E-turbocharger, the inverter power intuitively depends on the necessary compressor power and the recovered turbine power. Since setting up energy balances is off the table for reasons mentioned multiple times above, the data is leveraged once again.

The inverter power is predicted based on two quantities: the compressor side air enthalpy change and the turbine side air enthalpy change, as these quantities could be computed during the simulation. The former is another wording for compressor wheel power input to the air, and the latter another wording for the air power input to the turbine wheel. They are defined in Equation 3.61 and 3.62. The inverter power is then simply the result of a 2D map interpolation using these predictors: $P_{inv} = \text{map}(\Delta H_{a,c}, \Delta H_{a,t})$.

$$\Delta H_{a,c} = \dot{m}_{a,c} \cdot C_{p,a} \cdot (T_2 - T_1) \tag{3.61}$$

$$\Delta H_{a,t} = \dot{m}_{a,t} \cdot C_{p,} \cdot (T_3 - T_4) \tag{3.62}$$

3.7.5 Overview of the Complete E-Compressor & E-Turbocharger Model

Figure 3.14 shows the E-compressor model layout while Figure A.2 shows the ETC variant.

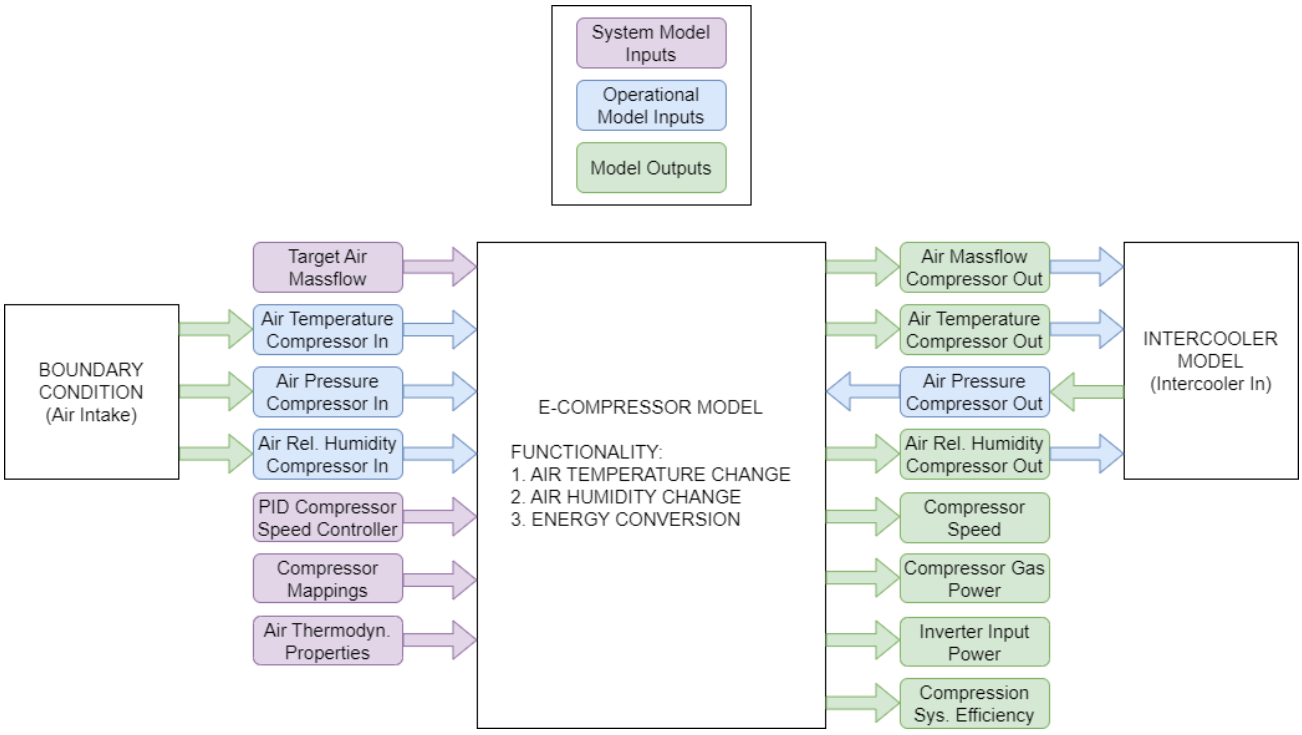

Figure 3.14: Schematic of the Inputs and Outputs of the E-Compressor Model

3.8 Pressure Valve and Water Separator Modeling

The pressure valve model used in the baseline system model and the water separator model used in the turbocharged system model are very similar in their setup. The only functionalities

that need to be modeled for these components are the temperature and pressure change.

3.8.1 Air Temperature Change

When it comes to the pressure valve, measurement data from the real system could be used to set up a simple map that takes as input the air massflow through the valve and gives back the temperature change. This could then be used to compute the valve outlet temperature based on the inlet temperature provided by the humidifier thermal model (wet outlet side).

For the water separator, no measurement data on temperatures was available, so for simplicity the component was seen as adiabatic: no heat transfer occurs within it, hence the temperature remains unchanged. This implied that the humidifier wet channel outlet air temperature would be the same as the water separator outlet (i.e. turbine inlet) air temperature.

For the turbocharged simulations with varying turbine inlet temperatures, the water separator outlet temperature was set to the desired value (e.g. 120°C), to keep it simple. That way, no extra heat exchanger model had to be developed and placed in between the water separator and turbine. The main goal is to see how the system performance increased in case of extra waste heat being put into the exhaust, hence this approach is sufficient.

3.8.2 Air Pressure Drop

As usual, since air pressure drop data is available for both the pressure valve and the water separator, the air massflow going through them is used to predict the pressure drop.

3.8.3 Overview of the Complete Pressure Valve Model

In terms of a diagram representation with inputs and outputs, both the pressure valve and water separator model are exactly the same. The schematic is shown in Figure 3.15.

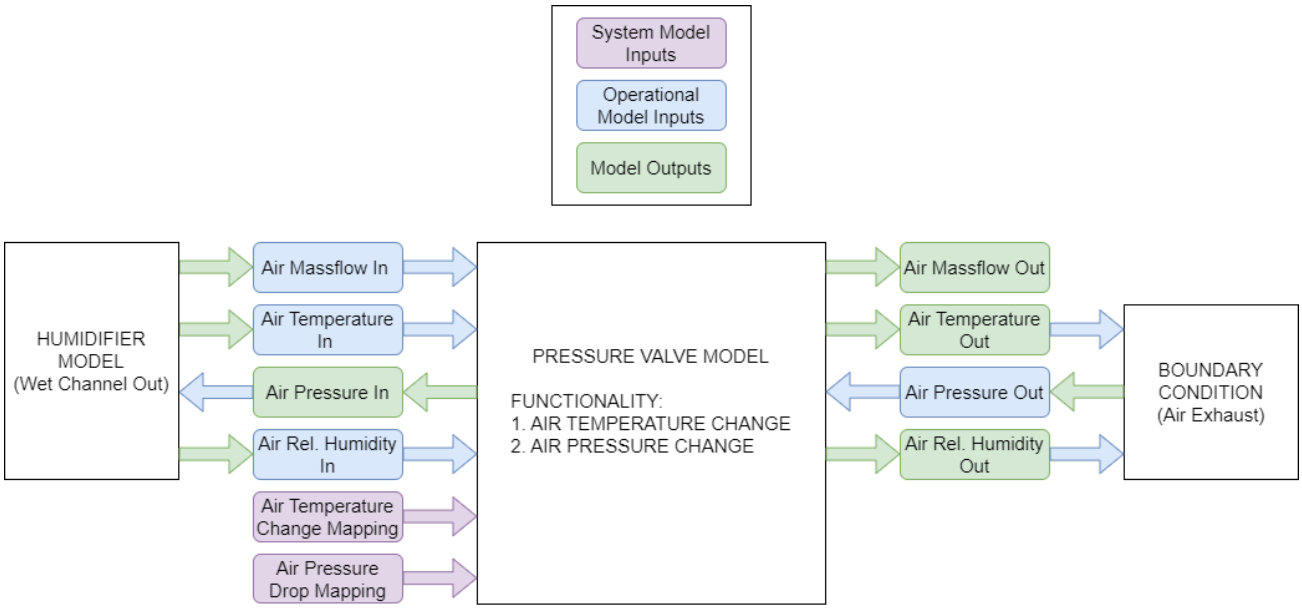

Figure 3.15: Schematic of the Inputs and Outputs of the Pressure Valve Model

Chapter 4

Results and Discussion

In this chapter, all the results generated with the AVL Cruise M simulations will be shown and discussed. Firstly, an overview of every simulation performed is provided. Subsequently, the validation of the baseline model is presented. Finally, the turbocharged model simulation results are shown and analyzed.

4.1 Detailed Overview of the Simulation Runs

Before all simulation results are shown, a list of each performed simulation with their corresponding inputs is presented in Table 4.1. The different columns in the table mean:

- Run: the unique identifier for each individual simulation
- Model: specifying whether the baseline or one of the turbocharged models (using ETC1 or ETC2) was used
- Power: indicating the approximate power level to be simulated
- Goal: states the reason for the simulation, there are four options: 1) validation of baseline model, 2) making reference runs using baseline to compare turbocharged models to, 3) simulate same net power output as the baseline reference, 4) simulate the same fuel consumption as the baseline reference
- Columns 5-9: show the resulting compressor outlet pressure (p_{co}) due to generated air massflow, the ambient temperature (T_{amb}), the compressor inlet pressure boundary (p_{ci}), the exhaust pressure boundary (p_{ex}) and the turbine inlet temperature (T_{ti}). 'Default' T_{ti} means it is not forced as an input but rather the result of the model calculations.

For convenience, when visualizing results later in the text, the corresponding run numbers of the simulations behind the shown data is always mentioned.

Table 4.1: Overview of All Performed Simulations with Respective Inputs

Run	Model	Power	Goal	p_{co} [bar]	T_{amb} [°C]	p_{ci} [bar]	p_{ex} [bar]	T_{ti} [°C]
1	Baseline	50kW	validation	1.2064	11.23	0.9956	1.0160	/
2	Baseline	70kW	validation	1.3711	11.65	0.9888	1.0190	/
3	Baseline	97kW	validation	1.7423	12.14	0.9754	1.0169	/
4	Baseline	50kW	reference	1.2065	20	0.9956	1.0160	/
5	Baseline	70kW	reference	1.3714	20	0.9888	1.0190	/
6	Baseline	97kW	reference	1.7424	20	0.9754	1.0169	/
7	ETC1	50kW	net power	1.2740	20	0.9956	1	default
8	ETC1	50kW	H2 usage	1.2863	20	0.9956	1	default
9	ETC1	50kW	net power	1.2710	20	0.9956	1	80
10	ETC1	50kW	H2 usage	1.2863	20	0.9956	1	80
11	ETC1	50kW	net power	1.2698	20	0.9956	1	100
12	ETC1	50kW	H2 usage	1.2863	20	0.9956	1	100
13	ETC1	50kW	net power	1.2694	20	0.9956	1	120
14	ETC1	50kW	H2 usage	1.2863	20	0.9956	1	120
15	ETC1	50kW	net power	1.2702	20	0.9956	1	150
16	ETC1	50kW	H2 usage	1.2863	20	0.9956	1	150
17	ETC1	70kW	net power	1.4695	20	0.9888	1	default
18	ETC1	70kW	H2 usage	1.4987	20	0.9888	1	default
19	ETC1	70kW	net power	1.4650	20	0.9888	1	80
20	ETC1	70kW	H2 usage	1.4987	20	0.9888	1	80
21	ETC1	70kW	net power	1.4627	20	0.9888	1	100
22	ETC1	70kW	H2 usage	1.4987	20	0.9888	1	100
23	ETC1	70kW	net power	1.4615	20	0.9888	1	120
24	ETC1	70kW	H2 usage	1.4987	20	0.9888	1	120
25	ETC1	70kW	net power	1.4600	20	0.9888	1	150
26	ETC1	70kW	H2 usage	1.4987	20	0.9888	1	150
27	ETC1	97kW	net power	1.7504	20	0.9754	1	default
28	ETC1	97kW	H2 usage	1.8224	20	0.9754	1	default
29	ETC1	97kW	net power	1.7425	20	0.9754	1	80
30	ETC1	97kW	H2 usage	1.8224	20	0.9754	1	80
31	ETC1	97kW	net power	1.7372	20	0.9754	1	100
32	ETC1	97kW	H2 usage	1.8224	20	0.9754	1	100
33	ETC1	97kW	net power	1.7332	20	0.9754	1	120
34	ETC1	97kW	H2 usage	1.9132	20	0.9754	1	120
35	ETC1	97kW	net power	1.7278	20	0.9754	1	150
36	ETC1	97kW	H2 usage	1.9143	20	0.9754	1	150
37	ETC2	50kW	net power	1.5460	20	0.9956	1	default
38	ETC2	50kW	H2 usage	1.5654	20	0.9956	1	default
39	ETC2	70kW	net power	2.0209	20	0.9888	1	default
40	ETC2	70kW	H2 usage	2.0517	20	0.9888	1	default
41	ETC2	97kW	net power	2.6399	20	0.9754	1	default
42	ETC2	97kW	H2 usage	2.7087	20	0.9754	1	default

4.2 Baseline Model Validation and Reference Simulations

To validate the generated baseline model that was supposed to mimic the behavior of the current hardware, simulation runs 1 to 3 from Table 4.1 were performed and analyzed. From the table it can be seen that specific ambient temperatures wer used, as well as compressor inlet and exhaust pressure boundaries. These values came from the measured validation data, to give the model the correct starting point. As can be seen, it was a rather cold day when the validation data was collected, as the ambient temperatures were around 12°C.

The comparison between validation data and model results is split up in three parts. The air pressures and temperatures are visualized and compared first, as they have the biggest impact on the rest of the model outputs. After that, more details on the output of the E-compressor and fuel cell stack models follow. Finally, a comparison is made between overall system model outputs and their corresponding validation points.

4.2.1 Air Path Results - Validation

The chosen modeling points in the system to compute air pressures and temperatures naturally overlapped with the sensor positions inside the validation vehicle, namely before and after each component in the air path. A layout is shown to guide the subsequent data visualizations:

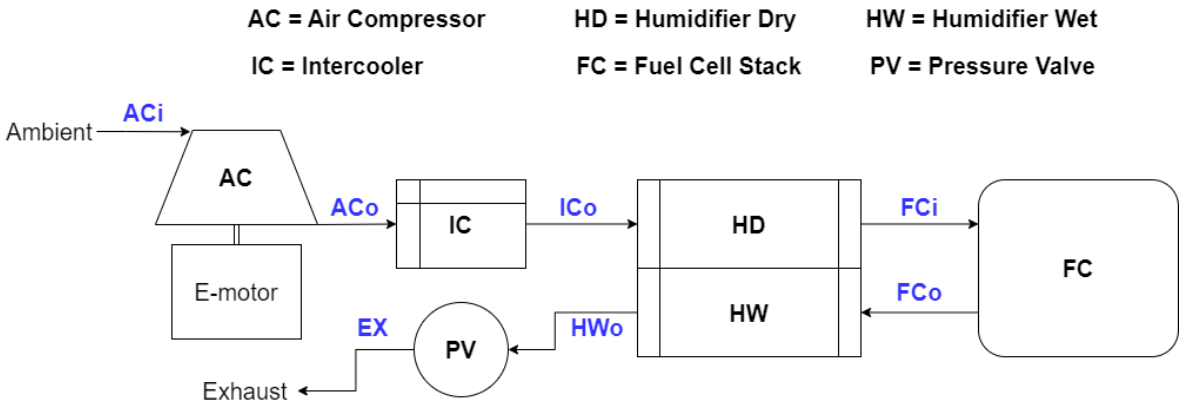

Figure 4.1: Layout of the Air Path Modeling Points

At the blue points in the above schematic, the air pressures and temperatures were simulated and compared to the validation data. The model percentage errors shown throughout this chapter are defined as:

$$error = \frac{model - data}{data} \cdot 100\% \tag{4.1}$$

with the units of the model and the data values being consistent. This way, positive model errors show model overestimation, and negative errors show underestimation.

Firstly, for the 50kW simulation (run 1), the pressure and temperature validation are shown in Figures 4.2 and 4.3 respectively.

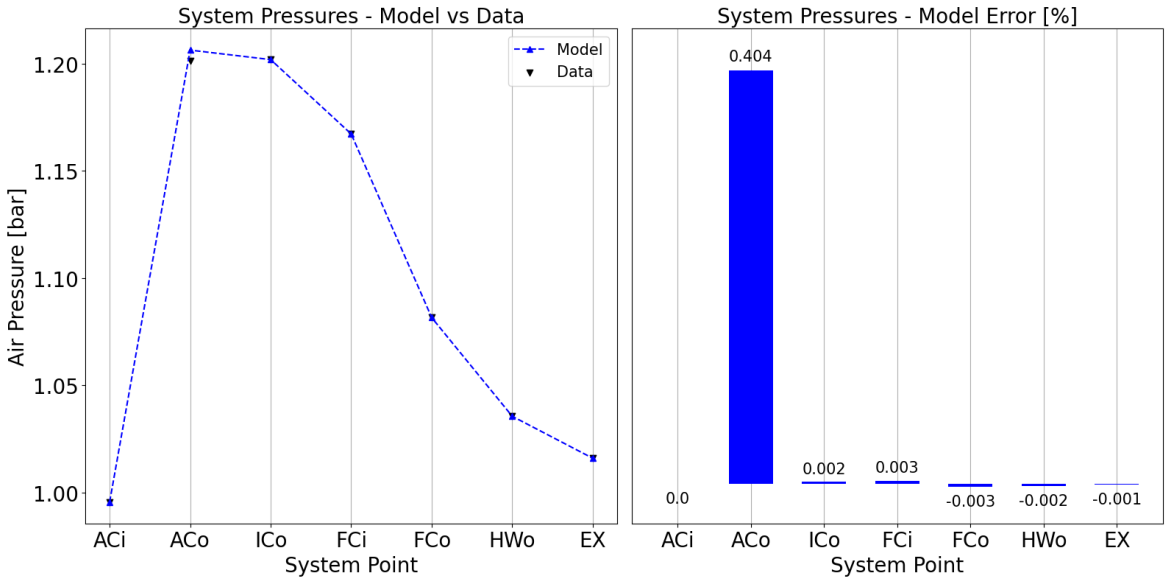

Figure 4.2: Validation of System Air Pressures for 50kW Stack Power

Over the compressor, the pressure obviously increases, but after that, the air only experiences pressure drops. The slope of the blue dashed line indicates the magnitude of the pressure drop over each component. The biggest pressure drop always occurred over the fuel cell stack, and the smallest one over the intercooler.

One should also remember that the measured pressure drop over the intercooler was faulty: a pressure rise was indicated, which is not realistic, but is a result of insufficient sensor accuracy. A theoretical pressure drop model was thus pursued to calculate an actual pressure drop. That is why the data usually shows an increase over the intercooler while the model shows a decrease. However, as expected, the difference is negligible.

The model pressures match the measured pressures quite well, which is not a surprise. First, it should be noted that the pressures at ACi and EX were set to the measured values as boundary conditions. As explained in Chapter 3, the pressures between ACi and EX (except ICo) were simply predicted by using air massflow to interpolate data from the validation measurements. Therefore, it is more consistent to call these verification results, as the model was fitted to the measurements shown here.

The one pressure that had to be validated was the compressor outlet pressure. The pressure rise over the compressor was modeled using the test bench data of the E-compressor. This was not the same as the vehicle validation measurement. However, the model error is small (0.4%). The next figure shows the temperatures:

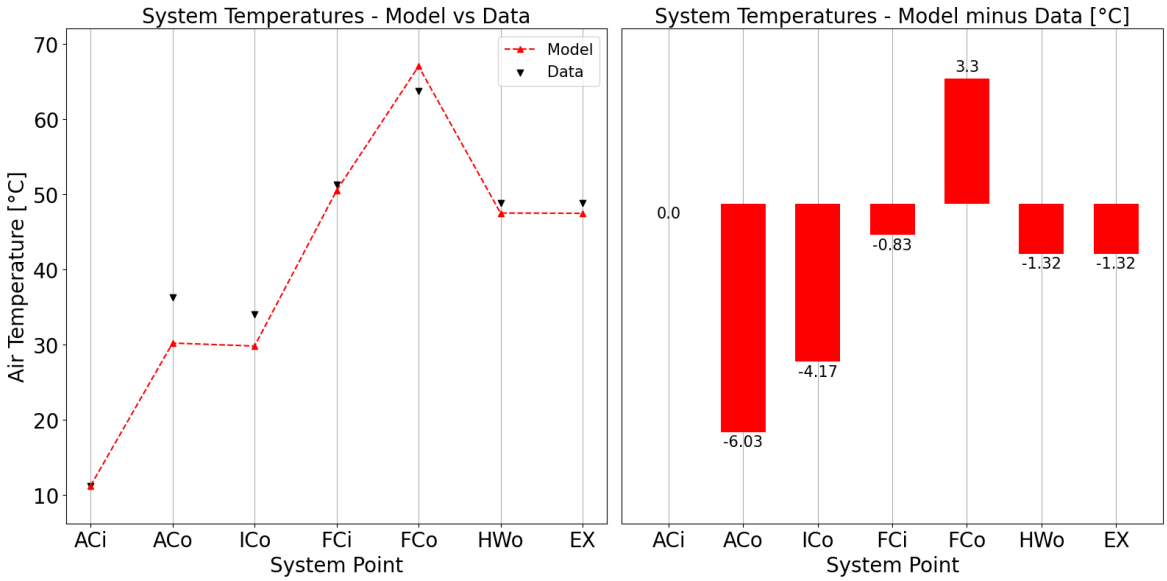

Figure 4.3: Validation of System Air Temperatures for 50kW Stack Power

To visualize temperature errors, the absolute difference between the model output and the measurement data is presented, as relative model errors don't work: relative errors differ when using Fahrenheit vs Celcuis vs Kelvin in equation 4.1. Over the compressor, the temperature obviously rises and over the intercooler the air cools down. In the dry channel of the humidifier (ICo to FCi), the air heats up due to the hot exhaust air that gives off heat in the humidifier wet channel (FCo to HWo). Over the stack, the air heats up to coolant temperature, and over the pressure valve (HWo to EX) there is almost no temperature change.

Right from the start, the model significantly underpredicts the compressor outlet temperature with a magnitude of over 6°C. This can be explained by the difficulties of modeling the heat transfer inside an E-compressor as mentioned in the previous chapter. The temperature change was modeled using data mappings coming from a stationary indoor test bench, while the validation data in the figure comes from a vehicle driving outside in 12°C weather. Obviously, the heat flows through the E-compressor vary greatly between the two situations, which is why the predicted outlet temperature also differs significantly. This dependency on situation-specific datasets is the biggest weakness seen in the simulation models.

The other temperatures seem much better. The error on the intercooler outlet temperature is misleading: if one considers the temperature drop over the intercooler (i.e. the slope), the error is smaller. The temperature drops only slightly since at 50kW, the intercooler coolant pump runs on the lowest setpoint. The fuel cell stack outlet temperature is overestimated by about 3°C. The simple explanation is that the sensor for this temperature was not located right at the stack outlet, it was mounted on a tube right after the air exit shutoff valve for easier installation. This means that this sensor reads a lower value than what really happens at the stack outlet due to some temperature loss. In reality, the stack air outlet temperature would thus be a bit higher and the model estimate is actually good.

For the 70kW air path model validation (run 2), visualized in Figures 4.4 and 4.5.

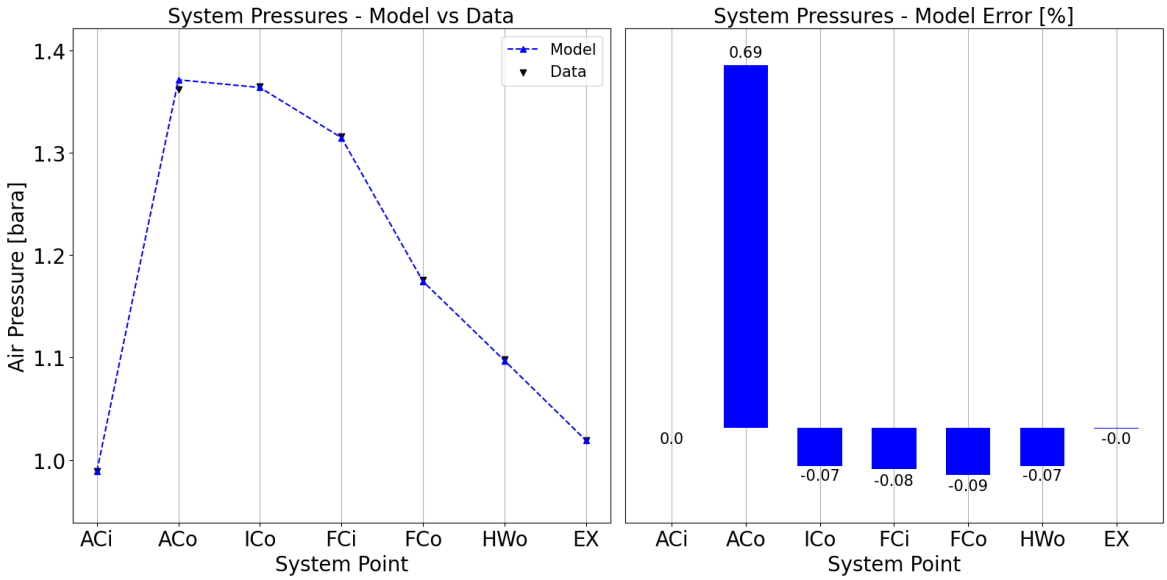

Figure 4.4: Validation of System Air Pressures for 70 kW Stack Power

As expected, the pressures match the measurement data well once again. The stack has the biggest pressure drop, around 140mbar. The calculated intercooler pressure drop is around 7.5mbar, which is expected for an intercooler of this size, and indeed below the measurement accuracy of the used sensors.

Looking at the temperatures in Figure 4.5, the compressor outlet temperature is now quite a bit higher than at 50kW. Now predicted at around 47°C, it is still underestimated by 5.7°C. This is a smaller error compared to the 50kW case, especially relative to the 70kW data. The decrease in error can be attributed to the increase in air massflow through the compressor between the 50kW and 70kW simulation. As stated in the last chapter, increasing compressor air massflow decreases the influence of heat transfer. For the temperatures of the 97kW run, this becomes even more clear as discussed later in this subsection.

The intercooler outlet temperature error is now smaller compared to the 50kW simulation, and this is due to the fact that the coolant heat transfer coefficient is significantly larger due to the intercooler coolant pump running on higher speed and thus creating more coolant massflow. The cooling effect is thus quite strong and there can be a certain air temperature variation at intercooler inlet that will still give a very similar air outlet temperature, which is seen in this plot. The humidifier dry and wet outlet temperatures (FCi and HWo) were estimated quite well by the model with overestimations of less than 1°C.

Moving on to the 97kW validation simulation (run 3), the pressures and temperatures are visualized once more in Figures 4.6 and 4.7.

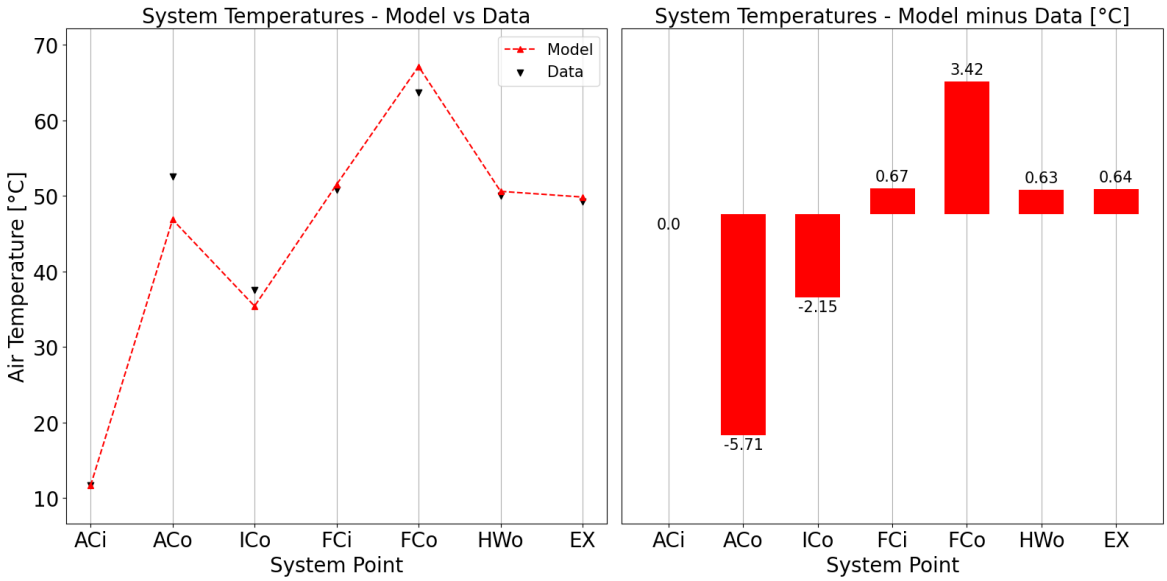

Figure 4.5: Validation of System Air Temperatures for 70kW Stack Power

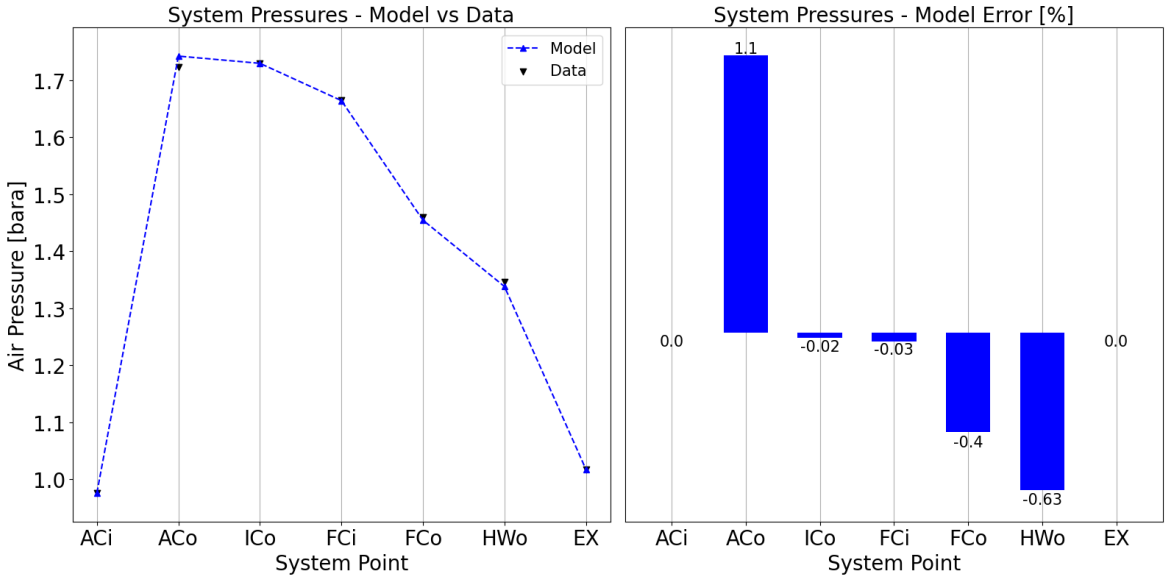

Figure 4.6: Validation of System Air Pressures for 97 kW Stack Power

The air pressure errors seem small again as expected, but there are some differences with the other runs. The compressor outlet pressure error has grown consitently from around 0.4% at 50kW to 1% at 97kW, which is very low in absolute sense, but indicates a dependence on the air mass flow. This could be due to the small differences in sensor readings on the vehicle versus on the testbench.

What is more notable is the relatively big difference between the errors of the pressures before and after the stack. The humidifier dry channel inlet and outlet pressures (ICo and FCi) feature a model error of -0.03% or less, but the wet channel pressure errors are now bigger than usual. This could likely be due to the fact that the simulated massflow at the stack outlet is smaller compared to what is happening in the real vehicle. This would be a result of some small errors in the fuel cell stack model, which will be discussed below.

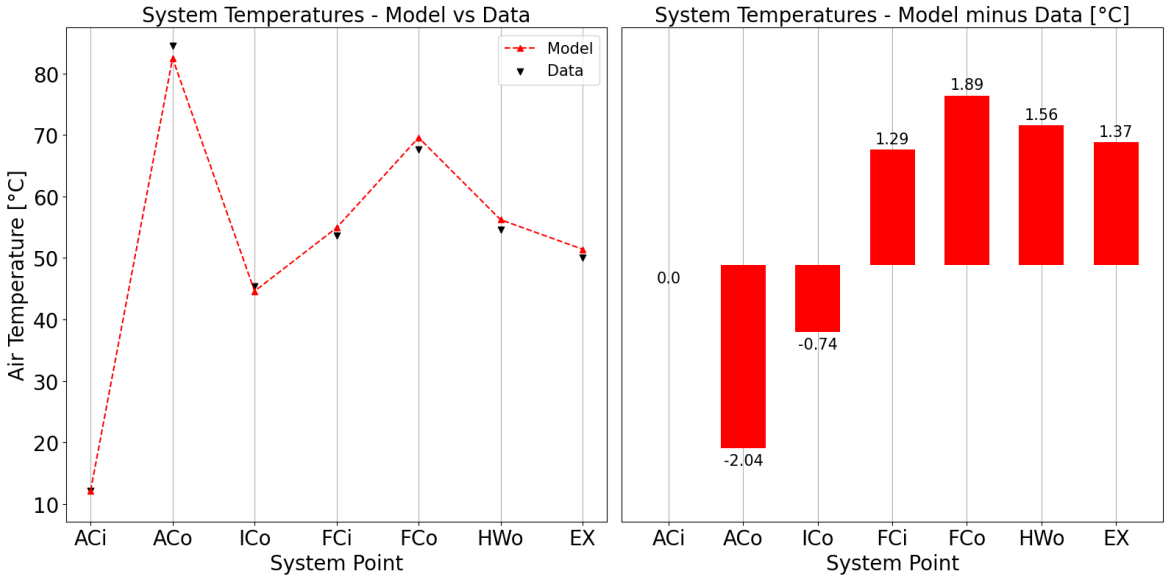

Figure 4.7: Validation of System Air Temperatures for 97 kW Stack Power

For the air temperatures at 97kW (Figure 4.7 above), now the error for the compressor outlet temperature is comparable to the other temperature errors in the air path. This confirms what was said earlier regarding that at higher air massflows, the heat transfer effect is less and therefore the model predictions are more accurate.

The intercooler model now also very accurately predicts its outlet temperature, both because the inlet temperature was estimated well by the compressor model but also because the coolant heat transfer coefficient is now largest as the pump is running on full speed.

The stack outlet temperature error is also lower compared to the approximately 3.3°C error at 50kW and 70kW, most likely due to the fact that the temperature loss between the actual stack outlet and the sensor position is reduced due to the whole system being warmed up. It is clear that the temperatures are better predicted at increasing system powers.

4.2.2 Compressor Results - Validation

In order to get a better view on the performance of the compressor model, the most relevant parameters were tabulated and compared. For each run (1 - 3), their outputs were compared

to the actual validation data and the model error was quantified. The considered parameters are: the pressure ratio Π_c, the temperature ratio Θ_c, the compressor speed n, the compressor air enthalpy change $\Delta H_{a,c} = \dot{m}_{a,c} \cdot Cp_a \cdot \Delta T_{a,c}$, the compressor inverter power P_{inv} and the compression system efficiency $\eta_{c,sys} = \Delta H_{a,c}/P_{inv}$. The output of the model next to the actual measurements of the real baseline sytem are shown in Table C.1 of Appendix C, but a summary on the validation errors is tabulated below in Table 4.2.

Table 4.2: Validation Errors of Compressor Model

	$\mathbf{\Pi_c}$	$\mathbf{\Theta_c}$	**n**	$\mathbf{\Delta H_{a,c}}$	$\mathbf{P_{inv}}$	$\eta_{\mathbf{c,sys}}$
50 kW error [%]	0.41	-1.93	0.98	-24.12	-8.62	-16.98
70 kW error [%]	0.73	-1.75	1.30	-13.96	-0.96	-13.20
97 kW error [%]	1.08	-0.56	2.97	-3.01	0.02	-3.03

The first column shows the pressure ratio model error. It is very small, and consistent with the compressor outlet pressure errors seen in the previous air path plots. The temperature ratio errors seem small at first glance, but knowing the large model errors for the compressor temperature outlet at 50kW and 70kW that might seem strange. However, the temperature ratio itself is defined using Kelvin/Kelvin, which is the reason why a small percentage change in temperature ratio can result in a significant change in computed outlet temperature in °C: $T_2[°C] = T_1[°C] \cdot \Theta_c + 273[°C] \cdot \Theta_c - 273[°C]$.

The compressor speeds seem to match well, with the model errors staying below 3% but consistently increasing. One cause of this could be that the compressor map serving as the model input has a lower concentration of datapoints in the higher pressure ratio and masslfow region, making the interpolation estimate more rough.

The compressor air enthalpy change depends on the temperature change, which is poorly estimated at 50kW and 70 kW. This error propagates to the enthalpy change calculation as can be seen, with model errors of around -24% and -14% for the 50kW and 70 kW runs. These errors propagate further into the compression system efficiency. As explained in the previous chapter, $\eta_{c,sys}$ was estimated using a dataset with predictors Π_c and air massflow. However, the values of $\eta_{c,sys}$ in the dataset are heavily dependent on the heat transfer, and therefore the big error model is seen here.

Finally, the predicted inverter powers are quite accurate for 70kW and 97 kW. For 70kW this should be attributed to coincidence: both the enthalpy change and the compression system efficiency are mispredicted due to heat transfer influences, but their ratio (being the inverter power) comes out just right. For 90kW the estimate is good since it is more robust against heat transfer. For 50kW, the inverter power error is then obviously the largest.

Overall, it is quite clear that the prediction of the compressor temperature increase is critical for obtaining most other parameters, and the accuracy of this prediction is heavily dependent on the datasets provided for the model. This is once again a confirmation that this is the biggest weakness in the whole simulation model. In a later subsection, the effect of these model errors on other system parameters will be shown.

4.2.3 Fuel Cell Stack Results - Validation

The main parameters regarding the fuel cell stack model are the air stoichiometry λ_a, stack current I_{fc}, stack voltage V_{fc}, the resulting stack power P_{fc} and the stack coolant temperature increase ΔT_c. The full validation is shown in Table C.2 in Appendix C, but again the validation errors are tabulated below:

Table 4.3: Validation Errors of Stack Model

	λ_a	I_{fc}	V_{fc}	P_{fc}	ΔT_c
50 kW error [%]	0.89	0.04	0.62	0.64	-0.57
70 kW error [%]	-0.70	1.62	-0.15	1.46	9.71
97 kW error [%]	0.12	0.64	-1.22	-0.59	0.63

The errors are overall quite low. For the stoichiometry this definitely makes sense as it is based on a data map with stack power as the predictor, and the input target massflow for the simulation is chosen to generate the desired power. And since air massflow and stoichiometry are related to the current, those model errors are also very low.

The stack voltage is modeled by the polarization curve which had its coefficients fitted on measurement data from the stack on a testbench. The parameters seem to have been fitted well since the errors again are quite low. And because the product of stack current and voltage gives power, the stack power is also accurately predicted.

Finally, coming to the coolant temperature change, which is used to compute stack coolant outlet temperature and thus also air outlet temperature, the errors are small, except for the 70kW run. An overestimation of almost 10% occurred. This was concluded to be due to outlier measurements in the validation data: at around 70kW, the coolant temperature change seems to drop around 1°C and then goes back up, which is not consistent with the stack testbench data that was used in the model, where the coolant temperature change grows more monotonously (which seems more realistic).

4.2.4 Air Processing System Results - Validation

The final part of the validation consisted of zooming out on the total system model and quantifying model errors of the main performance parameters. These were chosen to be the system net power $P_{net} = P_{fc} - P_{inv}$, system efficiency $\eta_{sys} = P_{net}/P_{fc}$ and the hydrogen consumption $\dot{m}_{H2}$. For reference, some quantities influencing the aforementioned parameters are shown in Table C.3 of Appendix C. The validation errors only can be found in the table below:

Table 4.4: Validation Errors of Air Processing System Model

	$\dot{m}_a$	P_{inv}	P_{fc}	P_{net}	η_{sys}	$\dot{m}_{H2}$
50 kW error [%]	/ (input)	-8.62	0.64	0.91	0.28	0.14
70 kW error [%]	/ (input)	-0.96	1.46	1.60	0.14	1.65
97 kW error [%]	/ (input)	0.02	-0.59	-0.66	-0.07	0.60

The net power model errors are quite small. The reason for that is that they seem mainly governed by the stack power model error as this is the bigger value compared to the inverter power. Therefore, also at 50kW there is a good net power estimate even though the inverter input power model error is almost -9%. Continuing to the full system efficiency, the errors are even lower with the biggest error being only 0.28%. Finally, since the hydrogen consumption is directly calculated from the current which had a very low model error, their errors are also very small. Overall, the baseline model predicts the validation data with sufficient accuracy, and the model was considered to be ready for the next steps in the research.

4.2.5 Baseline Model Results - Reference

After the baseline validation, the next step was to generate the reference baseline simulation runs to compare the turbocharged results to. These are simulation runs 4 to 6 in Table 4.1. The only input that was changed (compared to runs 1 to 3) to perform these simulations was the ambient temperature, which was set to a constant 20°C. This would also become the ambient temperature for all the subsequent turbocharged model simulations. Since these results do not differ much compared to the validation simulations, the reference runs are documented in Section A.3 of Appendix A for the sake of brevity.

4.3 Turbocharged Model Simulations with ETC1 and ETC2

The turbocharged model was developed in order to answer the main research questions, RQ2, 3 and 4 (Section 1.2). Now it is finally time to dive into the results and look at the answers. The simulations have been performed with two different E-turbochargers in the system, ETC1 (the bigger one) and ETC2 (the smaller one). Results from both turbocharged system simulations will be shown and compared, starting again with the air path. After that, the overall increase in system performance for both E-turbochargers is visualized and discussed.

4.3.1 Air Path Results

Figure 4.8 shows the turbocharged layout of the air path with corresponding system points where the air pressure and temperature were calculated.

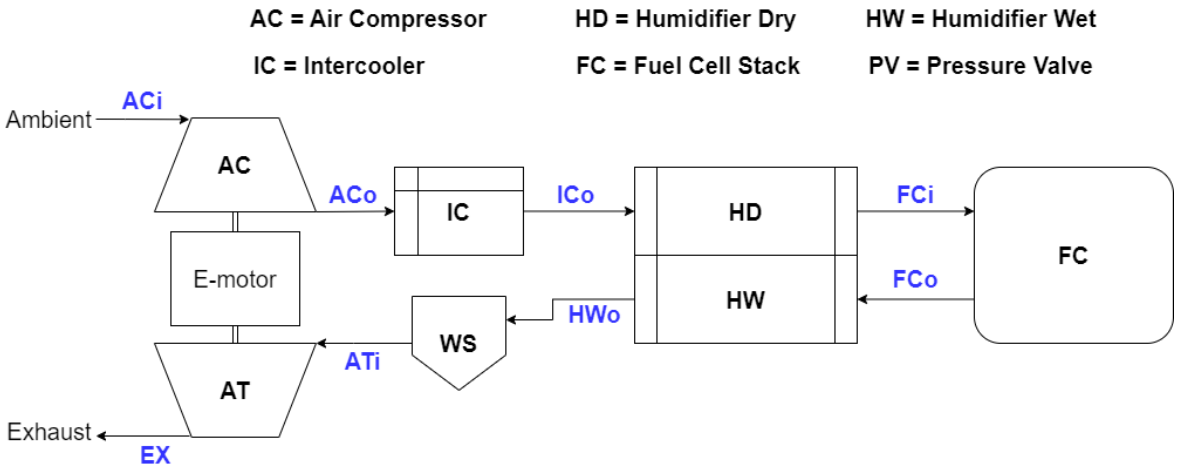

Figure 4.8: Layout of the Turbocharged Air Path Modeling Points

Starting at the 50kW point, the reference baseline model is compared to the ETC1 and ETC2 turbocharged models to show the difference in operational conditions throughout the air path. Figure 4.9 combines run 4 (baseline), run 7 (ETC1) and run 37 (ETC2). The latter two are turbocharged runs at the same net output power as the 50 kW baseline reference run. The compressor inlet pressures were thus equal for every model, but for the turbocharged models, the exhaust pressure is always set to 1bar since no real-life data was available from a vehicle-installed turbocharged system.

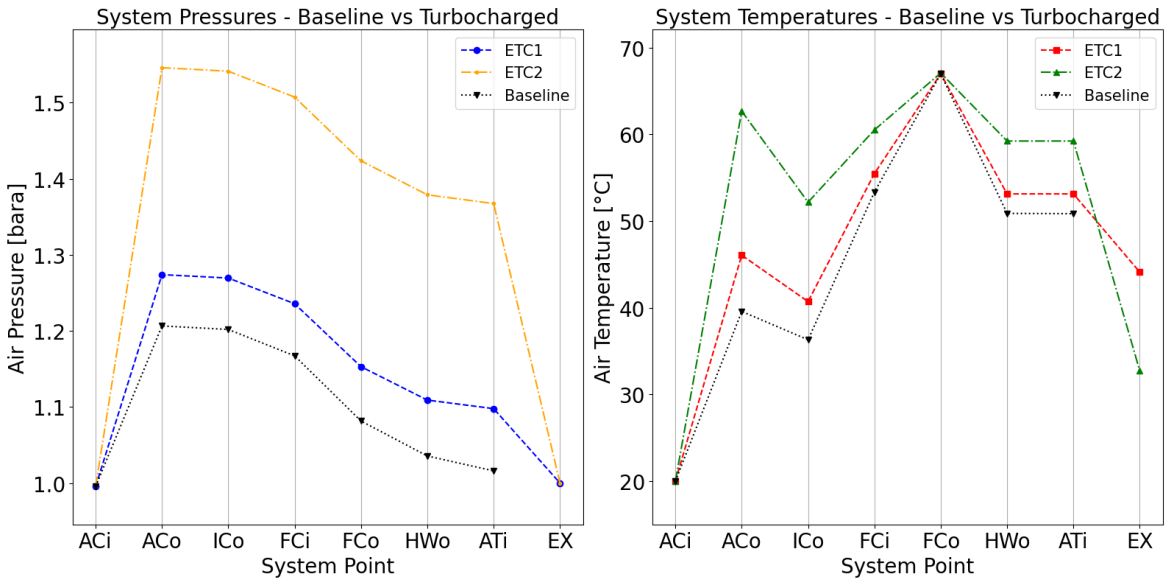

Figure 4.9: Baseline and Turbochared Model Air Pressures & Temperatures, 50kW Stack Power

First looking at the pressures (left graph in Figure 4.9), the black dotted line shows the baseline pressure profile which was already known. The blue line shows the pressure profile of the big E-turbocharger (ETC1), while the orange line shows the pressure profile of the small E-turbocharger (ETC2). A first impression is that ETC2 puts the system at a significantly higher operating pressure compared to both the baseline and ETC1. The turbine of ETC2 causes a turbine inlet pressure of nearly 1.37bar, and the compressor pressure ratio is around 1.55. Meanwhile, the turbine of ETC1 creates around 1.1bar at inlet and its compressor runs at a pressure ratio of 1.28. So the turbine inlet pressure of ETC2 is about 1.25 times larger than ETC1 (1.37bar/1.1bar). Considering the boost pressures then, ETC2 provides nearly twice the amount of boost as ETC1 does (0.55/0.28). This will have an effect on both the stack voltage as well as the compressor power consumption, which will be shown later.

For the temperatures (right graph in Figure 4.9), the results are as expected. Higher compression ratios lead to higher compressor outlet temperatures, with the ETC2 compressor outlet temperature close to 63°C. Since the coolant flow through the intercooler is low at this stack power level (due to vehicle control logic for the pump), the intercooler outlet temperatures vary quite a bit for each of the three systems.

At the fuel cell stack, as explained before, the air will always adapt to coolant temperature since that is the thermally stronger fluid. This can be seen at point *FCo*: all three air temperatures are now the same. However, since the temperatures in the dry channel of the humidifier are higher for ETC1 and higher still for ETC2, the wet air in the wet channel of the humidifier cools down less compared to the baseline, which makes sense from a heat transfer perspective. Lastly, the temperature drop over the turbine is obviously higher for ETC2 as its expansion ratio is higher than ETC1.

The same graph, now for the 70kW power level, is shown in Figure 4.10. This graph combines the results of simulation runs 5 (baseline), 17 (ETC1) and 39 (ETC2).

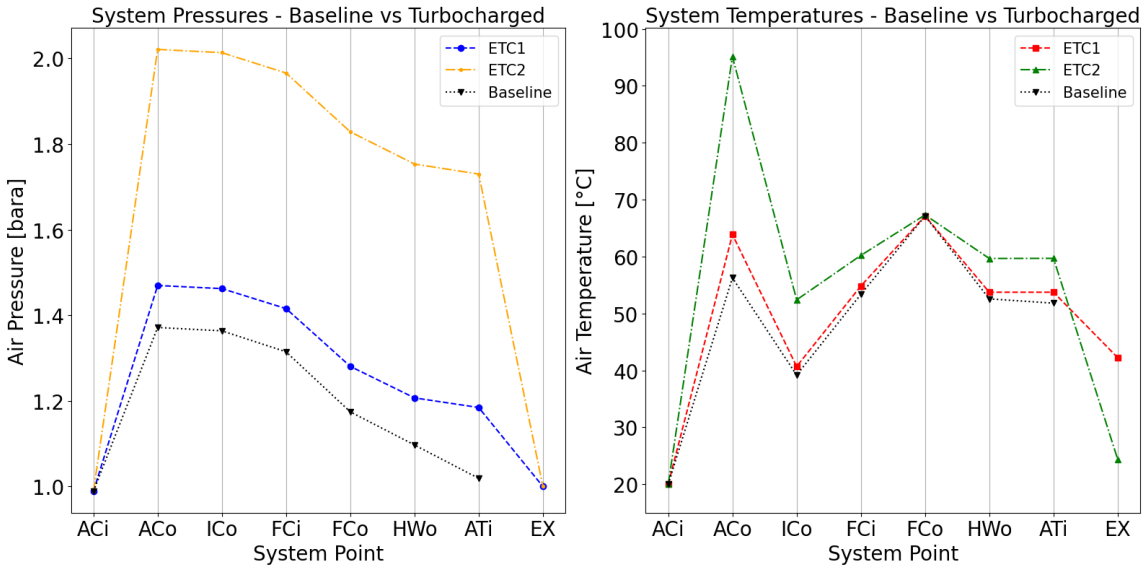

Figure 4.10: Baseline and Turbochared Model Air Pressures & Temperatures, 70kW Stack Power

Due to the higher massflow, the ETC2 turbine causes even more turbine inlet pressure: 1.73bar. ETC1 however, has not yet really 'spooled up', its turbine inlet is around 1.19bar. Hence, this time ETC2 causes close to 1.5 times the amount of turbine inlet pressure as ETC1. The compressor pressure ratio of ETC2 is now just above 2, while the ETC1 pressure ratio is just below 1.5. The boost pressure (defined relative to the ambient) of ETC2 is thus still twice as high as that of ETC1.

At 70kW, the intercooler coolant flow is significantly higher compared to 50kW, making the cooling more effective. This can be seen: the intercooler outlet temperatures of the baseline and ETC1 systems are nearly the same, even though ETC1 has an intercooler inlet temperature that is around 8 degrees higher. Additionally, for the ETC2 system, the air cools down from around 95°C to about 52°C (-43°C change), showing that the intercooler model seems to behave well even outside the validation data range (there the maximum compressor outlet temperature was around 85°C), which was the purpose of implementing the $\epsilon - NTU$ method laid out in the previous chapter. The behavior of the other temperatures (stack, humidifier and turbine) is consistent with what was mentioned before.

The last air path graph is shown in Figure 4.11. This graph concerns 97kW-simulation runs 6, 27 and 41.

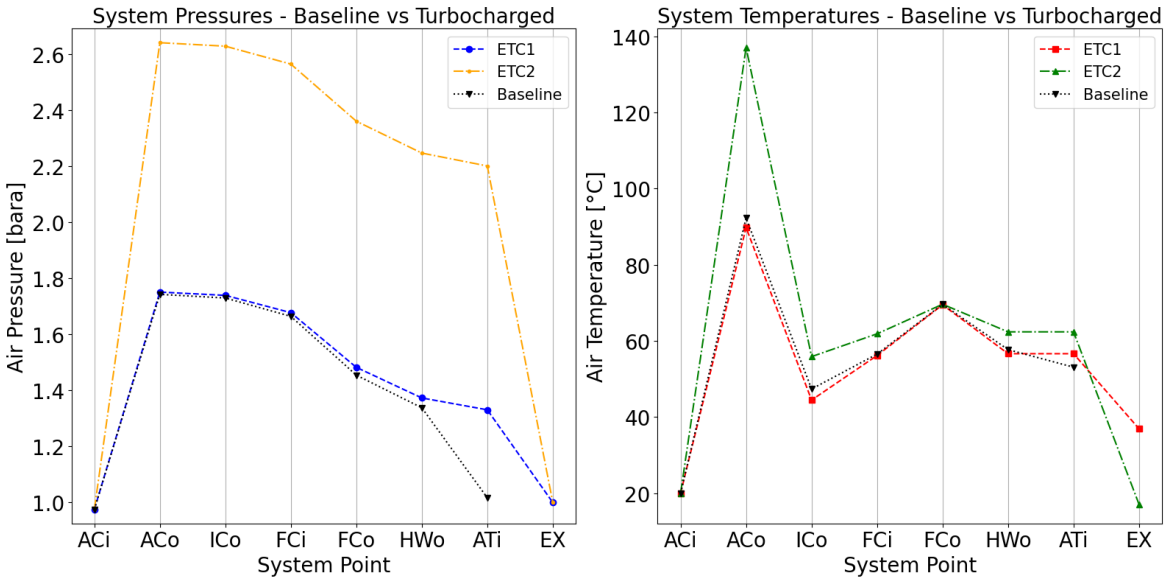

Figure 4.11: Baseline and Turbochared Model Air Pressures & Temperatures, 97kW Stack Power

Most notable here regarding the pressure graph, is that the baseline system and the ETC1 system seem to operate at almost the same system pressures, as their compression ratios are around 1.8. The pressure drops through the baseline system however seem to be higher, as the black dotted line falls more below the blue one as the air path progresses. This is due to the lower air massflow that is needed by ETC1 for generating the same net power as the baseline, and therefore yielding smaller pressure drops. The reason why both systems

operate at almost the same compression ratios is due to coincidence: at this power level, the inlet pressure of the ETC1 turbine is very close to the inlet pressure of the pressure valve in the baseline system. This pressure valve opens or closes according to vehicle control logic. Comparing ETC1 and ETC2 once more, the inlet pressure of the ETC2 turbine is around 2.2bar and therefore almost 1.7 times higher than the ETC1 turbine inlet pressure (1.33bar). The compressor pressure ratios for ETC1 and ETC2 are 1.75 and 2.7 respectively, meaning ETC2 provides over 2.2 times more boost pressure compared to ETC1.

At 97kW of power, the intercooler coolant flow is maximal. This is why the intercooler outlet air temperatures for all three systems lie quite close to eachoter, even though the difference between the intercooler inlet temperature of the baseline and the ETC2 model is about 45 degrees Celcius.

4.3.2 Comparing the Baseline, ETC1 and ETC2 Model at Same Fuel Usage

All three system configurations have also been simulated with the same fuel consumption. This means that the x-axes of the plots usually shows the current (equivalent to air massflow) pulled from the fuel cell stack. At the same fuel consumption as the baseline system, the turbocharged system will make more net power as it should be more efficient. Just how much more power depends on the setup, and this is quantified in Figure 4.12 for both the ETC1 and ETC2 systems. This graph as well as the other ones in this subsection contain results from simulation runs 4-5-6 (baseline), 8-18-28 (ETC1) and 38-40-42 (ETC2). The uncensored equivalent showing actual stack currents in amperes is shown in Figure C.1.

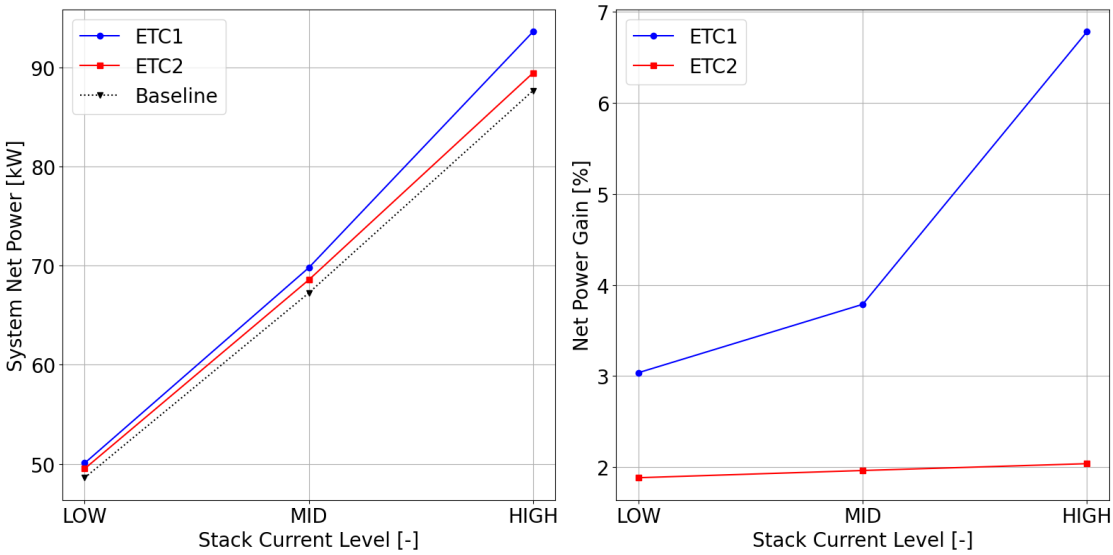

Figure 4.12: Net Power Output of the Baseline and Turbocharged Models, Same Current Levels

The left graph shows the absolute values of the net output power of the system for all three configurations (baseline, ETC1 and ETC2). It is clear that the baseline outputs the least net

power, as expected. It is interesting to see however, that for all three currents (corresponding to about 50, 70 and 97kW power levels), it is ETC1 that yields the most net power, despite ETC2 providing usually twice as high boost pressures.

In the right graph, the percentage increase in net power compared to the baseline system is shown. The ETC2 system stays around 2% over the whole power range, while the ETC1 system improves its power boost significantly from around 3% at 50kW to nearly 7% at 97kW. This makes sense as it has the bigger turbine that starts kicking in at higher flows.

Counter-intuitively, it is seen that ETC2 does not provide more net power than ETC1 at the lower power range. To dive deeper into why this occurs, a first good step is to identify in which regions of the compressor and turbine maps the sytem is operating at the three different power levels of 50, 70 and 97kW. See Figure 4.13 below, the power levels are indicated as LOW, MID and HIGH on the x-axis (uncensored: Figure C.2).

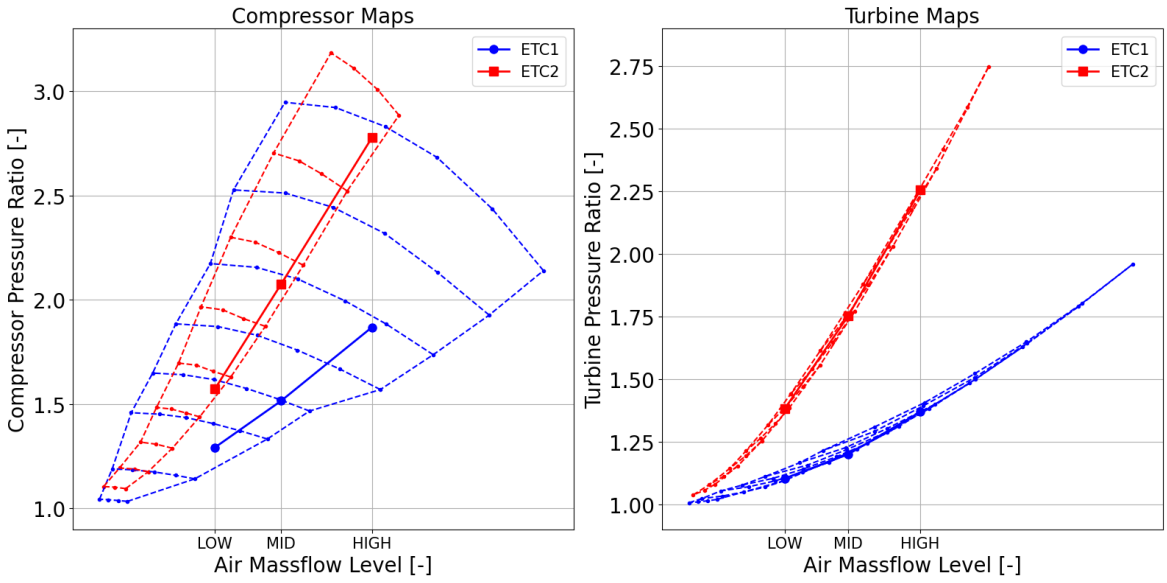

Figure 4.13: Compressor and Turbine Maps with Operating Conditions, Same Fuel Usage as Baseline

For ETC1, the solid blue line connecting the 50, 70 and 97kW operating points is located in the lower end of the map, but still with a margin from the choke line. If for the same massflows, the system pressure would be raised (i.e. the compression ratio), the operating line would move up to the central, more efficient region which could potentially yield even more performance. This could be tested by means of installing a backpressure valve downstream of the turbine outlet. After that, the next thing that would become limiting is the system pressure drop between compressor outlet and turbine inlet: the bigger this pressure drop, the more the operating line moves to the surge region where efficiency drops again.

For ETC2 however, the operating line lies much closer to the choke limit, and the 97kW point is located close to the maximum speed line. This confirms that ETC2 was sized to be more optimal for lower-power fuel cell systems, and hints to why its performance is less than expected: near the choke line, the efficiency of the compressor usually drops rapidly. This in turn will lead to higher inverter power consumption. Using a backpressure valve behind the turbine to increase system pressure and move the solid red line more towards the efficient region of the ETC2 compressor could perhaps increase performance. However, the component size is still a problem because moving the 97kW point upwards does not increase efficiency much due to its proximity to the maximum speed region.

Directly comparing ETC1 and ETC2 in terms of compressor stage, turbine stage and compression system efficiencies (η_c, η_t and $\eta_{c,sys}$ respectively), Table C.5 in Appendix C shows the numbers for these specific simulations. At the 50kW level, all three efficiencies were measured to be highest for ETC2. This contradicts the results shown earlier, which can be explained due to the influence of heat tranfser, especially at lower massflows such as corresponding to 50kW, overestimating the efficiencies. These efficiencies were therefore considered unsuitable to build conclusions on. At the 70 and 97kW levels, η_c and η_t were higher for ETC1 which is more in line with the earlier obtained results.

Looking at the values for $\eta_{c,sys}$, they were higher for ETC2 at 50 and 70kW, which again seems strange, but at 97 kW ETC1 performed better. It is clear that the efficiencies do not show completely why the results are the way they are. To find better conclusions, the data had to be considered from a different angle.

With that in mind, the increase in stack power output due to increase in system pressure as well as the change in inverter power consumption as function of the compressor pressure ratio could shed more light on the performance difference of both ETCs. This is visualized in Figure 4.14 (uncensored version: Figure C.3).

In the left graph, one can see the change in stack power w.r.t. air inlet pressure. The grey dashed lines are so-called 'iso-amps': lines where the current pulled from the stack is the same. Since the current and the air massflow are directly related, these iso-amps are also lines of constant air massflow (assuming constant air stoichiometry). Each of the three system configurations has one operating point on every iso-amp, as the simulations are performed at constant fuel consumption for each of the three power levels. Thus, in total, there are three iso-amps on the graph, corresponding to the 50, 70 and 97kW power levels. Looking at each iso-amp, the increase in stack power due to increase in stack air inlet pressure can be seen for all three power levels.

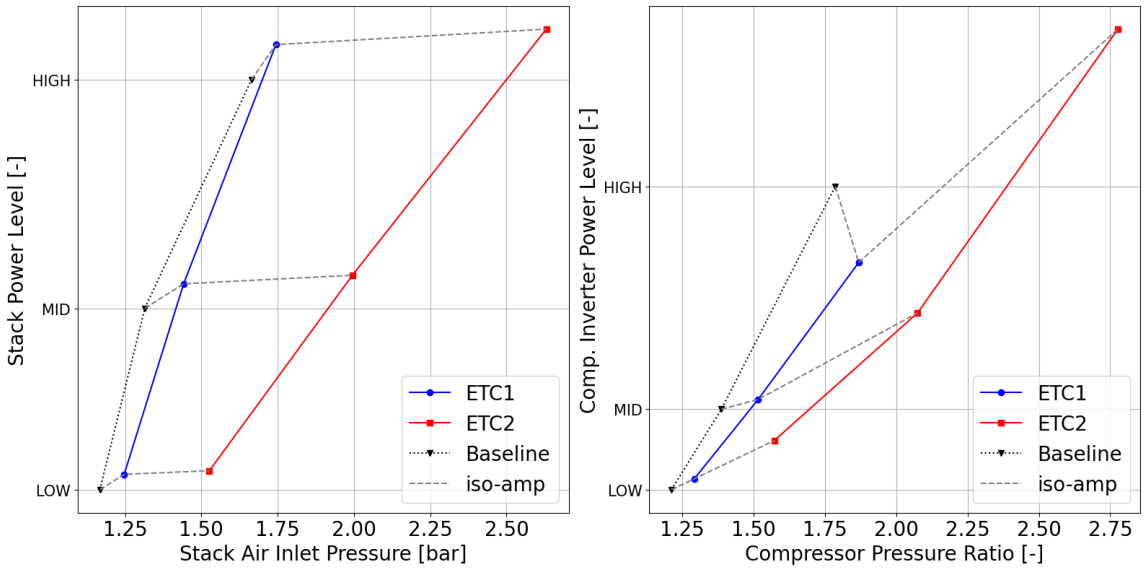

Figure 4.14: Graphs Showing the Variation in Stack Output Power and Inverter Power Consumption With Changing System Pressure Levels

From theory, as shown in Equation 3.20, increasing the stack air pressure yields a logarithmic increase in the stack voltage. The same is seen in this graph, as the iso-amps follow a logarithmic shape. A logarithmic relationship essentially represents diminishing returns on investment. In this case, the investment is the increased air pressure (using inverter power) and the return is the added stack power (due to voltage increase at constant current).

If one looks at the highest iso-amp in the left graph, the following conclusions can be made:

- The baseline stack power is lowest (97kW), the ETC1 stack power is higher than that and the ETC2 stack power is the highest
- The baseline stack air inlet pressure is around 1.66bar, the ETC1 stack air inlet pressure is 1.74bar and for ETC2 it is 2.63bar
- The iso-amp slope between the baseline and ETC1 point is steeper than the slope between the ETC1 and ETC2 point (holds for all iso-amps)

Although the ETC2 system produces more stack power than the ETC1 sytem, it requires a much higher air pressure to do so, which costs compressor inverter power. To see the dependence of this inverter power with air pressure increase, the right graph of Figure 4.14 is shown. This plot shows, for the same iso-amps, the change in compressor inverter input power w.r.t. the needed pressure ratio. The following can be noted here:

- For the lower two iso-amps, the compressor inverter power consumption for ETC1 and ETC2 is larger than for the baseline

- For the highest iso-amp, the ETC1 inverter power consumption is lower than that of the baseline system: ETC1 thus directly saves electrical power thanks to its turbine
- For the highest iso-amp, the ETC2 inverter power consumption is much higher than both ETC1 and the baseline: this is the cost of the 2.63bar of stack air inlet pressure

Regarding ETC1, at the 50 and 70kW levels its turbine has not spooled up yet, but at 97kW it has and clearly recuperates energy by saving about 2kW of inverter power consumption, leading to a significant increase in system efficiency. ETC2 however never consumes less compressor inverter power than the baseline, not even at the lower power levels. The reason for this could be that ETC2 is operating close to choked conditions, as shown in Figure 4.13, where it is known the efficiencies decrease strongly.

The above results could also be visualized in a more relative way. At the stack operating pressures ($p_{fc,i}$) of botch turbocharged systems, there is an increase in stack power compared to the baseline (dP_{fc}), and their ratio is a turbocharger-specific performance indicator: $\frac{dP_{fc}}{p_{fc,i}}$. The same can be done for the change in inverter power: $\frac{dP_{inv}}{p_{fc,i}}$. These performance indicators are denoted as the 'stack pressure sensitivity' and 'compressor inverter pressure sensitivity', respectively, and are visualized below in Figure 4.15 (uncensored version: Figure C.4).

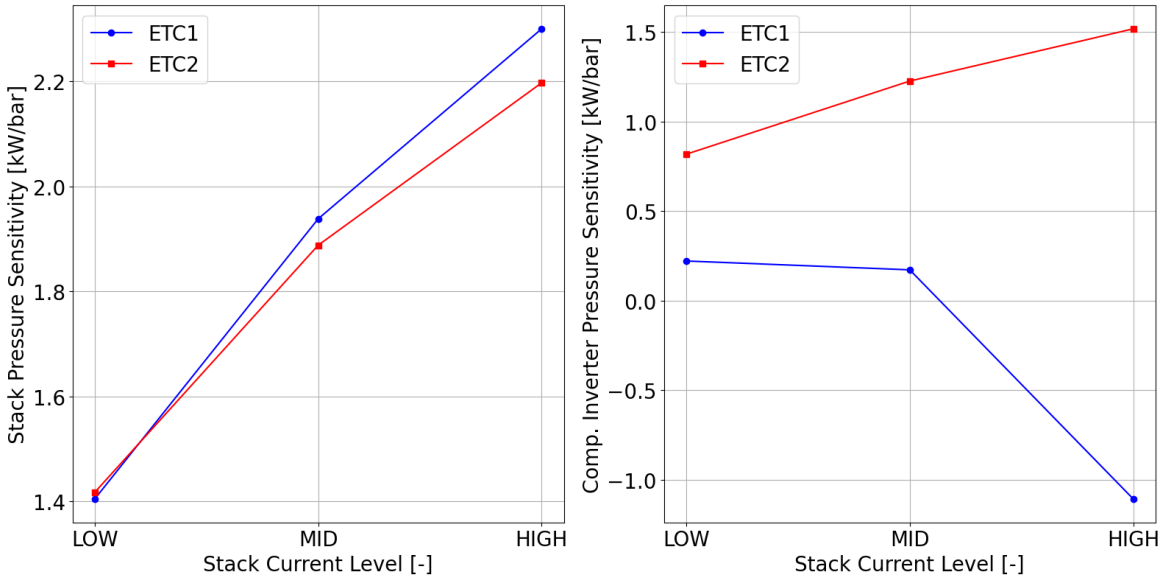

Figure 4.15: Stack Pressure Sensitivity and Compressor Inverter Pressure Sensitivity as a Function of the Stack Current

Looking at the left graph, one can see that the ETC1 system is more effective in creating extra stack power, only at the lowest current does ETC2 seem to have a slight advantage. But considering the right graph, it is seen that ETC1 is much more effective in creating boost pressures efficiently. The ETC1 inverter needs increasingly less power relative to the

pressure increase, showing it is a good fit in this specific air processing system, with the turbine really 'spooling up' at higher air flows (i.e. currents). ETC2 however struggles to leverage its turbine and needs increasingly more inverter power as the air flow and system pressure increases, which again corresponds well to expected behavior at choking conditions.

The shown sensitivities can be combined to show the overall benefit of using these specific E-turbochargers in this system. Incorporating an E-turbocharger means integrating a turbine that causes backpressure on the system, which is good for the stack but costly for the compressor. A performance index that quantifies the net benefit of integrating a specific E-turbocharger could be defined as $\frac{dP_{net}}{p_{fc,i}}$: how much extra net power is gained by increasing the stack inlet pressure to a certain level as a result of integrating a turbine? This performance index can be computed by:

$$\frac{dP_{net}}{p_{fc,i}} = \frac{dP_{fc}}{p_{fc,i}} - \frac{dP_{inv}}{p_{fc,i}} = \frac{dP_{fc} - dP_{inv}}{p_{fc,i}} \tag{4.2}$$

The value of this performance index is tabulated for both ETC1 and ETC2 for all three power levels:

Table 4.5: Overview of The Performance Indicators of both ETC1 and ETC2 Systems

Level	$\frac{\mathbf{dP_{fc}}}{\mathbf{p_{fc,i}}}$ ETC1	$\frac{\mathbf{dP_{fc}}}{\mathbf{p_{fc,i}}}$ ETC2	$\frac{\mathbf{dP_{inv}}}{\mathbf{p_{fc,i}}}$ ETC1	$\frac{\mathbf{dP_{inv}}}{\mathbf{p_{fc,i}}}$ ETC2	$\frac{\mathbf{dP_{net}}}{\mathbf{p_{fc,i}}}$ ETC1	$\frac{\mathbf{dP_{net}}}{\mathbf{p_{fc,i}}}$ ETC2
50 kW	1.405	1.418	0.221	0.818	1.184	0.600
70 kW	1.938	1.888	0.172	1.227	1.766	0.661
97 kW	2.300	2.197	-1.108	1.519	3.408	0.678

Looking at the final two columns, the net performance benefit of both E-turbochagers in this specific air processing system is seen. Nicely corresponding with the initial results from Figure 4.12, it is clear that ETC1 is the better fit for this specific system, and it is also confirmed that ETC2 still has a net benefit for all three power levels (despite the high compressor inverter power consumption). The above results provided good insights on why the net power boost performance is the way it is. The next step is to quantify the fuel consumption saving (running same net powers). This is done in the following subsection.

4.3.3 Comparing the Baseline, ETC1 and ETC2 Model at Same Net Power

In this subsection, the fuel savings when turbocharging are quantified. For the subsequent results, simulation runs 4-5-6 (baseline), 7-17-27 (ETC1) and 37-39-41 (ETC2) were used. The fuel consumption savings are shown in Figure 4.16 (uncensored: Figure C.5). Keeping in mind the values of the performance indices of both ETC1 and ETC2 from Table 4.5, the results make sense. The ETC1 system yields the best fuel consumption savings: 3.19, 4.27 and 7.67% respectively, and the ETC2 system yields 2.07, 2.41 and 3.17% which shows a more marginal increase over the power range. Figure 4.17 shows these operating points on the compressor and turbine maps once again (uncensored version: Figure C.6).

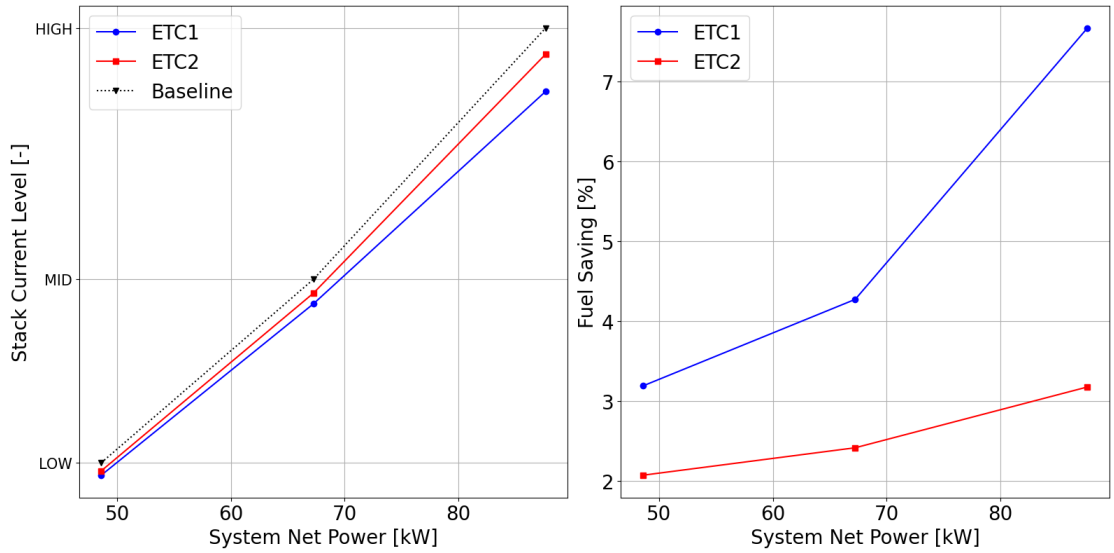

Figure 4.16: Stack Current for the Baseline and Turbocharged Models, Same Net Power Levels

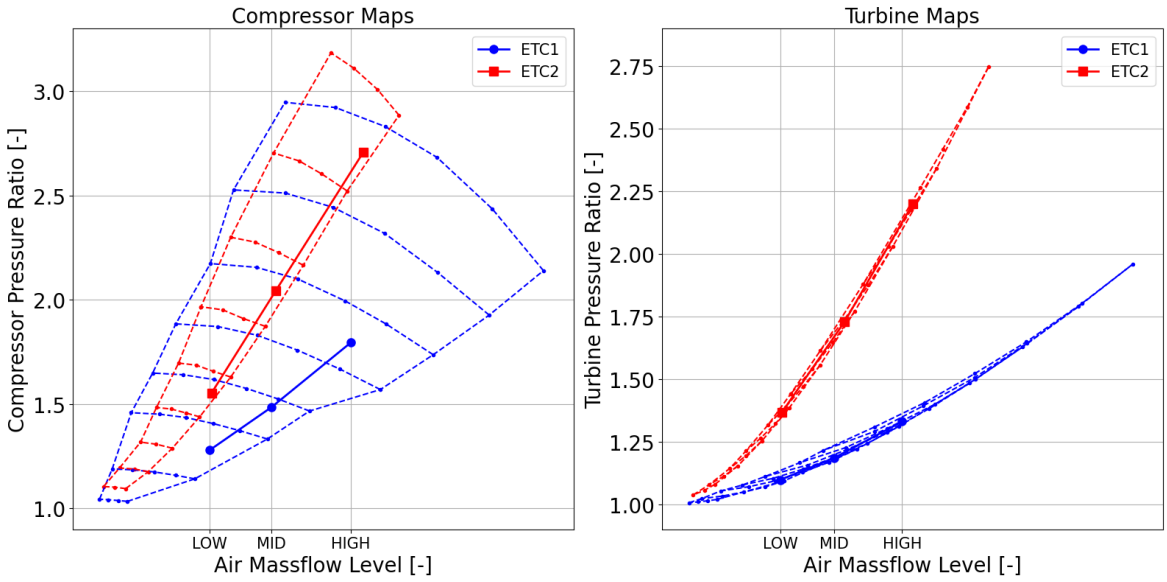

Figure 4.17: Compressor and Turbine Maps with Operating Conditions, Same Net Power Levels

This time, ETC1 is running on lower air massflow (lower current) than ETC2 which makes sense as the fuel savings were higher for ETC1. Both ETCs still experience operation in the same region as compared to the simulations shown in Figure 4.13: ETC1 in the lower end with a good margin to the choke line, but ETC2 operating near choking conditions.

Again, the corresponding efficiencies η_c, η_t and $\eta_{c,sys}$ for both turbocharger systems were also quantified and are shown in Table C.6 of Appendix C. Qualitatively speaking they show the

exact same story as already told in the previous subsection regarding the same-fuel usage simulations. The 50kW efficiencies are unreliably high (due to the heat transfer), the 97kW efficiencies are all higher for ETC1 and for 70kW, ETC2 has a higher $\eta_{c,sys}$ but lower individual turbine and compressor stage efficiencies. Quantitatively speaking, these efficiencies are in a very similar range compared to the values from the same-fuel usage simulations.

The final graph in this subsection, namely Figure 4.18, shows some more insights into the performance of the turbine stage specifically.

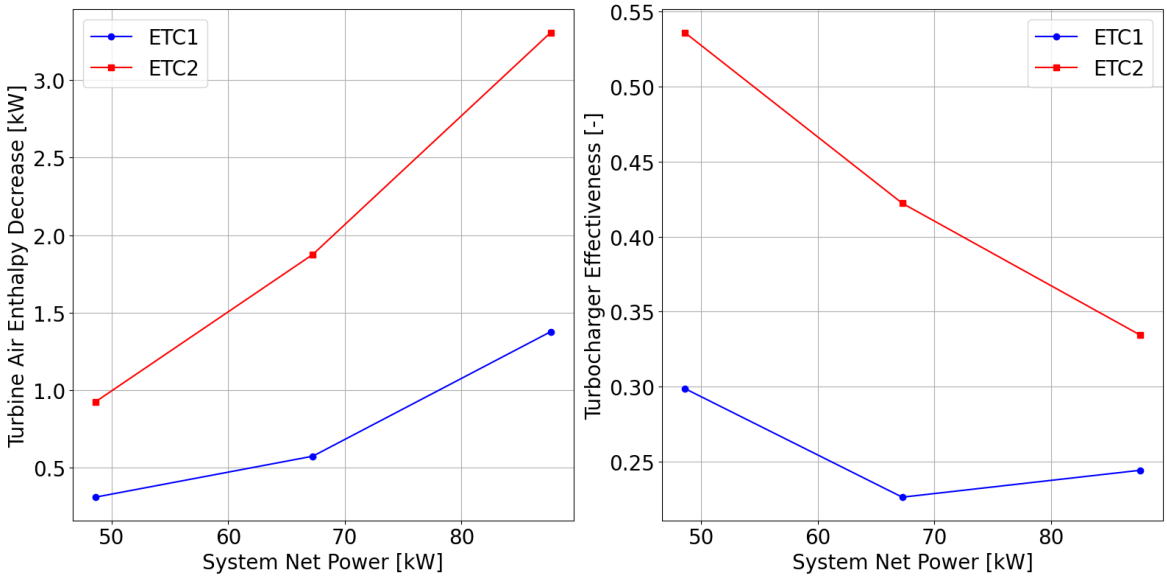

Figure 4.18: ETC1 and ETC2 Turbine Air Enthalpy Decrease and Effectiveness, Same Net Powers

In the left graph, the turbine air enthalpy decrease, defined as $\Delta H_{a,t} = \dot{m}_{a,t} \cdot Cp_a \cdot \Delta T_{a,t}$ is shown in function of the net power output of the system. This is a measure of how much energy input the turbine gets from the exhaust air. As expected, the ETC2 turbine recuperates significantly more exhaust power than ETC1 due to the size difference.

On the right plot, the turbocharger effectiveness is shown. This is defined as: $\Delta H_{a,t}/\Delta H_{a,c}$, or in other words: how much of the necessary compression energy has been recovered by the turbine. The results show that the turbocharger effectiveness for ETC2 is greater than for ETC1 over the whole power range. In the low and medium power range, the ETC2 turbine is nearly twice as effective.

4.3.4 Summary of Baseline vs ETC1 vs ETC2 Results

The main takeaways of the above discussion on comparing the baseline, ETC1 and ETC2 models are listed below.

- ETC2 operates the system at significantly higher pressures than ETC1 due to the smaller turbine on ETC2 (Figures 4.9, 4.10 and 4.11)
- Therefore, ETC2 yields more stack gross power (higher pressure = higher voltage) compared to ETC1 for all power levels (Figure 4.14 left graph)
- The turbine of ETC2 recovers more air power than the one of ETC1 for each power level, again due to its smaller size and thus higher expansion ratio (Figure 4.18)
- The compressor inverter power consumption is however also higher for ETC2 than for ETC1 over the whole power range, due to the higher needed compression ratio (Figure 4.14 right graph)
- Since for ETC2 the system operates near the choke line, the compression system suffers from lower efficiencies compared to ETC1 (Figures 4.13 and 4.17)
- In terms of overall benefit then, ETC1 outperforms ETC2 by producing more net system power at the same fuel consumption or consuming less fuel at same net power (Figures 4.12 and 4.16 respectively)

In addition, Table 4.6 summarizes the quantified performance gain of both ETC1 and ETC2 models compared to the baseline.

Table 4.6: Overview of The Performance Gains for Both E-turbocharger Prototypes

Level	ETC1		ETC2	
	Power Boost [%]	**Fuel Saving [%]**	**Power Boost [%]**	**Fuel Saving [%]**
50kW	3.04	3.19	1.88	2.07
70kW	3.79	4.27	1.96	2.41
97kW	6.78	7.67	2.04	3.17

4.4 Increased Turbine Inlet Temperature Simulations with ETC1

The previous section showed the potential performance gain for a PEM fuel cell system when swapping out the E-compressor for an E-turbocharger. If one zooms out to a bigger perspective, and considers a PEM fuel cell system applied in a vehicle as part of the powertrain, a next step can be done to increase performance even more. More specifically, waste heat from other sources in the vehicle could be directed to the fuel cell exhaust stream, heating up the temperature of the air before it enters the turbine. In theory, that should increase energy recuperation at the turbine, lower the inverter power consumption and thus increase the system performance further. The simulation runs considered in this part are runs 7 to 36. Now all simulation runs from Table 4.1 have been utilized for visualization.

Firstly, the impact of increasing turbine inlet temperature on fuel saving compared to the baseline fuel consumption is depicted in Figure 4.19 (uncensored version: Figure C.7). This

was done by comparing the runs that were performed at same net power output as the baseline reference. The LOW, MID and HIGH lines on the y-axis show the original stack current level of the baseline model without exhaust turbine.

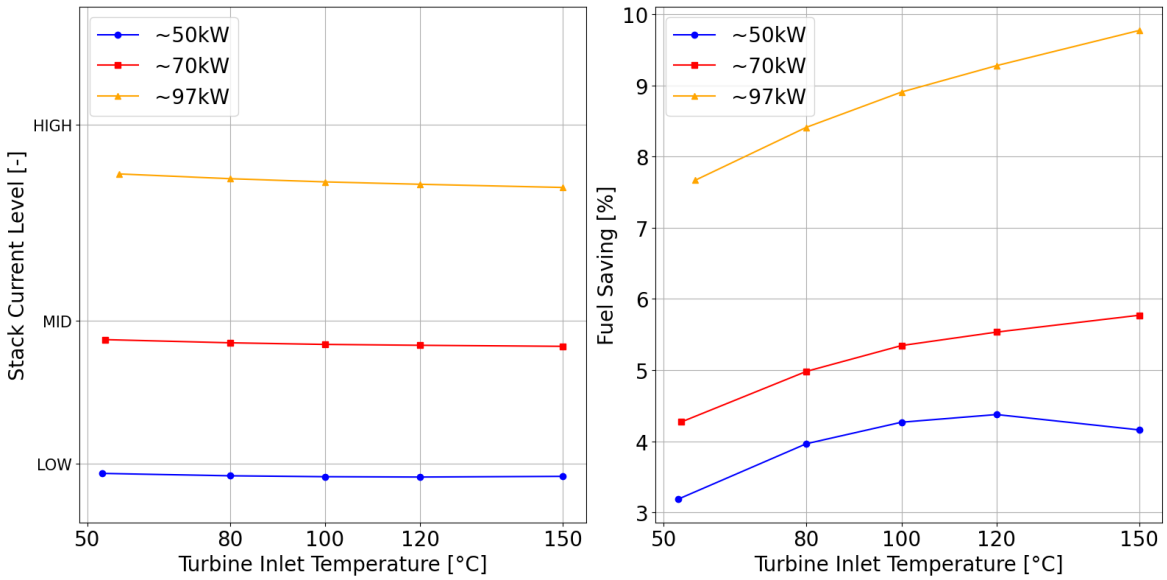

Figure 4.19: Change in Fuel Consumption as a Function of TIT for Various Power Levels

On the left side, one can see the resulting stack current levels compared to the baseline reference runs, but now as a function of turbine inlet temperature (TIT). The necessary current seems to decrease with increasing TIT, showing that at least there is a benefit when dumping more waste heat into the exhaust. The trend, however, seems to be sublinear, indicating again a diminishing return on investment. The same trend can be seen for the right plot, showing the savings in fuel consumption.

The added thermal management equipment that would need to be installed in order to obtain an increased TIT brings extra weight and costs, and those additions have to be justified by a sufficient increase in performance. These plots could help make that decision, as the benefit (fuel savings) is quantified in terms of the cost (increasing TIT).

One noteworthy thing here is that for the 50 kW power level, the fuel consumption seems to increase again from 120°C TIT to 150°C TIT, which should not be the case. Upon investigation, it was found that the reason for this numerical behavior is the lack of measurement data points in this area of high TIT and low air massflow (current). The interpolation therefore makes an inaccurate estimation of the reduction in inverter power and the error propagates into the fuel saving calculation. In reality, the fuel saving should increase from 120°C TIT to 150°C TIT.

The following figure shows the increase in net power when the turbocharged system is run with the same fuel consumption as the baseline reference.

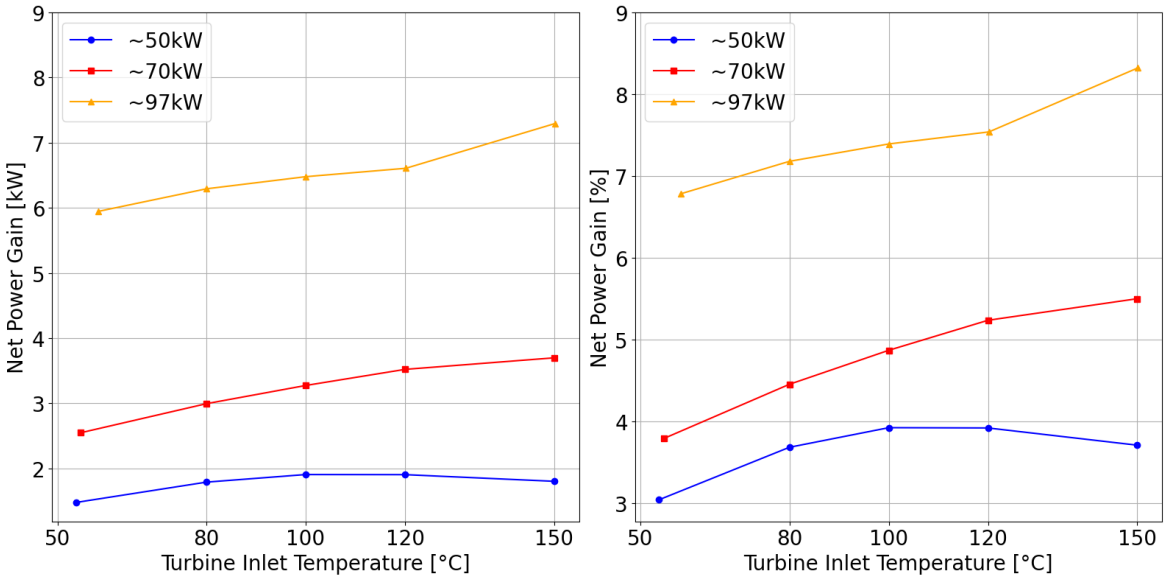

Figure 4.20: Change in Net Power Output as a Function of TIT for Various Power Levels

What can be seen now is that the net power increases with increasing TIT. The 70kW line acts as expected, with a diminishing return on investment once again. At 150°C TIT, the extra net power gained compared to the baseline 70kW net power equals 3.7kW. For the 50kW, the same behavior is seen as before, with an unnatural drop in net power gain due to a poor interpolation estimate. Interestingly enough, now also the 97kW line shows unrealistic behaviour from 120°C TIT to 150°C TIT.

This behaviour has been investigated, and it turned out that this was due to the high air massflow (the target air massflow is highest in this simulation: maximum power and same current as baseline). At this air massflow, the simulation was not perfectly stable making the air massflows through the components fluctuate around a certain mean. The result was that the massflow going through the turbine was too high, overestimating the turbine power, therefore underestimating the inverter power and in turn overestimating the net power.

The most reliable result here is therefore the 70kW line, and it can be seen that about 5.50% of extra net power can be gained at 150°C TIT compared to the baseline reference. For the naturally occuring TIT (54.7°C), the net power increases by 3.79%. Therefore, when heating up the turbine inlet air from 54.7°C to 150°C (increase of almost 95°C) yields an extra net power increase of 1.71%. These figures might help make decisions on what a feasible target TIT would be in a real vehicle application considering added weight and costs of the necessary extra heat exhanger(s).

Now that the full system response to increasing TIT has been quantified, it is time to dive into the component level to see what is going on there. Figure 4.21 shows the influence on compressor inverter power consumption.

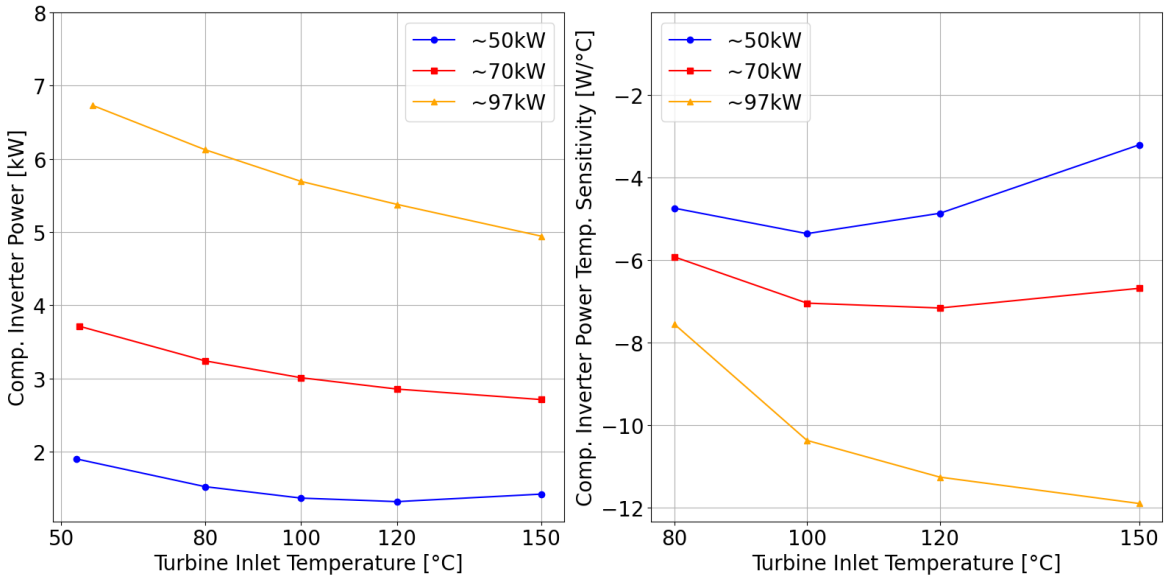

Figure 4.21: Change in Inverter Performance as a Function of TIT for Various Power Levels

The left side shows how the inverter power drops in function of the TIT. Again for the 50kW line, the unnatural behavior is seen. The reason for this is the same as for the previous plots. But for the 70kW and 97kW (in this case there were no massflow instabilities in the simulation) lines, the behavior seems good. Once again the diminishing returns on investment is noticed.

For the right plot, the sensitivity of inverter power consumption w.r.t. the TIT level is shown, which is a similar parameter as shown previously in Figure 4.15 and Table 4.5. This time, its definition is $\frac{dP_{inv}}{TIT}$: by how much does the inverter power change (decrease) at a certain increased TIT? Since the basis for generating this sensitivity is the data from the left graph, the 50kW blue line does not show realistic behavior, but the 70kW and 97kW lines do.

The 70kW line in the right side of figure 4.21 shows that from 120°C TIT onwards, the magnitude of the sensititvity decreases again after reaching a minimum. This is somewhat misleading as on the left plot it is seen that there should still be a benefit. This is purely a result of the definition of $\frac{dP_{inv}}{TIT}$. In order to obtain the change in inverter power at TIT=150°C for the 70kW power level, one simply has to multiply the corresponding sensitivity, in this case -6.68W/°C, with 150°C to obtain dP_{inv} = -1kW, which is still a larger reduction compared to dP_{inv} for the 120°C TIT at 70kW.

The very final graph, Figure 4.22 zooms in on what happens at the turbine.

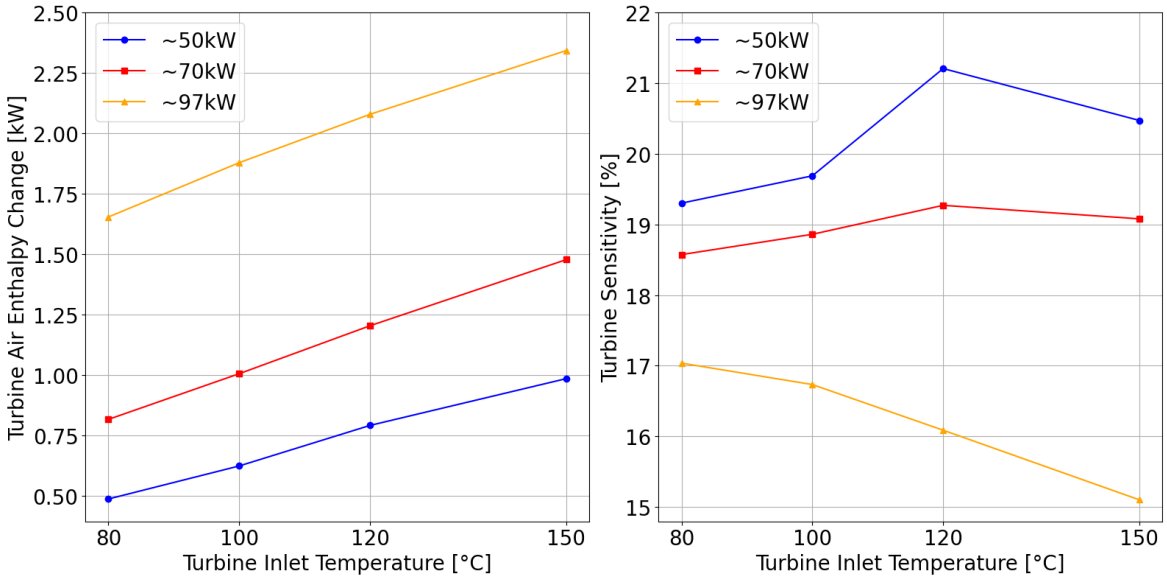

Figure 4.22: Change in Turbine Performance as a Function of TIT for Various Power Levels

As can be seen on the left plot, the increase in turbine air enthalpy change scales linearly with the TIT, which is in line with what the theory predicts (enthalpy change depends linearly on the inlet temperature). The more interesting thing to see is in the right graph. There, a turbine sensitivity σ_t is formulated and shown in function of the TIT. The way it is defined can be best thought of as this: For every kW of waste heat going in to the turbine inlet air, how much does the turbine recover? Or as a formula:

$$\sigma_t = \frac{d(\Delta H_{a,t})}{\dot{Q}_{in}} = \frac{(TIT - TOT) - (TIT_{ref} - TOT_{ref})}{(TIT - TIT_{ref})} \cdot 100\% \tag{4.3}$$

where TIT_{ref} and TOT_{ref} are the reference TIT and turbine outlet temperature when the exhaust air is not externally heated, respectively. TOT is the turbine outlet temperature corresponding to the increased TIT that occurs when adding waste heat $\dot{Q}_{in}$.

The values for TIT_{ref} and TOT_{ref} come from simulation runs 7 (50kW level), 17 (70kW level) and 27 (97kW level). Looking at the graph, what is clear is that the turbine sensitivity decreases with increasing power level and therefore air massflow. Looking at a (almost) constant air massflow, the relationship with varying TIT seems to be nonlinear, but at ever increasing TITs, the sensitivity does seem to go down, indicating once more the diminishing returns.

Chapter 5

Conclusions and Recommendations

The aim of this research was to investigate waste heat recovery (WHR) solutions for low-temperature PEM fuel cells for automotive applications such as turbocharging as a means of increasing the performance of the powertrain, by developing models of novel fuel cell air processing system concepts and carrying out simulations to quantify their potential performance gains against a benchmark. Four specific research questions (RQ) were posed in Section 1.2. The corresponding answers are now provided with essential information that was garnered during the research. Furthermore, recommendations for future work regarding the topic of turbocharged fuel cell air processing systems are also formulated.

5.1 Answers to the Research Questions

RQ1: What are potential methods of increasing the efficiency of a hydrogen PEM fuel cell system by means of waste heat recovery?

The literature study in Chapter 2 and the simplified analysis of the heat pump concept in Section B.1 made it possible to answer this research question. The four investigated WHR solutions were turbocharging with exhaust gas, the Organic Rankine Cycle (ORC), Vapour Compression and Absorption Cycles (VCC & VAC), and thermo-electric generators (TEGs). The conclusions regarding their feasibility are listed below:

1. Turbocharging with exhaust gas: This WHR solution features a high technology readiness level from being widely applied in internal combustion engines (ICE) as well as high efficiency ($\sim$70%) and power density compared to other solutions. Therefore, turbocharging hydrogen PEM fuel cell air processing systems is at this time the most suitable solution for increasing system efficiency in automotive applications.
2. ORC power systems: This solution has shown certain benefits for ICE applications, but due to complexity and cost barriers never made it to mass production. For PEM

fuel cell systems specifically, this solution proved to have insufficient performance due to very low cycle efficiencies (∼6%) at the low operating temperatures (∼70°C) of a fuel cell electric vehicle that did not justify the added complexity, weight and costs. In the future, granted developments for ORC systems are made and high-temperature fuel cells (∼160°C) are commercially available, the ORC power system could become a feasible WHR solution.

3. VCC systems: Also known as heat pumps, they are widely used for air conditioning applications in the automotive industry. In this research, the question was if a high-temperature heat pump could be used to heat up the fuel cell stack exhaust air before entering the turbine of the E-turbocharger, potentially yielding a benefit on the system level. It was concluded that in none of the simulated conditions, did the heat pump show any benefit in terms of net power boost or fuel savings.
4. VAC & TEG systems: These solutions feature very low efficiencies (∼5%), bulky dimensions and high costs. Therefore, although they might be used in certain industrial applications, they are not wide-spread in the automotive industry, and were also not considered as a viable option for an automotive PEM fuel cell system.

The performed simulations of an existing non-turbocharged baseline PEM fuel cell system in addition to its conceptual turbocharged variant allowed for answering RQs 2, 3 and 4. The specifications of two different E-turbochargers (ETCs) were used to set up models for two different turbocharged air processing systems. One ETC featuring a bigger turbine diameter, was named ETC1, and the other one featuring a smaller turbine diameter, was named ETC2. Each model was simulated at the same three stack power output levels of around 50kW, 70kW and 97kW. RQs 2-4 and their corresponding answers are given below.

RQ2: By how much does the efficiency of an automotive hydrogen PEM fuel cell system increase when its electrical air compressor is replaced by an electrical turbocharger that harvests power from the fuel cell exhaust stream?

In terms of extra net power and fuel saving, both turbochargers showed a positive impact across all three simulated power levels. The model featuring ETC1 achieved an increase in net power between 3.04-6.78% at same fuel consumption corresponding to 50-97kW stack power of the baseline model, and a decrease in fuel consumption between 3.19-7.67% when producing the same system net power as the baseline model. For the ETC2-based model, the net power at same fuel consumption as the baseline increased between 1.88-2.04%, and for same net system power, the fuel consumption decreased between 2.07-3.17%.

Although ETC2 features the smaller turbine and was initially expected to recover more energy at low system loads (the 50kW level) compared to ETC1, it turned out to not be the case, as shown in the percentages in the paragraph above. The cause for this is two-fold. Firstly, due to the characteristics of this specific fuel cell system, ETC2 operates very close to its choke line for all three power levels. This is a region where the efficiency of both the turbine and compressor wheels decreases strongly. Secondly, the high turbine inlet pressure caused by the smaller turbine wheel of ETC2 leads to a very high compressor pressure ratio that needs to be compensated by much more compressor inverter power. The combined effect is therefore a lower gain in system efficiency compared to when using ETC1.

RQ3: By how much does the efficiency of the turbocharged fuel cell system increase when a specific amount of waste heat from another source is added to the exhaust stream, thus increasing turbine inlet temperatures?

To answer RQ3, the ETC1-based turbocharged model was simulated with air turbine inlet temperatures (TITs) ranging from ∼60°C up to 150°C, since measurement data in these operational conditions was available. Increasing the TIT, which could hypothetically be done by using a heat exchanger between the turbine inlet air and a liquid carrying waste heat, showed to be beneficial in terms of boost power and fuel saving. However, the effect seemed to show 'diminishing returns on investment', meaning the respective increases in performance became smaller and smaller with every increase in TIT. There is thus a certain point where the necessary added thermal management equipment in the vehicle introduces more drawbacks in terms of cost and weight than can be justified by the only marginal performance gain.

In numbers: at the highest power level (∼97kW), where ∼160°C waste heat could be present in a commercial PEM fuel cell vehicle, the fuel consumption at TIT=150°C compared to the standard TIT (between 50-60°C) decreased with 2.1 percentage points. At the medium power level (∼70kW) and TIT=150°C, the net power output increased with 1.71 percentage points compared to operation with the standard TIT.

RQ4: In which circumstances could the addition of a pressure regulation valve be beneficial for the working of the aforementioned turbocharged fuel cell system?

When the E-turbocharger in the air processing system is operating in the lower region of its compressor map, it could be beneficial to install a pressure regulation valve after the turbine outlet. Upon restricting the flow using this valve, the system pressure rises, which in turn raises the compression ratio and moves the operating points more to the central region of the map. There, due to increased compressor efficiency, the complete system efficiency is expected to increase further.

In the opposite situation where the E-turbocharger would operate near the surge line, implying too high compression ratios, integrating a pressure regulation valve anywhere in the system would not help. The limiting factor here would be the excessive system pressure drop between compressor outlet and turbine inlet: if it could be reduced, then for the same air massflow and turbine backpressure, the compressor pressure ratio would reduce and the operating points would move away from the surge line. This implies changing designs of components.

5.2 Recommendations

5.2.1 Possible Model Improvements

The biggest weakness in the simulation model is how the air temperature change in the E-compressor and E-turbocharger, which have influence on overall accuracy, has been implemented. Due to the many pathways heat can flow from and to the air in the compressor and

turbine stages, and not enough information being available to quantify them all, a rough approach had to be taken. Instead of an energy balance-based method, a 2-dimensional dataset interpolation method has been used to compute the change in air temperature over the compressor and turbine, as well as to compute the change in necessary compressor inverter power. The exact values of these datasets depend heavily on the conditions in which they are generated. This makes the model dependent on its input data, and therefore less accurate when varying the simulated operational conditions away from the measurement range of the data.

For an improved model, these calculations can be made more accurate if more information is available that would facilitate the setup of an energy balance-based method. This could make the model more robust for a wider range of simulated operational conditions. However, this extra information needs to be provided from specific types of test setups, which is discussed in the next subsection.

5.2.2 Further Investigations

As just mentioned, the biggest challenge in this research was dealing with the unknowns regarding heat transfer. A potential further investigation could consist of building a framework for an efficiency definition specifically for liquid-cooled E-turbochargers where heat transfer is significant, since the conventional isentropic compressor/turbine efficiencies do not provide good accuracies in this case.

Specific test procedures could be formulated to be able to measure additional parameters yielding more information on all the various heat flows. Separately identifying the heat transfer between the compressing/expanding air and the E-motor coolant, as well as heat transfer due to natural convection, radiation and conduction through casings would provide this necessary information. This would allow energy balance-based calculations in a simulation and therefore more accurate results over a wide range of input conditions.

A more tangible further investigation is to use the current simulation model to investigate if ETC1 would perform even better if higher backpressure was applied at the turbine outlet, raising the system operation points to the central part of the compressor map where efficiencies are higher, compared to the lower end where the operating points are currently located.

Finally, a more advanced option for continued simulation is to investigate the benefit of a variable turbine geometry (VTG) E-turbocharger. In ICE applications, this is a mass-produced and widely used component for increasing system efficiency over a wider range of power outputs. However, this is only possible on the condition that certain measurement data on a VTG E-turbocharger is provided, which at the time of writing this thesis was not available.

Bibliography

[1] L. Hoesung, J. Romero, and The Core Writing Team. *Climate Change 2023 Synthesis Report Summary for Policymakers*. IPCC, March 2023. doi: 10.59327/IPCC/AR6-9789291691647.001.

[2] College of the Desert. Module 3: Hydrogen use in internal combustion engines. Technical report, Deparment of Energy USA, 2001.

[3] J. Larminie and A. Dicks. *Fuel Cell Systems Explained*. John Wiley & Sons Ltd, second edition, 2003.

[4] F. Barbir. *PEM Fuel Cells: Theory and Practice*. Elsevier, second edition, 2013.

[5] M. Raghavan and Y. Sheng He. A comparison of automotive waste heat recovery systems. *Advances in Technology Innovation*, 3(4):195–205, January 2018.

[6] S. Martinez-Boggio, L. Di Blasio, et al. Optimization of the air loop system in a hydrogen fuel cell for vehicle application. *Energy Conversion and Management*, 283, March 2023. doi: https://doi.org/10.1016/j.enconman.2023.116911.

[7] T. Wittmann et al. On the impact of condensation and liquid water on the radial turbine of a fuel cell turbocharger. *Machines*, 10(11):1053–1074, November 2022.

[8] M.D. Neto et al. Numerical study on the formability of metallic bipolar plates for proton exchange membrane (pem) fuel cells. *Metals*, 9(7), July 2019. doi: https://doi.org/10.3390/met9070810.

[9] J. Cheng et al. Modeling and fuzzy feedforward control of fuel cell air supply system. *World Electric Vehicle Journal*, 12(4), October 2021. doi: https://doi.org/10.3390/wevj12040181.

[10] B. Blunier and A. Miraoui. Air management in pem fuel cells: State-of-the-art and prospectives. *IEEE*, pages 245–254, September 2007. doi: 10.1109/ACEMP.2007.4510510.

[11] Z. Zhengping et al. Polybenzimidazole-based polymer electrolyte membranes for high-temperature fuel cells: Current status and prospects. *Energies*, 14(135), December 2020. doi: https://doi.org/10.3390/en14010135.

[12] Garrett. Performance catalogue vol 9, July 2022.

[13] P. McTaggart. Development of a hybrid compressor/expander module for automotive fuel cell applications. Technical report, Department of Energy USA, 2004.

[14] D. Filsinger, G. Kuwata, and N. Ikeya. Tailored centrifugal turbomachinery for electric fuel cell turbocharger. *International Journal of Rotating Machinery*, September 2021. doi: https://doi.org/10.1155/2021/3972387.

[15] D. Filsinger, G. Kuwata, and N. Ikeya. Electric turbocharger for fuel cells - ihi´s contribution to sustainable mobility. *FC³ Fuel Cell Conference*, November 2021.

[16] Y. Zhang, S. Xu, and C. Lin. Performance improvement of fuel cell systems based on turbine design and supercharging system matching. *Applied Thermal Engineering*, 180, November 2020. doi: https://doi.org/10.1016/j.applthermaleng.2020.115806.

[17] A. Hansson and M. Abu Al-Shoud. Turbo for fuel cell electric vehicle. Technical report, Lund University, Faculty of Engineering, 2022.

[18] A. Kerviel, A. Pesyridis, and D. Chalet. Boosting system options for high efficiency fuel cell electric vehicles. Technical report, Brunel University, 2019.

[19] M. Menze, M. Schoedel, and J. R. Seume. Numerical investigation of a radial turbine with variable nozzle geometry for fuel cell systems in automotive applications. *Proceedings of 14th European Conference on Turbomachinery Fluid dynamics & Thermodynamics*, April 2021.

[20] C. Jiménez-Garcia José et al. A comprehensive review of organic rankine cycles. *Processes*, 11, June 2023. doi: https://doi.org/10.3390/pr11071982.

[21] F. Raab, H. Klein, and F. Opferkuch. Steam rankine cycle instead of organic rankine cycle for distributed waste heat recovery – pros and cons. *ORC Munich International Seminar*, October 2021.

[22] A. Pesyridis et al. *Automotive Exhaust Emissions and Energy Recovery*. Nova, 2014.

[23] R. Vescovo. High temperature organic rankine cycle (ht-orc) for cogeneration of steam and power. *AIP Conference Proceedings*, December 2019. doi: https://doi.org/10.1063/1.5138886.

[24] Y. Lu, A.P. Roskilly, and X. Yu. The development and application of organic rankine cycle for vehicle waste heat recovery. *IntechOpen*, 2018. doi: http://dx.doi.org/10.5772/intechopen.78401.

[25] Y. Abdellah Ayoub Laouid et al. Wet working fluids for regenerative orc with varying heat source temperature. *International Conference on Applied Energy*, August 2019.

[26] F. Alshammari et al. Expander technologies for automotive engine organic rankine cycle applications. *Energies*, 11(7), July 2018. doi: https://doi.org/10.3390/en11071905.

[27] J. Carlos Soldado et al. Axial turbo-expander design for organic rankine cycle waste-heat recovery with comparative heavy-duty diesel engine drive-cycle performance assessment. *Frontiers in Mechanical Engineering*, 7, June 2021. doi: 10.3389/fmech.2021.676566.

[28] J. Thaddeus et al. Design, size estimation, and thermodynamic analysis of realizable organic rankine cycle systems for waste heat recovery in commercial truck engines. *Thermal Science and Engineering Progress*, 22, May 2021. doi: https://doi.org/10.1016/j.tsep.2021.100849.

[29] R. Cipollone et al. Development of an organic rankine cycle system for exhaust energy recovery in internal combustion engines. *Journal of Physics*, 2015. doi: doi:10.1088/1742-6596/655/1/012015.

[30] J. Galindo. Experimental and thermodynamic analysis of a bottoming organic rankine cycle (orc) of gasoline engine using swash-plate expander. *Energy Conversion and Management*, 2015. doi: http://dx.doi.org/10.1016/j.enconman.2015.06.085.

[31] V. Dolz et al. Hd diesel engine equipped with a bottoming rankine cycle as a waste heat recovery system. part 1: Study and analysis of the waste heat energy. *Applied Thermal Engineering*, 2012. doi: http://dx.doi.org/10.1016/j.applthermaleng.2011.10.025.

[32] F. Alsouda et al. Vapor compression cycle: A state-of-the-art review on cycle improvements, water and other natural refrigerants. *Clean Technologies*, 5:584–608, May 2023. doi: https://doi.org/10.3390/cleantechnol5020030.

[33] M. Bentrcia, M. Alshatewi, and H. Omar. Developments of vapor-compression systems for vehicle air-conditioning: A review. *Advances in Mechanical Engineering*, 9(8), August 2017. doi: https://doi.org/10.1177/1687814017717186.

[34] L. Reinholdt et al. Heat pump cop, part 1: Generalized method for screening of system integration potentials. *Proceedings of the13th IIR-Gustav Lorentzen Conference on Natural Refrigerants*, 2:1097–1104, 2018. doi: https://doi.org/10.18462/iir.gl.2018.1380.

[35] A. Subiantoro, K. Tiow Ooi, and U. Stimming. Energy saving measures for automotive air conditioning (ac) system in the tropics. *International Refrigeration and Air Conditioning Conference*, 2014. URL http://docs.lib.purdue.edu/iracc/1361.

[36] C. Arpagaus et al. High temperature heat pumps: Market overview, state of the art, research status, refrigerants, and application potentials. *Energy*, 152:985–1010, March 2018. doi: https://doi.org/10.1016/j.energy.2018.03.166.

[37] R. Best and W. Rivera. A review of thermal cooling systems. *Applied Thermal Engineering*, 75:1162–1175, August 2014. URL http://dx.doi.org/10.1016/j.applthermaleng.2014.08.018.

[38] Z. Tan, X. Feng, and Y. Wang. Performance comparison of absorption heat pump and refrigeration in low temperature waste heat recovery. *Chemical Engineering Transactions*, 81:151–156, May 2020. doi: 10.3303/CET2081026.

[39] G. Vicatos, J. Gryzagoridis, and S. Wang. A car air-conditioning system based on an absorption refrigeration cycle using energy from exhaust gas of an internal combustion engine. *Journal of Energy in Southern Africa*, 19(4):6–11, November 2008. doi: 10.17159/2413-3051/2008/v19i4a3331.

[40] L. Jianbo et al. A novel absorption–compression combined refrigeration cycle activated by engine waste heat. *Energy Conversion and Management*, 205, December 2019. doi: https://doi.org/10.1016/j.enconman.2019.112420.

[41] Unknown author. The fundamentals of thermoelectrics a bachelor's laboratory practical. Technical report, LMU München, 2004.

[42] P. Nonthakarn et al. Design and optimization of an integrated turbo-generator and thermoelectric generator for vehicle exhaust electrical energy recovery. *Energies*, 12, August 2019. doi: 10.3390/en12163134.

[43] R. Rodriguez. Maximizing energy recovery in thermoelectric generator waste heat recovery systems for automotive applications. Technical report, University of California, Berkeley, USA, 2019.

[44] S. El Oualid et al. High power density thermoelectric generators with skutterudites. *Advanced Energy Materials*, 11(19), 2021. doi: 10.1002/aenm.202100580.

[45] R. Anant Kishore, M. Sanghadasa, and P. Shashank. Optimization of segmented thermoelectric generator using taguchi and anova techniques. *Scientific Reports (Nature)*, 7, December 2017. doi: https://doi.org/10.1038/s41598-017-16372-8.

[46] T. Nguyen Tien, Q. Khong Vu, and V. Nguyen Duy. Novel designs of thermoelectric generator for automotive waste heat recovery: A review. *Energy*, 10(4), August 2022. doi: 10.3934/energy.2022042.

[47] P. Bakker and B. van Leer. Lecture notes on gasdynamics, ae4-140. Technical report, Delft University of Technology, 2019.

[48] L.D. Rodriguez, J. M. Aftosmis, and M. Nemec. Formulation and implementation of inflow/outflow boundary conditions to simulate propulsive effects. Technical report, NASA, 2018.

[49] J.D. Anderson Jr. *Introduction to Flight*. McGraw-Hill, eighth edition, 2016.

[50] R.K. Shah and D.P. Sekulić. *Fundamentals of Heat Exchanger Design*. John Wiley & Sons, Inc., 2003.

[51] H. Peng. A thermodynamic model of membrane humidifiers for pem fuel cell humidification control. *Journal of Dynamic Systems Measurement and Control*, 127:424–432, September 2005. doi: 10.1115/1.1978910.

[52] POWDERPROCESS. Humid air : Specific heat capacity, 2024. URL https://powderprocess.net/Tools_html/Air/Air_Humid_Specific_Heat.html.

[53] S.L. Dixon and C. A Hall. *Fluid Mechanics and Thermodynamics of Turbomachinery*. Elsevier Inc., sixth edition, 2010.

[54] Association of German Engineers VDI Society for Process Engineering and Chemical Engineering. *VDI Heat Atlas*. Springer, second edition, 2010.

Appendix A

Additional Diagrams and Graphs

A.1 Schematic of the Full Turbocharged System Model

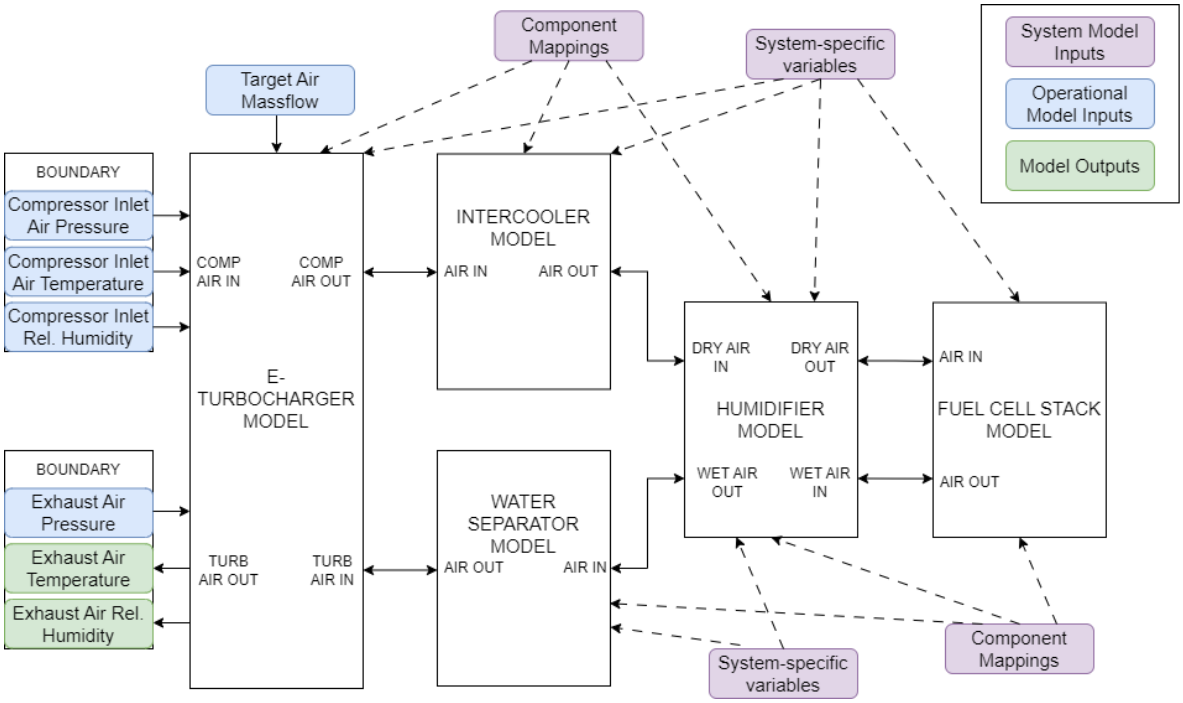

Figure A.1: Schematic of the Complete Turbocharged System Model

A.2 Schematic of the E-turbocharger Component Model

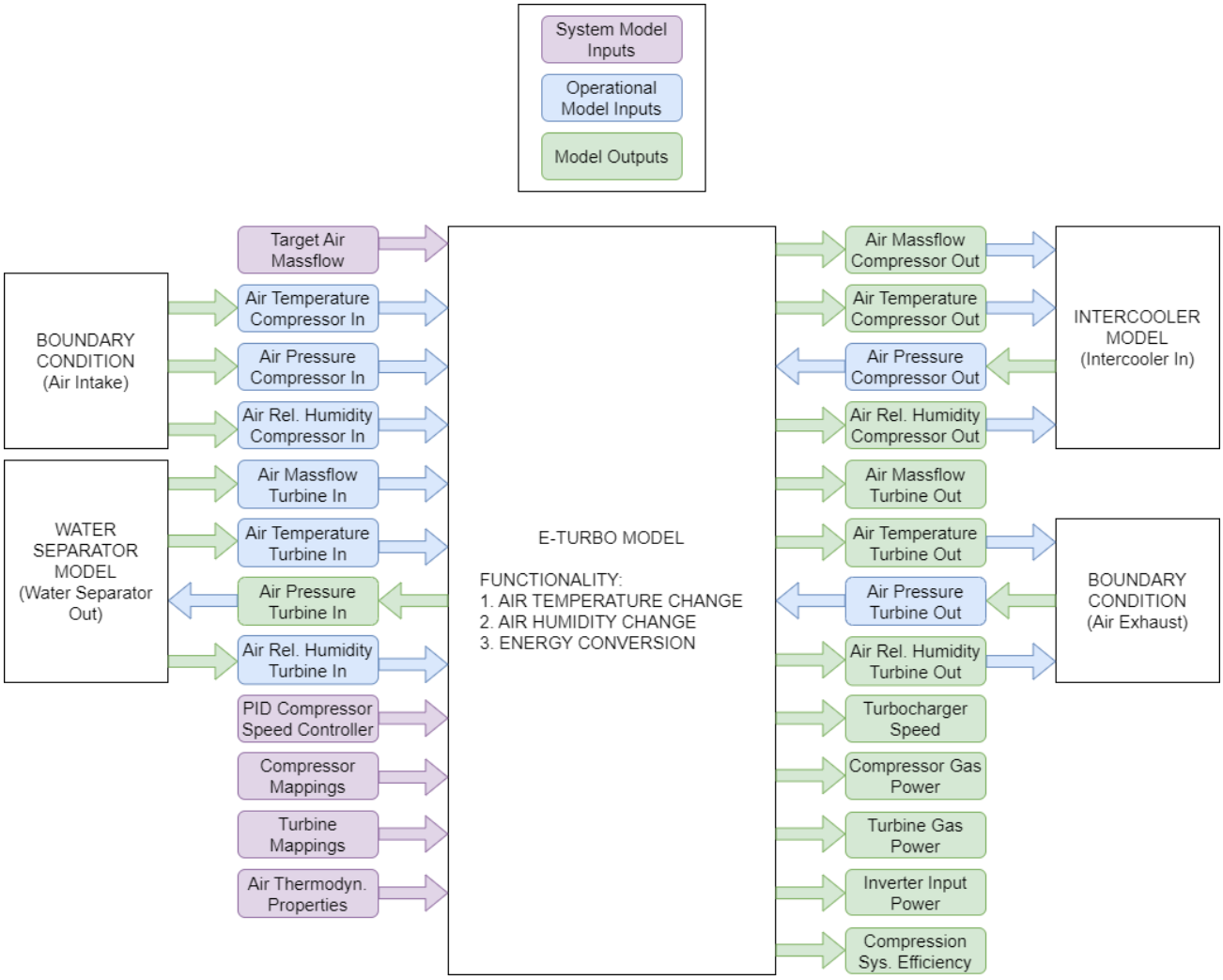

Figure A.2: Schematic of the Inputs and Outputs of the E-Turbocompressor Model

A.3 Baseline Model Reference Runs

The 50kW baseline reference air path results are visualized in figure A.3 below.

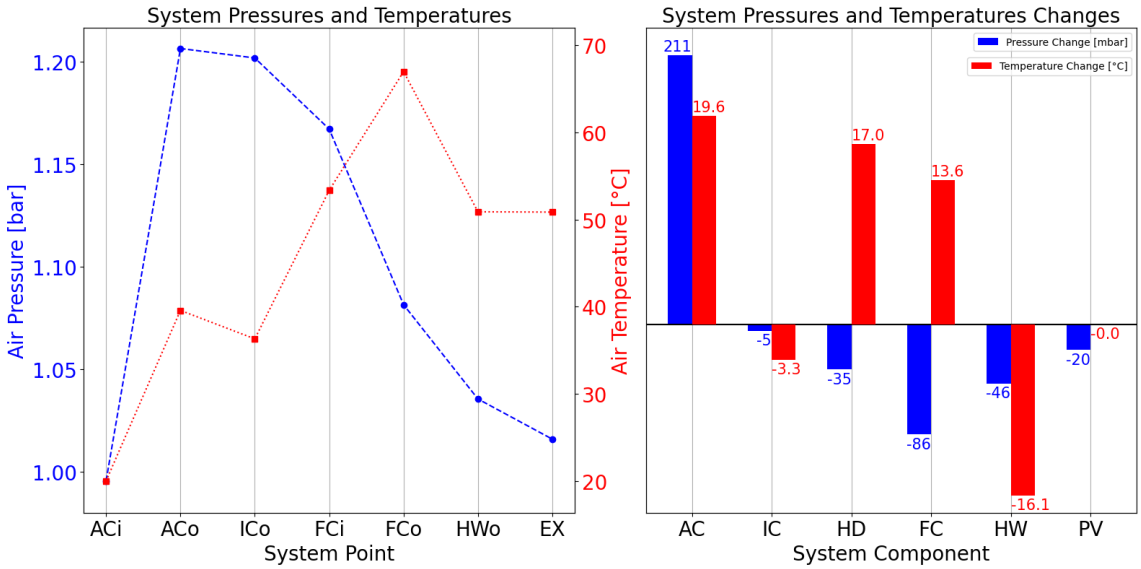

Figure A.3: Baseline Model Air Pressures and Temperatures for 50kW Stack Power at 20°C Ambient

The other two are shown in Figures A.4 and A.5. The only significant difference here is that due to the higher inlet temperature (20°C instead of around 11°C), the compressor outlet temperature is higher. This makes the intercooler outlet and humidfier dry outlet temperatures higher compared to the validation baseline runs.

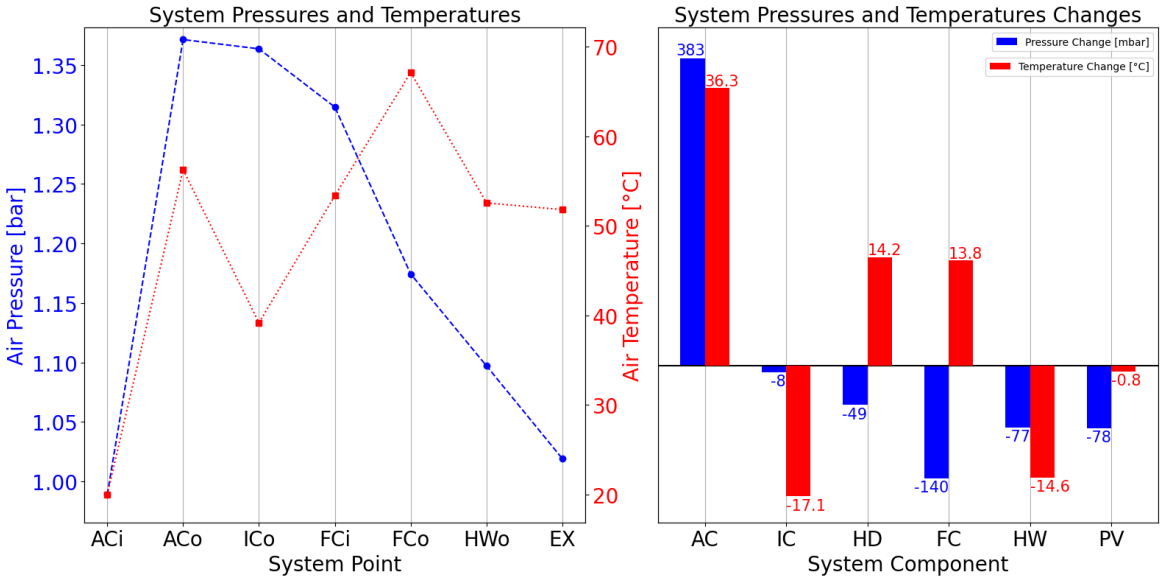

Figure A.4: Baseline Model Air Pressures and Temperatures for 70kW Stack Power at 20°C Ambient

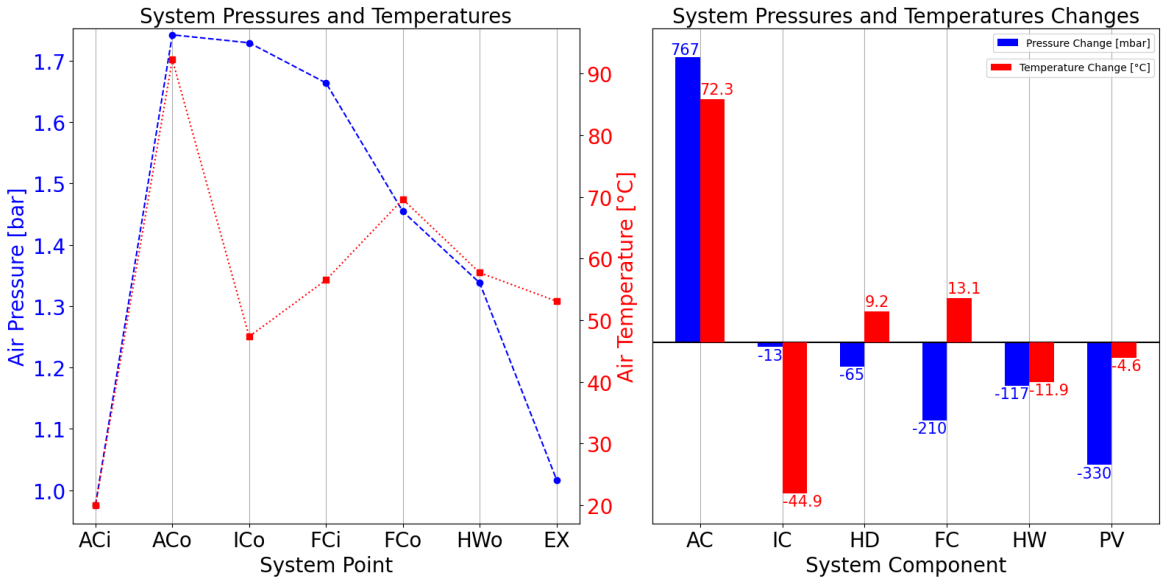

Figure A.5: Baseline Model Air Pressures and Temperatures for 97kW Stack Power at 20°C Ambient

The main system model outputs are shown in Table C.4 in Appendix C for all three reference runs. Looking at the system efficiency and hydrogen consumption, and comparing their values to the ones from Table C.3, they differ barely when changing the ambient temperature to 20°C. This makes sense, as for hydrogen fuel cell systems the ambient air temperature should not really have an effect on the fuel consumption.

The parameters that were most affected by the change in ambient temperature were of course the compressor air enthalpy change and the E-compressor inverter power. The change in value of these two parameters due to the change in ambient temperature is quantified in the table below:

Table A.1: Model Parameter Sensitivity w.r.t. a Change in Ambient Temperature

Level	ΔT_{amb}	$\Delta H_{a,c}$	P_{inv}
50 kW change	+8.77°C	3.17%	3.15%
70 kW change	+8.35°C	3.00%	2.97%
97 kW change	+7.86°C	2.73%	2.74%

As can be seen, the sensitivities fluctuate around 3% for a change in ambient temperature of roughly around 8°C. Again, there should not be a big influence of ambient temperature on compressor inverter input power, but here, the influence comes from the fact that the heat transfer within the E-compressor is affected by, amongst others, the ambient. That in turn affects the magnitude of $\Delta H_{a,c}$ (recall equation 3.61) which is used to predict P_{inv}, hence the small sensitivity with ambient temperature.

Appendix B

Details on Specific Calculations

B.1 Exhaust Heat Pump Analysis

One of the two selected concepts to go forward in the research was decided to be a turbocharged air processing system with an integrated heat pump to increase the air turbine inlet temperature (TIT) above the highest waste heat temperature occurring in the vehicle. After the literature study, it was not yet clear if the extra recovered exhaust energy by means of a higher TIT would outweigh the energy consumption of the heat pump compressor. For that reason, a simplified calculation was performed to check this, which is discussed briefly in this chapter.

The components considered in this analysis are as follows:

- heat pump evaporator transferring heat from the hot coolant to the working fluid
- heat pump compressor compressing and circulating the gaseous working fluid
- heat pump condenser transferring latent heat from the working fluid to the exhaust air
- E-turbocharger that recuperates exhaust energy, reducing electrical power consumption

The problem constants with their corresponding values are listed below, and if needed will be explained later on in this chapter:

- condenser air inlet temperature, $T_{a,i} = 55°\text{C}$
- exhaust air massflow, $\dot{m}_a = 286\text{kg/h}$
- air specific heat capacity, $c_{p,a} = 1005\text{J/kg/K}$
- hot source massflow, $\dot{m}_s = 2.6375\text{kg/s}$ (corresponds to volume flow of 150l/min)

- hot source specific heat capacity, $c_{p,s} = 3596 \text{J/kg/K}$ (water-glycol mixture)
- condenser heat exchange effectiveness, $\eta_{cond} = 1$
- evaporator heat exchange effectiveness, $\eta_{evap} = 1$
- heat pump compressor polytropic efficiency, $\eta_{poly} = 0.75$
- second law efficiency for heat pump coefficient of performance, $\eta_{2L} = 0.5$

Lastly, the input variables for this problem are:

- target condenser air outlet temperature/turbine inlet temperature, $T_{a,o} = TIT$
- evaporator hot source inlet temperature, $T_{s,i}$

The outputs of the calculation will be mentioned throughout the explanation of the method. A diagram of the considered problem is shown in Figure B.1.

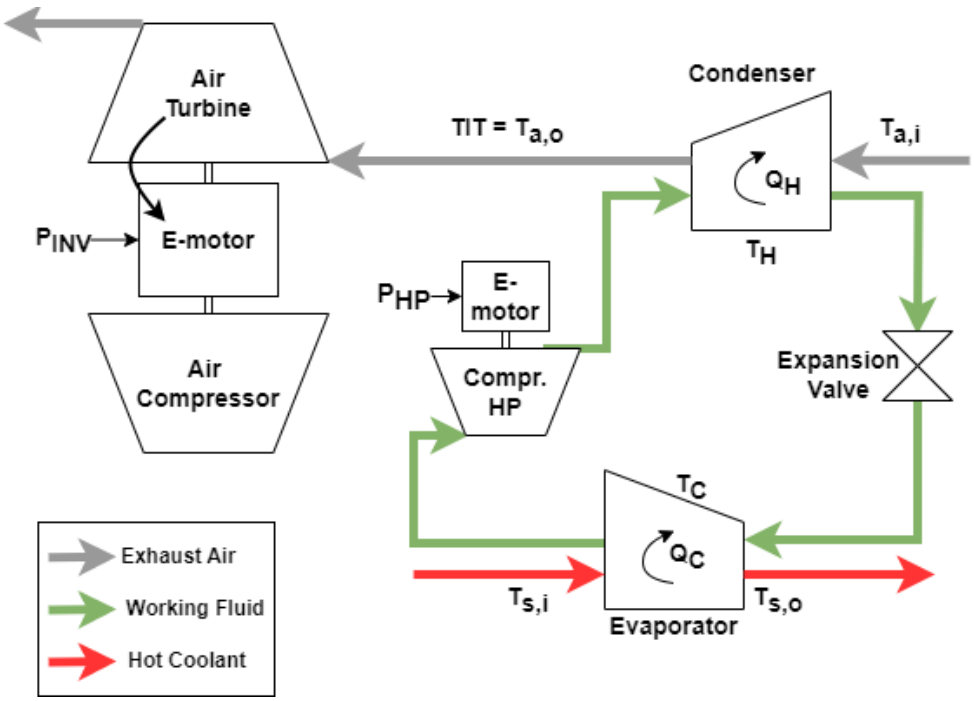

Figure B.1: Schematic of the Considered Heat Pump Integration Concept

The goal was, given a certain hot source temperature $T_{s,i}$ and a target TIT, to compute the necessary electrical power for the heat pump compressor (P_{HP} in the diagram) and the decrease in necessary electrical power for the air compressor (P_{inv} in the diagram). That way, it could be seen if the decrease in P_{inv} was larger than the value of P_{HP}, which means the setup would be beneficial. Let's now look at the calculations scheme.

The starting point was taken to be the necessary input heat to increase the air temperature from $T_{a,i}$ to $T_{a,o}$. This could be computed as follows:

$$\dot{Q}_a = \dot{m}_a \cdot c_{p,a} \cdot (T_{a,o} - T_{a,i}) = \dot{m}_a \cdot c_{p,a} \cdot (TIT - T_{a,i}) \tag{B.1}$$

This is thus the amount of heat that has to be transfered from the condensing working fluid to the air. The condenser could be assumed to be not 100% effective, so a condenser heat exchange effectiveness η_{cond} was introduced, meaning the latent heat that needed to be released by the working fluid was as follows:

$$\dot{Q}_H = \dot{Q}_a / \eta_{cond} \tag{B.2}$$

Next to this, in order for heat transfer to occur inside both the condenser and the evaporator, there had to be a temperature difference between the air and the working fluid (condenser side), as well as the hot coolant and the working fluid (evaporator side). It was assumed that the respective temperature differences would both be equal to 5 K compared to the condenser air outlet and evaporator coolant inlet, meaning the heat pump hot and cold temperatures could be computed by:

$$T_H = T_{a,o} + 5 \tag{B.3}$$

$$T_C = T_{s,i} - 5 \tag{B.4}$$

This way, there would always be heat transfer in the correct direction throughout the condenser and evaporator (from coolant to working fluid and working fluid to air, respectively). Knowing the heat pump hot and cold working temperatures, it was possible to calculate the theoretical Carnot coefficient of performance (COP):

$$COP_{Carnot} = \frac{T_H}{T_H - T_C} \tag{B.5}$$

The COP of real heat pumps is of course less because of losses due to the second law of thermodynamics. For (high temperature) heat pumps, a second-law efficiency showing the ratio between actual achieved COP and Carnot COP is commonly defined as:

$$\eta_{2L} = \frac{COP_{real}}{COP_{Carnot}} \tag{B.6}$$

From literature, it was seen that a good value for the second-law efficiency was 0.5 [36, p. 993], meaning COP_{real} could already be computed at this point. Additionally, the definition of the COP is simply the heat released at the condenser (useful energy) divided by the electrical input to the heat pump compressor (paid energy):

$$COP_{real} = \frac{\dot{Q}_H}{P_{HP}} \tag{B.7}$$

Therefore, the heat pump electrical power consumption depends on the heat pump working temperatures as follows:

$$P_{HP} = \frac{\dot{Q}_a / \eta_{cond}}{\eta_{2L} \frac{T_H}{T_H - T_C}} = \frac{\dot{Q}_a \cdot (T_H - T_C)}{\eta_{cond} \cdot \eta_{2L} \cdot T_H} \tag{B.8}$$

At this point, the only unknown at the heat pump was the hot coolant evaporator outlet temperature $T_{s,o}$. This could be calculated by defining both the heat transfer in the evaporator as well as the energy balance of the heat pump:

$$\dot{Q}_C = \dot{Q}_s \cdot \eta_{evap} = \eta_{evap} \cdot \dot{m}_s \cdot c_{p,s} \cdot (T_{s,i} - T_{s,o}) \tag{B.9}$$

and

$$\dot{Q}_C = \dot{Q}_H - \dot{W}_{HP} = \dot{Q}_H \cdot \left(1 - \frac{\eta_{poly}}{COP_{real}}\right) \tag{B.10}$$

since $\dot{W}_{HP} = P_{HP} \cdot \eta_{poly}$. The above two equations represent a system of two equations and two unknowns, namely $\dot{Q}_C$ and $T_{s,o}$. One can thus solve for $T_{s,o}$ as follows:

$$T_{s,o} = T_{s,i} - \left(1 - \frac{\eta_{poly}}{COP_{real}}\right) \cdot \left(\frac{1}{\eta_{cond}\eta_{evap}}\right) \cdot \left(\frac{\dot{m}_a \cdot c_{p,a}}{\dot{m}_s \cdot c_{p,s}}\right) \cdot (T_{a,o} - T_{a,i}) \tag{B.11}$$

Now, all parameters of the heat pump in order to generate $TIT = T_{a,o}$ are known and the only thing left to quantify was the change in inverter power consumption that powers the air compressor for the fuel cell system. This was done using data from an E-turbocharger on a testbench that was tested for $\dot{m}_a$ = 286kg/h with TITs varying from 50°C to 200°C. More information on the nature of this data is provided in Subsection 3.1.3. It was seen in this data that the decrease in inverter power consumption was linear with the increase in TIT. Therefore a simple linear trendline was generated in excel to provide a function that computes ΔP_{inv} as follows:

$$\Delta P_{inv} = P_{inv}(T_{a,i}) - P_{inv}(TIT) \tag{B.12}$$

Now, all the numbers were there to compute if the setup with integrated heat pump would be beneficial or not. If the difference between ΔP_{inv} and P_{HP} was positive, that means there would be an increased system net output power, and vice versa. The results of this initial investigations are presented below.

Three different scenarios were laid out: i) a hot source for the heat pump evaporator of $T_{s,i}$=70°C, ii) a hot source temperature $T_{s,i}$=110°C and iii) a hot source temperature $T_{s,i}$=150°C. For each of these cases, the benefit of the setup was computed in function of the desired air turbine inlet temperature $T_{a,o}$(=TIT) at the condenser side of the heat pump, which was varied from 5°C above to 50°C above the hot source temperature.

The higher the temperature lift ($T_H - T_C$), the higher the air turbine inlet temperature, but also the more heat pump compressor power would be needed.

To see if there was a net benefit, Figures B.2 - B.4 are shown.

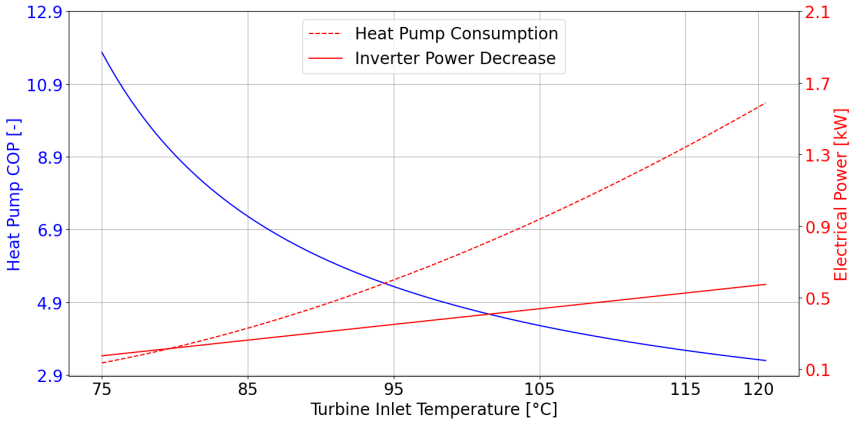

Figure B.2: Heat Pump Analysis for Hot Coolant Evaporator Inlet Temperature of 70°C

The blue solid line shows the change in heat pump COP in function of the turbine inlet temperature (TIT), and as expected, it follows a downwards trend. Specifically, $COP \sim 1/(T_H - T_C)$ as the theory predicts. The red dashed line represents the necessary heat pump compressor electrical power consumption, which grows superlinearly with the heat pump temperature lift. Finally, the solid red line shows the decrease in necessary air compressor inverter power ΔP_{inv} which scales linearly with the TIT (and thus with $(T_H - T_C)$).

Straightforwardly, when $\Delta P_{inv} - P_{HP} > 0$, there is a net benefit. From TIT = 75°C to about 80°C, this is indeed the case. However, the temperature where the difference $(\Delta P_{inv} - P_{HP})$ is maximum is at the first temperature of 75°C. What this means is that from the moment a heat pump is used, the performance of the setup becomes worse. Therefore, in this specific situation the use of a heat pump is not beneficial. For both other graphs in Figures B.3 and B.4, the same situation is observed. This means it can be concluded that this setup with a heat pump does not give extra benefit for any of the considered operational conditions.

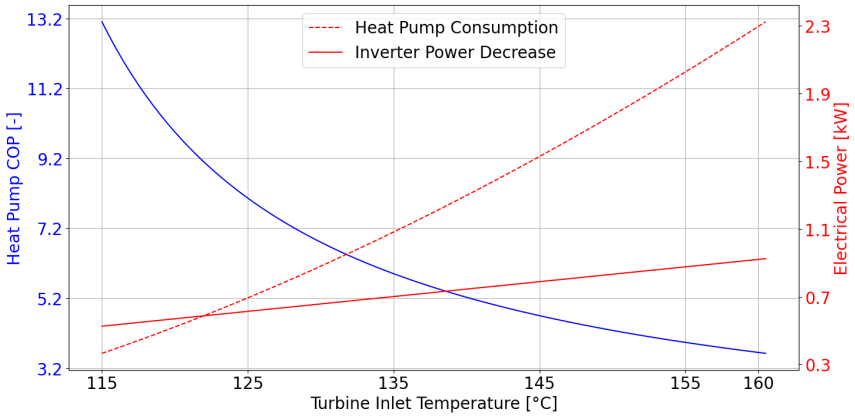

Figure B.3: Heat Pump Analysis for Hot Coolant Evaporator Inlet Temperature of 110°C

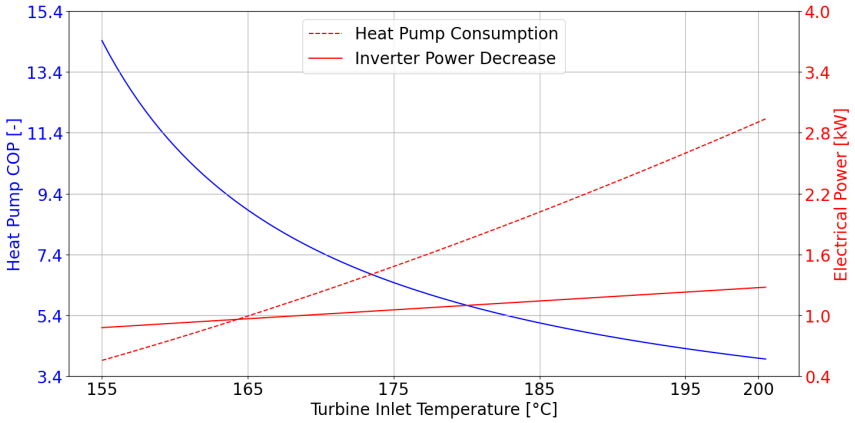

Figure B.4: Heat Pump Analysis for Hot Coolant Evaporator Inlet Temperature of 150°C

B.2 Calculation of Water Vapor Pressure at Stack Outlet

The following derivation is based on theory from [3] on pages 81 and 82. Assuming all the produced water in the stack is evaporated into the exhaust air, the ratio between the water partial pressure and air pressure at stack outlet is equal to:

$$\frac{p_{H_2O,fc,o}}{p_{a,fc,o}} = \frac{\dot{n}_{H_2O}}{\dot{n}_{H_2O} + \dot{n}_{O_2} + \dot{n}_{rest}} \tag{B.13}$$

where $\dot{n}$ is the molar massflow of either water (H_2O), oxygen (O_2) or other gasses ($rest$). The produced water, oxygen, and rest gasses that come out of the stack can be expressed as:

$$\dot{n}_{H_2O} = \frac{P_{fc}}{2 \cdot V_{cell} \cdot F} \tag{B.14}$$

$$\dot{n}_{O_2} = (\lambda_a - 1)\frac{P_{fc}}{4 \cdot V_{cell} \cdot F} \tag{B.15}$$

$$\dot{n}_{rest} = \frac{0.79}{0.21}\lambda_a \frac{P_{fc}}{4 \cdot V_{cell} \cdot F} \tag{B.16}$$

Substituting these three expressions in the first equation yields:

$$\frac{p_{H_2O,fc,o}}{p_{a,fc,o}} = \frac{1}{1 + (\lambda_a - 1)/2 + \frac{0.79}{0.21}\lambda_a/2} = \frac{2}{1 + 4.76\lambda_a} \tag{B.17}$$

such that one obtains:

$$p_{H_2O,fc,o} = \frac{0.42 \cdot p_{a,fc,o}}{0.21 + \lambda_a} \tag{B.18}$$

If the water brought into the fuel cell due to humidified intake air would also be considered, Equation 3.6 as mentioned before could be obtained. However, in the fuel cell stack model in this research, it was considered that not all produced water would leave the stack, which is a more realistic scenario. Remember the water flow factor κ, which indicated the fraction of the produced water that was assumed to leave with the exhaust air. In that case one should write:

$$\frac{p_{H_2O,fc,o}}{p_{a,fc,o}} = \frac{\dot{n}_{H_2O} \cdot \kappa}{\dot{n}_{H_2O} \cdot \kappa + \dot{n}_{O_2} + \dot{n}_{rest}} \tag{B.19}$$

which would become (when only considering produced water and no intake air water):

$$p_{H_2O,fc,o} = \frac{0.42 \cdot \kappa \cdot p_{a,fc,o}}{0.21 \cdot \kappa + 0.21 + \lambda_a} \tag{B.20}$$

Finally, when adapting the equation once more for also taking into account stack inlet air water, one obtains the final formula:

$$p_{H_2O,fc,o} = \frac{(0.42 \cdot \kappa + \psi \cdot \lambda_a) \cdot p_{a,fc,o}}{0.42 \cdot \kappa - 0.21 + (1 + \psi) \cdot \lambda_a} \tag{B.21}$$

B.3 Estimation of Intercooler Heat Transfer Coefficients

The following presented theory was taken from Chapter 3, 7 and 8 of [50]. By definition, UA can be expressed as:

$$UA = \left(\frac{1}{A_a \cdot h_a} + \frac{1}{A_c \cdot h_c} \right)^{-1} \tag{B.22}$$

Where A_a and A_c are the heat transfer surface areas for the air and coolant side respectively. They could be determined purely based on the geometrical features of the heat exchanger. The air heat transfer coefficient, h_a, could be predicted (i.e. modeled) for given operational (inlet) conditions of the air side, but h_c needed to be extracted from measurements.

In order to calculate the air and coolant side heat transfer surface areas, the correct geometrical formulae had to be used depending on the type of heat exchanger. This specific intercooler was a plate-fin heat exchanger with corrugated louvers. From [50, p. 517], a plate-fin geometry is shown in the figure below:

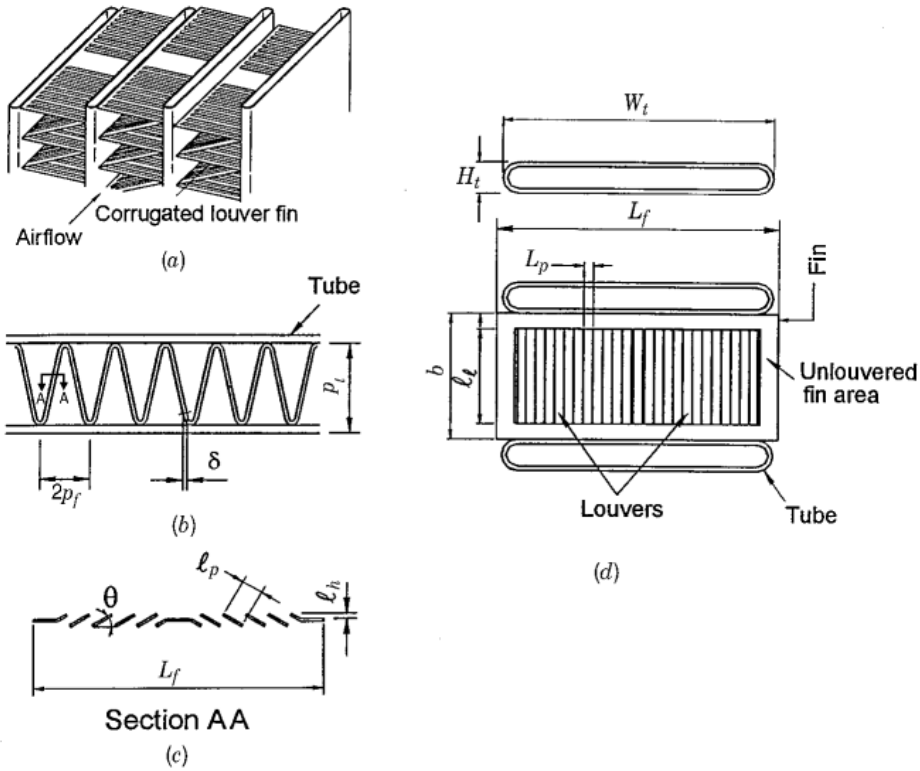

Figure B.5: Sketch of the Geometry of a Louvred Plate-fin Heat Exchanger. Isometric View Sketch (a), Fin Frontal View Sketch (b), Fin Cross-section Sketch (c) and Fin Side View Sketch (d)

The geometrical parameters shown in figure B.5 allowed to compute the air and coolant side surface areas as follows [50, p. 580]. For the air side:

$$A_{p,cell,a} = 2W_t(p_f - \delta) + 2p_f H_t \tag{B.23}$$

$$A_{f,cell,a} = 2L_f(b - \delta) \tag{B.24}$$

$$A_a = N_p \frac{W}{p_f}(A_{p,cell,a} + A_{f,cell,a}) \tag{B.25}$$

where N_p is the number of finned passages and W is the core width. For the coolant side:

$$A_{p,cell,c} = 2(W_t - 2t_t)(p_f - \delta) + 2p_f(H_t - 2t_t) \tag{B.26}$$

$$A_c = N_p \frac{W}{p_f} A_{p,cell,c} \tag{B.27}$$

The geometrical parameters were also necessary to compute h_a based on specified operational (inlet) conditions. First, some dimensionless numbers are introduced that were involved in this calculation. The Reynolds number (Re), the Prandtl number (Pr), the Stanton number (St) and the Colburn factor (j) are defined in equations B.28 - B.31 [50, p. 442]. Firstly, the Reynolds number:

$$Re = \frac{\rho \cdot V \cdot x}{\mu} = \frac{V \cdot x}{\nu} \tag{B.28}$$

where x is a characteristic length of the specific situation (e.g. relevant diameter or length), μ is the dynamic viscosity (units of Ns/m^2) and ν is the kinematic viscosity (units of m^2/s). The Reynolds number represents the ratio of inertial forces (momentum) and viscous forces (friction). Subsequently, the Prandtl number:

$$Pr = \frac{\mu \cdot C_p}{k} = \frac{\nu}{\alpha} \tag{B.29}$$

where k is the thermal conductivity (units of $W/(mK)$) and α is the thermal diffusivity (units of m^2/s). It represents the ratio of momentum diffusivity (kinemetic viscosity) and thermal diffusivity. Now onto the Stanton number:

$$St = \frac{h}{\rho \cdot V \cdot C_p} \tag{B.30}$$

which is the ratio of convective heat transfer and the fluid heat capacity rate. Finally, the Colburn factor:

$$j = St \cdot Pr^{2/3} \tag{B.31}$$

which is an adapted Stanton number to take into account the change in Prandtl number for turbulent flows. This Colburn factor can be empirically predicted based on the flow conditions represented by the Reynolds number and the geometrical features of the intercooler [50, p. 517]:

$$j = Re_{l_p}^{-0.49} \left(\frac{\theta}{90}\right)^{0.27} \left(\frac{p_f}{l_p}\right)^{-0.14} \left(\frac{b}{l_p}\right)^{-0.29} \left(\frac{W_t}{l_p}\right)^{-0.23} \left(\frac{l_l}{l_p}\right)^{0.68} \left(\frac{p_t}{l_p}\right)^{-0.28} \left(\frac{\delta}{l_p}\right)^{-0.05} \tag{B.32}$$

Hence, for given inlet conditions, the Reynolds number was first computed and the Colburn factor was found.

If one combines equation B.30 and B.31 and eliminates St and solves for h, one obtains the following expression:

$$h = \rho \cdot V \cdot C_p \cdot j \cdot Pr^{-2/3} = \frac{\dot{m}}{A_0} \cdot C_p \cdot j \cdot Pr^{-2/3} \tag{B.33}$$

Since for the air inlet, A_0 (the free-flow area defined in equation B.44), C_p and j are known now, if one knows also the value of Pr, then a value for h can be found as previously stated. For air, the Prandtl numher varies slightly depending on pressure and temperature but is

rather constant. The following table shows the air Prandtl number for various temperatures at two different pressure levels[1]:

Table B.1: Air Prandtl Number Values for Various Temperature and Pressure Levels

	1 bara pressure	**5 bara pressure**
temperature °C	**Prandtl number [-]**	**Prandtl number [-]**
0	0.711	0.715
6.9	0.71	0.714
15.6	0.709	0.713
26.9	0.707	0.711
46.9	0.705	0.708
66.9	0.703	0.705
86.9	0.701	0.703
106.9	0.7	0.702
126.9	0.699	0.701
226.9	0.698	0.7
326.9	0.703	0.704

Indeed, the Prandtl number variation is very small in the range that was relevant for the system simulations, meaning the average value of all Prandtl numbers in this table was used in the model. This average is equal to $Pr = 0.70555$. Now finally, h_a could be computed.

With h_a known, only the value of h_c was missing to find UA. That value could be estimated based on measurement data of the real intercooler. An overview of the needed measurement parameters in order to perform the calculations is provided below:

- air massflow through the intercooler
- air inlet and outlet temperatures
- air inlet and outlet pressures
- coolant massflow through the intercooler
- coolant inlet and outlet temperatures

With this information, the following procedure was followed to obtain an estimation for h_c. First, the transferred heat needed to be quantified. In steady-state and according to conservation of energy, the heat given off by the air is the same as the heat taken up by the coolant. But in practice, there are other modes of heat transfer (through the materials, casings and piping, natural convection and radiation) meaning that in experiments, the two quantities could be different. Since the focus of this model was regarding the temperature change on the air side, the enthalpy change of the air was taken as the start:

$$Q_a = \dot{m}_a \cdot C_{p,a} \cdot \Delta T_a \tag{B.34}$$

[1] https://www.engineeringtoolbox.com/air-prandtl-number-viscosity-heat-capacity-thermal-conductivity-d_2009.html

This was by assumption equal to the heat exchanged in the intercooler: $Q_a = Q_{HX}$. The heat exchange in the intercooler can be expressed as follows:

$$Q_{HX} = U \cdot A \cdot \Delta T_m \tag{B.35}$$

with ΔT_m being the average temperature difference between the air and coolant side of the intercooler along the channels. If this temperature difference is known, UA can be computed. However, this temperature difference is in practice unknown and hard to quantify. Therefore, another approach was taken to estimate this temperature difference. To elaborate on this, the concept of the Log-Mean Temperature Difference ($LMTD$) should be noted first. The $LMTD$ is the theoretical temperature difference between the hot and cold streams averaged along the heat transfer surface (e.g. length) of a heat exchanger. For an ideal counterflow heat exchanger with infinite surface area, $\Delta T_m = LMTD$. In this case, the counterflow $LMTD$ would be expressed as:

$$LMTD = \frac{(T_{a,o} - T_{c,i}) - (T_{a,i} - T_{c,o})}{\ln(T_{a,o} - T_{c,i}) - \ln(T_{a,i} - T_{c,o})} \tag{B.36}$$

However, the intercooler considered in this research is of the cross-flow configuration, meaning that the $LMTD$ from equation B.36 is not the same as our desired ΔT_m. But there exists a correction factor F that can be multiplied with the $LMTD$ to estimate ΔT_m. From [54, p. 37], the following empirical relation was taken:

$$F = (1 + aR_1^{db} NTU_1^b)^{-c} \tag{B.37}$$

$$R_a = \frac{C_a}{C_c} \tag{B.38}$$

$$NTU_a = \frac{UA}{C_a} \tag{B.39}$$

where R_1 and NTU_1 are the air-to-coolant heat rate capacity ratio and the air-side NTU respectively (which is the same as the overall NTU since for this intercooler, $C_a = C_{min}$). For this specific intercooler, [54, p. 37] provides the following coefficient values: $a = 0.433$, $b = 1.6$, $c = 0.267$ and $d = 0.5$. This allowed to compute the correction factor based on the operational conditions. Knowing F, an estimate for UA could be made as follows:

$$UA = \frac{Q_a}{LMTD \cdot F} \tag{B.40}$$

Now that UA was obtained, it was possible to use equation B.22 to solve for h_c since h_a could be calculated using the measurement data as per equation B.33.

With the computed values for h_c as input to the intercooler heat exchange model, finally, together with the already computed h_a, the value for UA can be found as per equation B.22. This value is accurate as long as the coolant masflow in the simulation is the same as in the test that generated the measurement data, denoted as the nominal massflow. If it is desired

to run a simulation with a different coolant massflow, a simple correction to h_c can be applied in the form of:

$$h_{c,new} = h_{c,nom} \left(\frac{\dot{m}_{c,new}}{\dot{m}_{c,nom}} \right)^{0.8} \tag{B.41}$$

For the current research, it was sufficient to use the nominal flow since the intercooler air outlet temperature was always below the upper safety limit (protecting the humidifier and fuel cell stack membranes).

B.4 Computing the Intercooler Air Pressure Drop

The following presented theory was based on Chapter 6 and 7 from [50]. For heat exchangers with corrugated louvre fins, the air-side pressure drop is given by the following equation [50, p. 388]:

$$\frac{\Delta p}{p_i} = \frac{\dot{m}^2}{2A_0^2 \rho_i p_i} \cdot \left[1 - \sigma^2 + K_c + 2\left(\frac{\rho_i}{\rho_o} - 1 \right) + \frac{f L_f}{r_h} \rho_i v_m - (1 - \sigma^2 - K_e) \frac{\rho_i}{\rho_o} \right] \tag{B.42}$$

where A_0 is the free-flow cross-sectional area of the intercooler air inlet, σ the ratio of free flow to frontal cross-sectional area, K_c the entrance loss factor, f the friction factor, L_f the fin length, $r_h = D_h/4$ the hydraulic radius, $v_m = 0.5(1/\rho_i + 1/\rho_o)$ the mean specific volume and K_e the exit loss factor. The entrance and exit pressure loss make up less than 10% of the total air pressure drop, and hence the above equation was simplified to:

$$\frac{\Delta p}{p_i} = \frac{\dot{m}^2}{2A_0^2 \rho_i p_i} \cdot \left[2\left(\frac{\rho_i}{\rho_o} - 1 \right) + \frac{f L_f}{r_h} \rho_i \frac{1}{2} \left(\frac{1}{\rho_i} + \frac{1}{\rho_o} \right) \right] \tag{B.43}$$

At this point, there were two unknowns in this equation, namely Δp and ρ_o. The values for A_0, f and r_h could be calculated based on the intercooler geometry and the inlet Reynolds number. The free-flow cross-section and the hydraulic radius are computed as follows:

$$A_0 = N_p \frac{W}{p_f} A_{0,cell} = N_p \frac{W}{p_f} \left(p_f b - \delta(b - \delta) \right) \tag{B.44}$$

$$r_h = \frac{D_h}{4} = \frac{A_{0,cell} L_f}{A_{p,cell,a} + A_{f,cell,a}} \tag{B.45}$$

The friction factor could be estimated using an empirical relation from [50, p. 518] that combines the air inlet Reynolds number and intercooler geometry. Since the Reynolds numbers for this intercooler were always between 150 and 300 (checked with the measurement data), the following relations for the friction factor were valid:

$$f_1 = 4.97 Re_{lp}^{(0.6049 - 1.064/\theta^{0.2})} \left[\ln \left(\sqrt{\delta/p_f} + 0.9 \right) \right]^{-0.527} \tag{B.46}$$

$$f_2 = \left[(D_h/l_p) \ln (0.3 Re_{lp}) \right]^{-2.966} \left(p_f/l_l \right)^{(-0.7931 p_t/b)} \tag{B.47}$$

$$f_3 = (p_t/H_t)^{-0.0446} \left[\ln\left(1.2 + (l_p/p_f)^{1.4}\right)\right]^{-3.553} \theta^{-0.477} \tag{B.48}$$

$$f = f_1 f_2 f_3 \tag{B.49}$$

The problem of having just one equation (equation B.43) and two unknowns (Δp and ρ_o) was solved by invoking the equation of state. The outlet air density could be substituted for an expression of the outlet air pressure. The equation of state applied to the intercooler air outlet namely gives:

$$\rho_o = \frac{p_o}{RT_o} \tag{B.50}$$

where $R = 287.05$ J/kg/K is the air specific gas constant. Since the air outlet temperature T_o was already computed in the thermal model of the intercooler, the substitution of equation B.51 into equation B.43 could yield a single equation with one unknown, namely the outlet pressure:

$$p_o^2 - \left[p_i + \frac{\dot{m}^2}{A_0^2 \rho_i}\left(1 - \frac{fL_f}{4r_h}\right)\right] \cdot p_o + \frac{\dot{m}^2 RT_o}{A_0^2}\left(1 + \frac{fL_f}{4r_h}\right) = 0 \tag{B.51}$$

This is cleary a second order polynomial equation, which can be analytically solved for p_o. When this equation is solved, two potential outlet pressures are always obtained. However, only one pressure could be the correct one. It seemed that there was always a pressure close to vacuum, and another pressure that was slightly lower than the inlet air pressure. The latter is obviously the correct value, so this one was chosen. By now knowing both the inlet and outlet air pressure of the intercooler, the pressure drop was straightforwardly calculated.

One thing to note here: the intercooler pressure drop in this model depends on the inlet pressure. As discussed before in Section 3.3.3, the chain of pressure calculations works from downstream to upstream direction. For the intercooler specifically, the simulation therefore performs an iteration loop that started off with an initial condition (ambient temperatures and pressures everywhere in the system). Based on an initial intercooler inlet pressure, the intercooler outlet pressure is computed from which the pressure drop follows. Then, by knowing the outlet pressure from the next component, the new intercooler inlet pressure can be updated using the found pressure drop. Finally, using the new intercooler inlet pressure, the new outlet pressure can be computed, and the loop repeats.

B.5 Stagnation vs. Static Conditions - Calculating the Difference

The equations stated below were taken from Chapter 4 of [49]. The stagnation temperature is the hypothetical temperature a gas would have if it were slowed down from its velocity to

a stop without any work or heat transfer. For a perfect gas, this means:

$$T_t = T + \frac{V^2}{2 \cdot C_p} \tag{B.52}$$

which can be rewritten to:

$$\frac{T_t}{T} = 1 + \frac{\gamma - 1}{2} M^2 \tag{B.53}$$

The stagnation pressure is defined as the hypthetical pressure a gas would have without any heat transfer or losses, implying an isentropic process. Therefore it can be expressed as:

$$\frac{p_t}{p} = \left(\frac{T_t}{T}\right)^{\gamma/(\gamma-1)} = \left(1 + \frac{\gamma - 1}{2} M^2\right)^{\gamma/(\gamma-1)} \tag{B.54}$$

Finally, for the density one obtains:

$$\frac{\rho_t}{\rho} = \left(1 + \frac{\gamma - 1}{2} M^2\right)^{\frac{1}{\gamma-1}} \tag{B.55}$$

When the flow speed is sufficiently low, it is common practice to interchange stagnation conditions with static conditions, meaning it is assumed that $T_t = T$, $p_t = p$ and $\rho_t = \rho$. To check whether this is the case or not, the threshold Mach number needs to be defined. This is defined as the Mach number where the total and static conditions vary less than 5%.

The most well-known example of this in aerospace engineering is the assumption that air is incompressible below Mach numbers of around 0.3. To show this, equation B.55 is used by filling in $\frac{\rho_t}{\rho} = 1/0.95$ (since the total quantity is always higher than the static quantity) and solving for the Mach number. Indeed, one obtains $M = 0.322$. The same threshold Mach numbers can be found for the same 5% variation condition for the temperature and pressure using equations B.53 and B.54. The corresponding Mach numbers are then 0.512 and 0.271, respectively. The limiting value in this research is thus the pressure threshold Mach number of 0.271.

For the compressor outlet, the highest Mach number seen in the data was 0.212, meaning at the compressor outlet side the total conditions could be assumed equal to the total conditions. On the compressor inlet, the maximum Mach number was 0.288 which is above the 5% threshold. However, computing $\frac{p}{p_t}$ with this Mach number using equation B.54 yields a variation of 5.6%. For this research, this was still deemed sufficient to assume that also on the compressor inlet side, total conditions equalled static conditions.

B.6 Proving $p_{2,ab} \approx p_2$ For E-Compressor Outlet Temperature Computation in this Research

Can it be said that the measured outlet pressure p_2 is the same as the would-be adiabatic outlet pressure $p_{2,ab}$? Those pressures being equal was implied, but the validity of this had to be checked. This is done now.

A flow that is subject to only heat transfer (no work transfer) and has no losses (e.g. friction), is called a Rayleigh flow[2]. The simplest type of Rayleigh flow is a one-dimensional flow going through a constant area duct that is subjected to a certain heat transfer. Say the flow enters the duct at temperature $T_{2,ab}$, pressure $p_{2,ab}$ and Mach number $M_{2,ab}$ and leaves the duct at T_2, p_2 and M_2. The Mach number is simply the ratio between the actual flow speed and the speed of sound for those flow conditions. From Rayleigh flow theory, the change in pressure could then be quantified by the following formula:

$$\frac{p_2}{p_{2,ab}} = \left(\frac{1+\gamma M_{2,ab}^2}{1+\gamma M_2^2}\right)\left(\frac{1+\frac{\gamma-1}{2}M_2^2}{1+\frac{\gamma-1}{2}M_{2,ab}^2}\right)^{\frac{\gamma}{\gamma-1}} \tag{B.56}$$

From the measurement data, it was known that the highest value of M_2 was 0.212. Assuming the threshold Mach number value for the duct inlet, $M_{2,ab} = 0.271$, the variation in the pressures is 1.7% only ($\frac{p_2}{p_{2,ab}} = 1.017$). In the extreme case of $M_2 = 0$, the variation is still just 4.8% which is below the threshold of 5%.

The last thing that had to be checked was if $M_{2,ab}$ could be higher than 0.271, as then the '<5% rule' might not be achieved. For this, one could look at the temperatures, which according to Rayleigh theory are related through:

$$\frac{T_2}{T_{2,ab}} = \left(\frac{M_2[1+\gamma M_{2,ab}^2]}{M_{2,ab}[1+\gamma M_2^2]}\right)^2\left(\frac{1+\frac{\gamma-1}{2}M_2^2}{1+\frac{\gamma-1}{2}M_{2,ab}^2}\right) \tag{B.57}$$

If one fills in $M_{2,ab} = 0.271$ and $M_2 = 0.212$ in this equation, the temperature ratio would be: $\frac{T_2}{T_{2,ab}} = 0.655$. From the data, the temperature corresponding to $M_2 = 0.212$ was $T_2 = 103.8$ °C or 376.8 K. With the found temperature ratio, that would mean $T_{2,ab} = 575.2$ K or 302.2 °C which is clearly not realistic. In the data, $T_1 = 20$ °C, and since the adiabatic compression ratio follows from (cite):

$$\Pi_c = \left(\frac{T_{2,ab}}{T_1}\right)^{\frac{\gamma}{\gamma-1}} \tag{B.58}$$

it would mean that if $M_{2,ab} = 0.271$, the compression ratio would be around 10.6 which is unrealistically high for this type of radial compressor. The conclusion therefore was that $M_{2,ab} < 0.271$, and it could be concluded that $p_{2,ab} = p_2$.

B.7 The First Attempt to Calculate the E-Compressor Outlet Temperature

To try and solve the problem, it was assumed that the non-adiabatic compression happened in two stages. First, the air compresses adiabatically, a process represented by the orange arrow in Figure 3.11. Secondly, the air cools down without work transfer, the process represented by

[2] https://kyleniemeyer.github.io/gas-dynamics-notes/compressible-flows/heat-transfer.html

the red arrow. Following these two stages, one ends up at the real measured outlet conditions, and the combined effective process is the one represented by the green arrow.

The assumption that the compression and heat transfer happen sequentially as described above, allowed to calculate the temperature in the opposite direction: starting from the measured and therefore known T_2, the unknown and desired $T_{2,ab}$ could be estimated through some specified method. This way, a more representative efficiency estimate could be obtained by applying:

$$\eta_c = \frac{T_{2s} - T_1}{T_{2,ab} - T_1} = \frac{T_1 \left[\left(\frac{p_2}{p_1} \right)^{(\gamma-1)/\gamma} - 1 \right]}{T_{2,ab} - T_1} \tag{B.59}$$

The available measurement data to perform the calculations are tabulated below:

Table B.2: Overview of Measured E-compressor Parameters

Parameter	Symbol
Inverter Input Power	P_{inv}
Inverter Efficiency	η_{inv}
Air Compressor Intlet & Outlet Temperature	T_1 & T_2
Air Compressor Inlet & Outlet Pressure	p_1 & p_2
Compressor Air Massflow	$\dot{m}_a$
Coolant Inlet & Outlet Temperature	$T_{c,i}$ & $T_{c,o}$
Coolant Massflow	$\dot{m}_c$

A start was made by invoking conservation of energy. An overview of the energy flows in a liquid-cooled E-compressor is shown in Figure B.6.

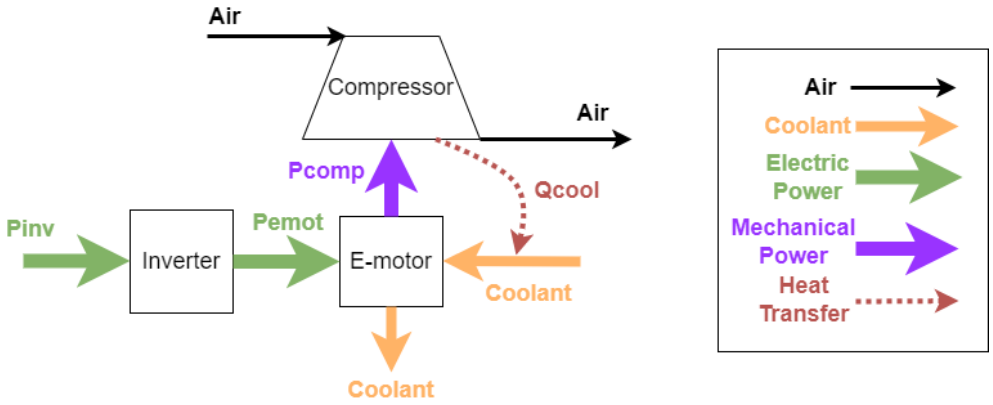

Figure B.6: Schematic Showing the Energy Flows in an E-Compressor

From the perspective of the air going through the compressor, the following energy balance could be made:

$$\dot{W}_a - \dot{Q}_a = \Delta H_a \tag{B.60}$$

where ΔH_a represents the air enthalpy change, $\dot{W}_a$ is the effective work the compressor performs on the air and $\dot{Q}_a$ is the heat extracted from the air by the liquid coolant. It is assumed this is the only mode of heat transfer, and no heat is going to other places. In reality, that is obviously not the case, but due to lack of more information, other modes of heat transfer could not be quantified, hence the decision to make this assumption. The above energy balance was rewritten in more detail to involve the problem parameters stated in Table B.2:

$$[P_{inv} \cdot \eta_{inv} \cdot \eta_{emot} \cdot \eta_c] - [\dot{m}_a \cdot c_{p,a} \cdot (T_{2,ab} - T_2)] = [\dot{m}_a \cdot c_{p,a} \cdot (T_2 - T_1)] \tag{B.61}$$

where η_{emot} is the E-motor efficiency (electrical+mechanical). This could be simplified to:

$$P_{inv} \cdot \eta_{inv} \cdot \eta_{emot} \cdot \eta_c = \dot{m}_a \cdot c_{p,a} \cdot (T_{2,ab} - T_1) \tag{B.62}$$

Looking at the cooling liquid, its heat balance was set up as follows:

$$\dot{m}_c \cdot c_{p,c} \cdot (T_{c,o} - T_{c,i}) = P_{inv} \cdot \eta_{inv} \cdot (1 - \eta_{emot}) + \dot{m}_a \cdot c_{p,a} \cdot (T_{2,ab} - T_2) \tag{B.63}$$

The first term on the right hand side of the above equation represents the heat generated by the compressor E-motor (as $P_{emot} = P_{inv} \cdot \eta_{inv}$), and the second term is the heat extracted from the compressing air.

At this point, there are three unknowns, namely η_{emot}, $T_{2,ab}$ and η_c, but also three equations, namely Equations B.59, B.62 and B.63. This means the problem could be mathematically solved, and it turned out the solution was also analytic. The obtained expression for $T_{2,ab}$ in terms of purely known quantities was:

$$\alpha \cdot (T_{2,ab} - T_1)^2 + \beta \cdot (T_{2,ab} - T_1) + \delta = 0 \tag{B.64}$$

where the coefficients α, β and δ were found to be:

$$\alpha = \frac{\dot{m}_a \cdot c_{p,a}}{T_1 \left(\Pi_c^{\frac{\gamma-1}{\gamma}} - 1 \right)} \tag{B.65}$$

$$\beta = -\dot{m}_a \cdot c_{p,a} \tag{B.66}$$

$$\delta = \dot{m}_a \cdot c_{p,a} \cdot (T_2 - T_1) + \dot{m}_c \cdot c_{p,c} \cdot (T_{c,o} - T_{c,i}) - P_{inv} \cdot \eta_{inv} \tag{B.67}$$

One could now solve for $T_{2,ab}$ making sure to use temperature values in Kelvin, which gave two options (two roots): a negative and a positive temperature in Kelvin. A negative Kelvin temperature is obviously impossible, so the positive root had to be chosen.

Unfortunately, the obtained $T_{2,ab}$ was actually always lower than T_2 instead of higher, meaning the corrected efficiencies (using Equation B.59) were even higher, instead of lower. The reason for this behavior was attributed to the fact that the heat balance formulated in Equation B.63 is not correct, rather, it is too simple. As mentioned, the heat from the compressing air does not only go into the E-motor cooling, but conducts through the compressor casing, convects and radiates away to the environment, etc. These heat flows were impossible to quantify with the available data, and therefore, the method did not succeed.